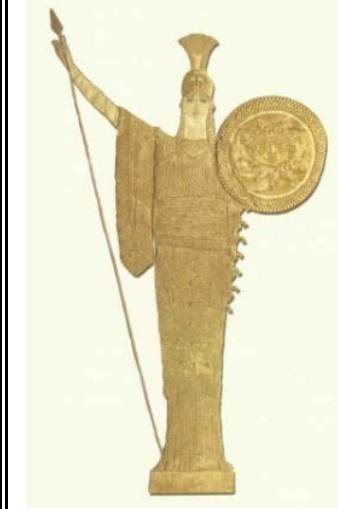


Εθνικόν και Καποδιστριακόν
Πανεπιστήμιον Αθηνών
Σχολή Θετικών Επιστήμων
Τμήμα Γεωλογίας και
Γεωπεριβάλλοντος
Τομέας Ορυκτολογίας
και Πετρολογίας
Πανεπιστημιούπολη
Ζωγράφου, Αθήνα
15784



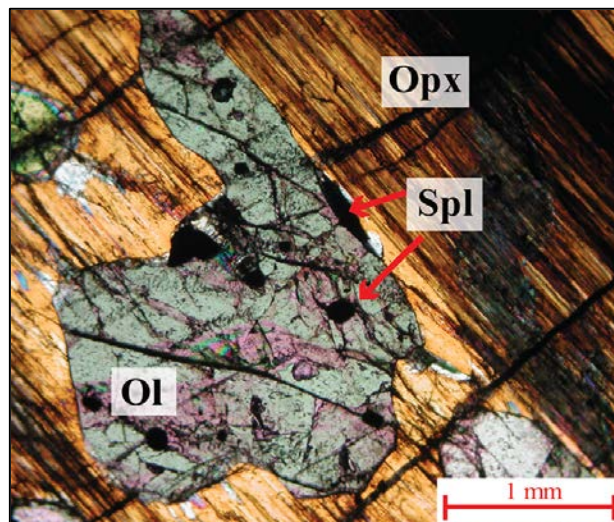
National and Kapodistrian
University of Athens
School of Sciences
Faculty of Geology and
Geoenvironment
Department of Mineralogy
and Petrology
Panepistimioupoli
Zographou, Athens 15784
Greece

BSc Diploma Thesis – Προπτυχιακή Διπλωματική Εργασία

A novel calibration of the Fe^{+2} -Mg exchange thermometer between orthopyroxene and spinel with application to mantle peridotites

Μία νέα βαθμονόμηση του θερμομέτρου ανταλλαγής Fe^{2+} -Mg μεταξύ ορθοπυροξένου και σπινελίου με εφαρμογή σε μανδουακούς περιδοτίτες

**Βασίλειος Γιατρός (A.M. 1114201700015)
Vasileios Giatros (Reg.No. 1114201700015)**



**Αθήνα, 2021
Athens, 2021**

Επιβλέπων: Επ. Καθ. Δημήτριος Κωστόπουλος
Thesis Supervisor: Ass. Prof. Dr. Dimitrios Kostopoulos

ACKNOWLEDGEMENTS

This thesis was initiated in the summer of 2019 and finalized in the summer of 2021, during my B.Sc. studies in the Faculty of Geology and Geoenvironment of the National and Kapodistrian University of Athens, Greece. Throughout this whole endeavor, I had the support of certain individuals who helped me achieve my goal of presenting this project. For this reason, I would like to thank:

My supervisor, Professor of Metamorphic Petrology Dr. Dimitrios Kostopoulos, for his guidance which helped me develop my scientific thinking and encouraged me to continuously seek novel ways to approach Geology, but mainly because I have become a better person and a scientist through our collaboration and many fruitful discussions.

Professor Dr. Panagiotis Pomonis, as well as my colleagues Dimitris Moutzouris, Nefeli Tsirikou–Kasimati and Antonis Laskos, for their continuous support and advice, that made the process of understanding Geology easier for me.

My mother Despoina Christodoulou and my family, Vasilis Christodoulou, Chrysoula Christodoulou, Paulina Christodoulou and Kostas Koulouris for raising me and making me stand on my feet.

All those close to me: Stelios Maragakis, Nikos Moutas, Marios–Angelos Kalemis and Fani Kalogirou for standing by my side through thick and thin and always being there for me,

and last but not least, Ms. Elisavet Vorgia and the coaching school «Αλληλεγγύη» of the Municipal Community Service of Piraeus, for their help in my first steps as a scientist. They were there for me at the very beginning of my scientific career, by supporting and helping me transform my dreams into reality. Without Ms. Elisavet, I wouldn't have made it this far.

ΕΥΧΑΡΙΣΤΙΕΣ

Η παρούσα διπλωματική εργασία ξεκίνησε το καλοκαίρι του 2019 και περατώθηκε το καλοκαίρι του 2021, στα πλαίσια του προπτυχιακού προγράμματος σπουδών του τμήματος Γεωλογίας και Γεωπεριβάλλοντος του Εθνικού και Καποδιστριακού Πανεπιστημίου Αθηνών. Πριν και κατά το χρονικό διάστημα της εκπόνησης της διπλωματικής εργασίας, υπήρξαν συγκεκριμένοι άνθρωποι που με βοήθησαν να μπορέσω να παρουσιάσω τον παρόν έργο. Γι' αυτό θα ήθελα να ευχαριστήσω τους κάτωθι:

Τον επιβλέποντα καθηγητή μου, Δρ. Δημήτριο Κωστόπουλο, για την βοήθεια του ώστε να αναπτύξω την επιστημονική μου σκέψη, να βλέπω συνεχώς την γεωλογία με νέα μάτια, αλλά κυρίως επειδή με βοήθησε να γίνω ένας καλύτερος άνθρωπος και επιστήμονας μέσω της συνεργασίας μας και των πολλών γόνιμων συζητήσεών μας.

Τον καθηγητή Δρ. Παναγιώτη Πομόνη καθώς και τους συναδέλφους μου Δημήτρη Μουτζούρη, Νεφέλη Τσιρικού–Κασιμάτη και τον Αντώνη Λάσκο για την συνεχή τους βοήθεια και τις συμβουλές τους, κάνοντας την κατανόηση της γεωλογίας πιο εύκολη.

Την μητέρα μου Δέσποινα Χριστοδούλου καθώς και την οικογένεια μου, Βασίλη Χριστοδούλου, Χρυσούλα Χριστοδούλου, Παυλίνα Χριστοδούλου και Κώστα Κουλούρη για τον τρόπο που με μεγάλωσαν, κάνοντάς με έναν άνθρωπο ικανό να στέκομαι στα πόδια μου.

Τους κοντινούς μου ανθρώπους Στέλιο Μαραγκάκη, Νίκο Μούτα, Μάριο Άγγελο Καλέμη και Φανή Καλογήρου που μου στάθηκαν σε όλες τις δυσκολίες και όποτε τους χρειαζόμουν ήταν πάντα εκεί.

Την κ. Ελισάβετ Βοργιά και την Κοινωφελή Δημοτική Επιχείρηση Πειραιά για την βοήθεια τους στα πρώτα μου επιστημονικά βήματα. Ήταν εκεί στην αρχή της επιστημονικής μου σταδιοδρομίας, υποστηρίζοντας και βοηθώντας με να χτίσω τα όνειρά μου. Χωρίς την κ. Ελισάβετ δεν θα ήμουν σήμερα εδώ.

Την κ. Ελισάβετ Βοργιά και την Κοινωφελή Δημοτική Επιχείρηση Πειραιά για την βοήθεια τους στα πρώτα μου επιστημονικά βήματα. Ήταν εκεί στην αρχή της επιστημονικής μου σταδιοδρομίας, υποστηρίζοντας και βοηθώντας με να χτίσω τα όνειρα μου. Χωρίς την κ.Ελισάβετ δεν θα ήμουν σήμερα εδώ.

ABSTRACT

Geothermometry is the extraction of temperature information from rocks using equilibrium phases whose chemical composition/interaction is sensitive to temperature variations. Mineral geothermometry is based on cation exchange between minerals and effectively reflects the closure temperature to diffusion (of cations between minerals) during cooling. Each geothermometer is designed for a specific purpose and has its own merits (mineral-melt equilibria for magma thermometry, inter-mineral equilibria for magmatic crystallization temperatures, metamorphic temperatures, subcontinental mantle geotherms, etc.). By combining geothermometers with geobarometers, it is possible to decipher the P-T path a rock has followed, in order to clarify the sequence of events that best describe its geological history.

The present thesis focuses on the Fe^{2+} -Mg cation exchange between coexisting orthopyroxene and spinel with the aim to create a robust geothermometer that can be applied primarily to mantle peridotites but also to other rock types from different geotectonic environments (e.g., mafic/ultramafic cumulates in layered intrusions and ophiolites, granulites, etc.). The first step of this procedure was the collection of experimental data on orthopyroxene-spinel equilibrium pairs from all available literature. As a result, a data base consisting of 1188 Opx-Spl experimental pairs culled from 103 publications was created. The experimental data span a temperature range from 800 to 1600°C and a pressure range from 0.001 to 80 kbar, covering a variety of chemical systems/starting compositions. Orthopyroxene and spinel were treated as octonary symmetric solutions comprising the endmembers En, Fs, Wo, Hd, MgTs, FeTs, MgCrTs and FeCrTs, and Spl, Hc, Chr, Mag, Mchr, Usp, Qnd and Mfr, respectively. After mathematical analysis through multilinear regression using matrix inversion, a new thermometric expression was derived for the Fe^{2+} -Mg cation exchange reaction between coexisting orthopyroxene and spinel:

$$T_{KG21}(^{\circ}K) = \frac{4930.98 + 205.58 \times P(kbar) + RT \ln(K_Y)}{R \ln(K_D)}, \text{ with } \ln(K_D) = \ln \left(\frac{\left(\frac{Fe^{2+}}{Mg} \right)_{Spl}}{\left(\frac{Fe_{M2}^{2+} \cdot Fe_{M1}^{2+}}{Mg_{M2} \cdot Mg_{M1}} \right)_{Opx}} \right)$$

$$RT \ln(K_Y) = 33678.88(X_{Hc} - X_{Spl}) + 25630.65 \times X_{Chr} - 6195.58 \times X_{Mchr} + 47258.56 \times X_{Mag} - 27969.63$$

$$\times X_{Mfr} + 105130.74 \times X_{Usp} - 93914.69 \times X_{Qnd} + 30410.81 \times (X_{En} - X_{Fs}) + 98894.14 \times X_{Di}$$

$$- 381529.99 \times X_{Hd} + 12886.55 \times X_{MgTs} + 180750.91 \times X_{MgCrTs} - 175575.25 \times X_{FeTs}$$

$$- 634363.98 \times X_{FeCrTs}$$

In addition, a recalibration of the Liermann and Ganguly (1993) thermometer was performed, aiming to further extend the P-T conditions of its applicability as well as its efficacy. The recalibrated thermometric formula is as follows:

$$T_{LG03.Rec} (^{\circ}K) = \frac{1714 + 81.05P(GPa) + 1856Y_{Cr}^{Spl} - 6462X_{Al}^{Opx} + 1851(Y_{Fe^{+3}}^{Spl} + Y_{Ti}^{Spl})}{\ln(K_D) + 0.39}$$

$$\text{With } \ln(K_D) = \ln \left(\frac{\left(\frac{Fe^{+2}}{Mg} \right)_{Spl}}{\left(\frac{Fe^{+2}}{Mg} \right)_{Opx}} \right)$$

ΠΕΡΙΛΗΨΗ

Η γεωθερμομετρία είναι η διαδικασία εξαγωγής πληροφοριών θερμοκρασίας από πετρώματα, χρησιμοποιώντας φάσεις σε θερμοδυναμική ισορροπία, των οποίων η χημική σύσταση/αλληλεπίδραση είναι ευαίσθητη στις μεταβολές της θερμοκρασίας. Η γεωθερμομετρία ορυκτών βασίζεται στην ανταλλαγή κατιόντων μεταξύ αυτών και ουσιαστικά αντικατοπτρίζει την θερμοκρασία κλεισίματος της διάχυσης (των κατιόντων μεταξύ των ορυκτών) κατά την ψύξη. Κάθε γεωθερμόμετρο σχεδιάζεται για έναν συγκεκριμένο σκοπό και έχει τα δικά του ιδιαίτερα χαρακτηριστικά (ισορροπία ορυκτού-τήγματος για θερμομετρία μάγματος, ισορροπία μεταξύ ορυκτών για θερμοκρασίες μαγματικής κρυστάλλωσης, μεταμορφικές θερμοκρασίες, γεώθερμες υπο-ηπειρωτικού λιθοσφαιρικού μανδύα κτλ.). Συνδυάζοντας γεωθερμόμετρα με γεωβαρόμετρα καθίσταται δυνατό να εξιχνιαστεί η πορεία πίεσης-θερμοκρασίας την οποία έχει ακολουθήσει ένα πέτρωμα, με σκοπό να διαλευκανθεί η ακολουθία γεγονότων η οποία περιγράφει καλύτερα την γεωλογική του ιστορία.

Η παρούσα διπλωματική εργασία εστιάζει στην ανταλλαγή κατιόντων $Fe^{2+}-Mg$ μεταξύ συνυπαρχόντων ορθοπυροξένου και σπινελίου, με σκοπό να δημιουργηθεί ένα στιβαρό γεωθερμόμετρο το οποίο θα μπορεί να εφαρμοσθεί κυρίως σε μανδουακούς περιδοτίτες, αλλά και σε τύπους πετρωμάτων διαφορετικών γεωτεκτονικών περιβαλλόντων (π.χ. μαφικούς/υπερμαφικούς σωρείτες σε στρωματόμορφες διεισδύσεις και οφιολίθους, γρανουλίτες, κτλ.). Το πρώτο βήμα της διαδικασίας αυτής ήταν η συλλογή πειραματικών δεδομένων ζευγών ορθοπυροξένου-σπινελίου που βρίσκονται σε ισορροπία, από όλη την διαθέσιμη βιβλιογραφία. Ως αποτέλεσμα, δημιουργήθηκε μια βάση δεδομένων από 1188 πειραματικά ζεύγη Opx-Spl που έχουν εξαχθεί από 103 δημοσιεύσεις. Το εύρος των πειραματικών δεδομένων κυμαίνεται από 800 έως 1600°C σε θερμοκρασία και από 0.001 έως 80 kbar σε πίεση, καλύπτοντας μια ποικιλία χημικών συστημάτων/αρχικών συστάσεων. Ο ορθοπυροξένος και ο σπινέλιος αντιμετωπίστηκαν ως οκταδικά συμμετρικά διαλύματα τα οποία περιλαμβάνουν τα ακραία μέλη En, Fs, Wo, Hd, MgTs, FeTs, MgCrTs and FeCrTs, και Spl, Hc, Chr, Mag, Mchr, Usp, Qnd and Mfr, αντιστοίχως. Έπειτα από μαθηματική ανάλυση μέσω πολλαπλής γραμμικής παλινδρόμησης χρησιμοποιώντας αντιστροφή πινάκων, δημιουργήθηκε μια νέα θερμομετρική έκφραση για την αντίδραση ανταλλαγής κατιόντων $Fe^{2+}-Mg$ μεταξύ συνυπαρχόντος ορθοπυροξένου και σπινελίου:

$$T_{KG21} (^{\circ}K) = \frac{4930.98 + 205.58 \times P(kbar) + RT \ln(K_{\gamma})}{R \ln(K_D)}, \quad \mu\epsilon \ln(K_D) = \ln \left(\frac{\left(\frac{Fe^{2+}}{Mg} \right)_{Spl}^2}{\left(\frac{Fe_{M2}^{2+} \cdot Fe_{M1}^{2+}}{Mg_{M2} \cdot Mg_{M1}} \right)_{Opx}} \right)$$

$$RT \ln(K_{\gamma}) = 33678.88(X_{Hc} - X_{Spl}) + 25630.65 \times X_{Chr} - 6195.58 \times X_{Mchr} + 47258.56 \times X_{Mag} - 27969.63 \\ \times X_{Mfr} + 105130.74 \times X_{Usp} - 93914.69 \times X_{Qnd} + 30410.81 \times (X_{En} - X_{Fs}) + 98894.14 \times X_{Di} \\ - 381529.99 \times X_{Hd} + 12886.55 \times X_{MgTs} + 180750.91 \times X_{MgCrTs} - 175575.25 \times X_{FeTs} \\ - 634363.98 \times X_{FeCrTs}$$

Επιπλέον εκτελέστηκε μια επαναβαθμονόμηση του γεωθερμομέτρου των Liermann and Ganguly (1993), με σκοπό να διευρυνθούν οι συνθήκες P–T εφαρμοσιμότητάς του αλλά και η αποτελεσματικότητά του. Η επαναβαθμονομημένη θερμομετρική εξίσωση έχει ως εξής:

$$T_{LG03.Rec} (^{\circ}K) = \frac{1714 + 81.05P(GPa) + 1856Y_{Cr}^{Spl} - 6462X_{Al}^{Opx} + 1851(Y_{Fe^{+3}}^{Spl} + Y_{Ti}^{Spl})}{\ln(K_D) + 0.39}$$

$$\mu\epsilon \ln(K_D) = \ln \left(\frac{\left(\frac{Fe^{+2}}{Mg} \right)_{Spl}}{\left(\frac{Fe^{+2}}{Mg} \right)_{Opx}} \right)$$

TABLE OF CONTENTS

Chapter 1: Geothermometry and Geobarometry	7
1.0 Introduction.....	7
1.1 Geothermometry – Theoretical background.....	7
1.2 Experimental petrology and application to thermometry.....	8
1.2.a. Instrumentation.....	8
1.2.b. Chemical systems and starting materials.....	8
1.2.c. Calibration.....	9
1.3. Thermometer Parameterization	10
1.3.a. Application of empirical corrections	10
1.3.b. Calculating the activity coefficients and ΔG^{XS}	11
Chapter 2: Experimental samples and Opx/Sp Thermometry	13
2.0. Introduction.....	13
2.1. Chemical content of experimental Orthopyroxene and Spinel.....	13
2.2. Chemical interaction of Opx/Sp.....	20
2.3. Opx/Sp equilibrium with Fe ²⁺ /Mg exchange.....	21
2.4. Effect of Al ⁺³ , Cr ⁺³ , Fe ⁺³ and Ti ⁺⁴ in Spinel with K_D	21
2.5. Formulation of Opx/Sp multicomponent solid solution with Margule parameters.....	24
2.6. T_{KG21} : A new Opx/Sp Geothermometer.....	26
2.7. Recalibration of Liermann and Ganguly Opx/Sp Thermometer.....	39
Chapter 3: Testing of T_{KG21}, $T_{LG03.Rec}$ and $T_{LG03.2.Ti}$ on Natural Samples	44
3.0. Introduction.....	44
3.1. Abyssal Peridotites.....	44
3.2. Continental Peridotites.....	46
3.3. Ophiolites.....	47
3.4. Discussion.....	49
References	51

Chapter 1 Geothermometry and Geobarometry

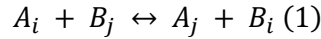
1.0. Introduction

Igneous and metamorphic processes are essentially controlled by variations in pressure (P) and temperature (T). Understanding P–T phase relationships is fundamental in unravelling such processes and enables us to eventually discriminate between different geotectonic environments. Experimental petrology provides the links between pressure, temperature, phase stability and composition.

Given mineral compositions, structure of crystal lattice and thermodynamics of solid solutions, it is possible to construct and test mineral solution models that best describe the experimental data. This is a major step forward in linking coexisting mineral compositions to P–T equilibration conditions via thermodynamics. Once this is established, it can lead to the development of mineral geothermometers and geobarometers.

1.1 Geothermometry – Theoretical background

Temperature is a crucial physical parameter that controls mineral nucleation, growth, solubility, reaction rates, elemental diffusivity and much more. Most cation exchange reactions are sensitive to temperature variations; hence they constitute good geothermometers. Cation exchange between minerals involves specific structural sites and takes place over a range of P–T conditions. In effect, the temperature calculated reflects closure to diffusion of the selected cations for the mineral pair considered. Assuming phases A and B are in equilibrium and exchange cations i and j between them, one can write (Anderson 2005):



Then, using chemical potentials:

$$\begin{aligned} \mu_{\text{reactans}} &= \mu_{\text{products}} \Rightarrow \\ \mu_{\text{products}} - \mu_{\text{reactans}} &= 0 \xrightarrow{\mu = \mu^0 + RT \ln a} \\ \mu_{\text{products}}^0 + RT \ln \alpha_{\text{products}} - \mu_{\text{reactans}}^0 - RT \ln \alpha_{\text{reactans}} &= 0 \Rightarrow \\ (\mu_{\text{products}}^0 - \mu_{\text{reactans}}^0) + \left(RT \ln \left(\frac{\alpha_{\text{products}}}{\alpha_{\text{reactans}}} \right) \right) &= 0 \quad (2) \end{aligned}$$

α_r^c : Activity (of component r in phase C)
 γ : Activity coefficient
X: Concentration
K: Equilibrium Constant
 G^{XS} : Gibbs free energy excess due to component mixing in a solid solution

$$\text{with, } K = \frac{\alpha_{\text{products}}}{\alpha_{\text{reactans}}} \rightarrow K = \frac{a_j^A \cdot a_i^B}{a_i^A \cdot a_j^B} \quad (3) \xrightarrow{\alpha = \gamma \cdot X}$$

$$K = \frac{\gamma_j^A \cdot X_j^A \cdot \gamma_i^B \cdot X_i^B}{\gamma_i^A \cdot X_i^A \cdot \gamma_j^B \cdot X_j^B} \Rightarrow$$

$$K = \frac{\gamma_j^A \cdot \gamma_i^B}{\gamma_i^A \cdot \gamma_j^B} \times \frac{X_j^A \cdot X_i^B}{X_i^A \cdot X_j^B} = K_\gamma \cdot K_D \quad (4) \xrightarrow{(2) \ \& \ \Delta\mu^0 = \Delta G}$$

μ : Chemical potential (J/mol)
T: Temperature (K)
P: Pressure (bar)
G: Gibbs free energy (J)
H: Enthalpy (J/mol)
S: Entropy (J/mol/K)
V: Volume (J/mol/bar)
R: Gas Constant (J/mol/K)

$$\Delta G + RT \ln(K_\gamma * K_D) = 0 \quad (5) \Rightarrow$$

$$\Delta G + RT \ln K_D + \ln K_\gamma = 0 \quad (6) \xrightarrow{\Delta G^{XS} = RT \ln(K_\gamma)}$$

$$\Delta G + RT \ln K_D + \Delta G^{XS} = 0 \quad (7)$$

At equilibrium:

$$\Delta G = \Delta H + P\Delta V - T\Delta S \quad (6) \xrightarrow{(7)}$$

$$0 = \Delta H + P\Delta V - T\Delta S + RT \ln K_D + \Delta G^{XS} \Rightarrow$$

$$T = \frac{\Delta H + P\Delta V + \Delta G^{XS}}{R \ln K_D - \Delta S} \quad (8)$$

1.2 Experimental petrology and application to thermometry

1.2.a. Instrumentation

Once the mathematical formula to calculate temperature (i.e., a geothermometer) is established, the next step is to determine all thermodynamic parameters (ΔS , ΔV , ΔH , ΔG^{XS}) involved in equation 8. In order to achieve this, analytical data on minerals produced in experiments at controlled P-T conditions are required as well as appropriate mineral solution models. Experimental petrology focuses on reproducing the geological conditions that occur in nature by testing the stability of rocks and minerals at various physicochemical conditions. Starting materials of known composition are tested in experimental laboratories equipped with sophisticated instruments designed to replicate the natural conditions.

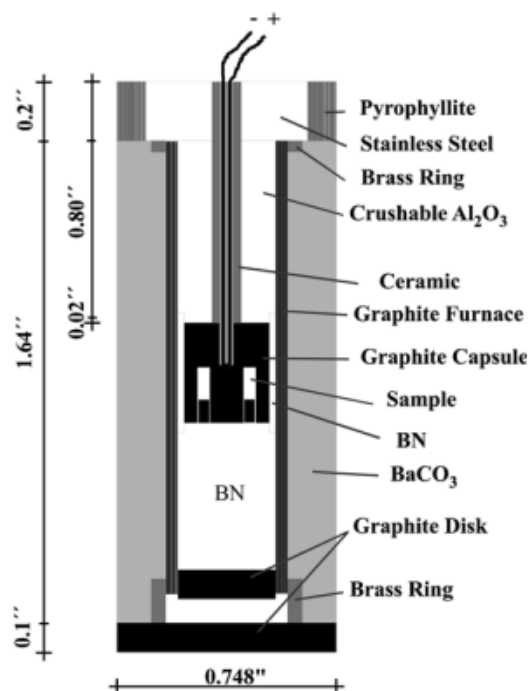


Figure 1: Schematic cross section of a typical pressure cell used in Fe^{2+} -Mg fractionation experiments in a piston-cylinder apparatus (Liermann and Ganguly 2003).

The experimental products are being studied and analysed employing several techniques such as Scanning Electron Microscopy / Back Scatter Electron Imaging in combination with Electron Probe Micro Analysis, Inductively Coupled Plasma-Mass Spectroscopy, etc..

1.2.b. Chemical systems and starting materials

An important stage in experimental petrology is the choice of the chemical system to be studied. The chemical system is represented by the elements that constitute the starting material. This has a direct correlation with the type of minerals that can be experimentally reproduced. For example, if we consider the MAS system (acronym of $MgO-Al_2O_3-SiO_2$), then no minerals containing FeO are expected. A test of the predictive power of synthetic system thermometers applied to coexisting orthopyroxene-clinopyroxene pairs against data from natural-system re-equilibration experiments is shown in Figure 2 (Bertrand and Mercier 1985).

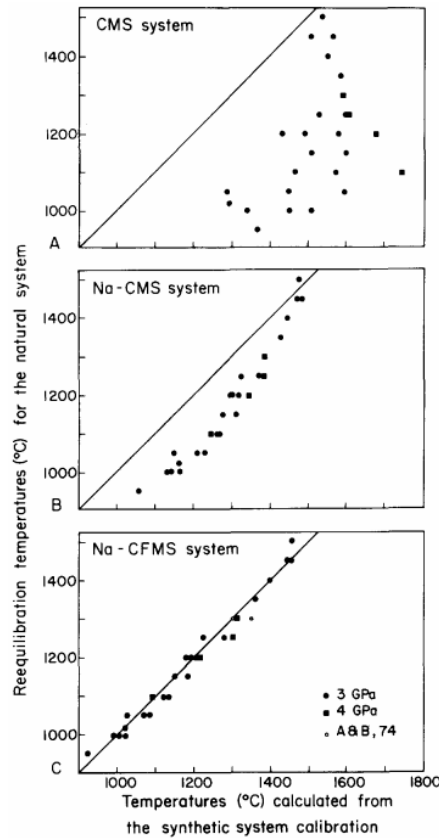


Figure 2: Synthetic systems with more components are more capable efficient in reproducing accurate and precise results.(Bertrand and Mercier 1985).

Obviously, the more oxides considered in a synthetic system, the closer we get to natural rock compositions. However, this increases the complexity of the system and requires more elaborate experimental conditions (e.g., to avoid Fe loss to the capsules). With regard to experiments on mantle materials, the CFMASCr system is considered adequate.

1.2.c. Calibration

Given the availability of experimental data conducted on a variety of appropriate starting materials at a range of temperature and pressure conditions, it is possible to extract the thermodynamic parameters of equation 8 for a specific cation exchange reaction between two minerals of interest. Firstly, some manipulation of equation 8 is necessary:

$$T = \frac{\Delta H + P\Delta V + \Delta G^{XS} \xrightarrow{\Delta G^{XS}=0}}{R \ln K - \Delta S}$$

$$RT \ln K_D - T\Delta S = \Delta H + P\Delta V \Rightarrow$$

$$\ln K_D = \frac{\Delta H}{R} \cdot \frac{1}{T} + \frac{\Delta V}{R} \cdot \frac{P}{T} + \frac{\Delta S}{R} \quad (9)$$

Equation 9 is a simple equation of the form: $y = \alpha_0 + \alpha_1 x_1 + \alpha_2 x_2$ where $\alpha_0 = \frac{\Delta S}{R}$, $\alpha_1 = \frac{\Delta H}{R}$, $\alpha_2 = \frac{\Delta V}{R}$, $x_1 = \frac{1}{T}$, $x_2 = \frac{P}{T}$ and can be solved for by using multiple linear regression. An example of parameter fitting for $Fe^{2+}-Mg$ exchange between mantle peridotite minerals using this technique is given below (Brey and Köhler 1990).

Fitting parameters of Fe–Mg exchange relations

Pair	$\Delta H/R$	$\Delta S/R$	$\Delta V/R$
ol/opx	-134 (± 148)	-0.08 (± 0.11)	-2.73 (± 1)
ol/cpx	-1489 (± 148)	-1.07 (± 0.11)	-4.64 (± 1.1)
opx/cpx	-1354 (± 85)	-0.99 (± 0.06)	-2.15 (± 0.6)
grt/ol	-1350 (± 144)	-0.51 (± 0.11)	-7.86 (± 1.7)
grt/opx	-1456 (± 120)	-0.55 (± 0.09)	-9.86 (± 1.4)
grt/cpx	-2862 (± 143)	-1.57 (± 0.11)	-11.67 (± 1.7)

Figure 3: ol: Olivine, opx: Orthopyroxene, cpx: Clinopyroxene, grt: Garnet

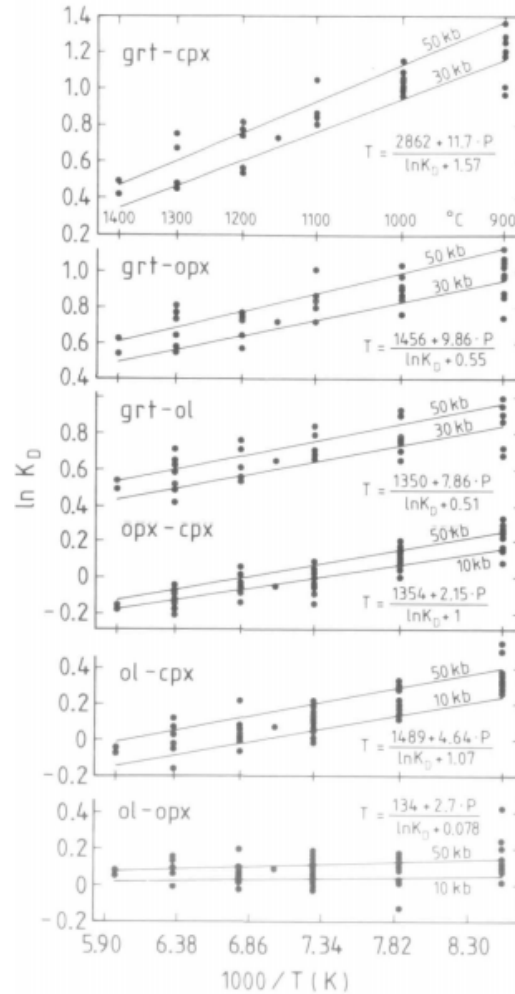


Figure 4: $\ln K_D$ vs reciprocal temperature based on the fitting parameters of figure 3.

Sensitivity to temperature is demonstrated by well sloping fits on an $\ln K_D$ vs. $1/T$ graph. From Figure 4 it appears that the ol/opx calibration is not a good thermometer (flat trend), whereas the grt/cpx calibration exhibits the best Fe^{2+} –Mg fractionation with respect to temperature.

1.3. Thermometer Parameterization

1.3.a. Application of empirical corrections

Commonly, in thermobarometry, it is necessary to apply some empirical corrections related to the presence of certain major/minor elements and/or theoretical mineral endmembers of seemingly secondary importance that were not used in the primary calibration. The latter effectively account for cation exchange between sites yielding interaction parameters that improve the linear fit to temperature. A good example is Taylor’s two-pyroxene thermometer (Taylor 1998):

$$T(K) = \frac{24787 + 678 * P(GPa)}{15.67 + 14.37 * Ti^{cpx} + 3.69 * Fe^{cpx} - 3.25 * X_{TS} + (\ln K_D)^2} \quad (9)$$

where addition of terms to correct for the effect of Ti, ferrous iron in clinopyroxene and Tschermak's components on the width of the pyroxene miscibility gap improved the fit. In this thermometer, an increase in Ti^{cpx} and Fe^{cpx} lowers the estimated temperature. By contrast, an increase in X_{TS} increases the estimated temperature.

1.3.b. Calculating the activity coefficients and ΔG^{XS}

Up until now, in the procedure to determine the values of the thermodynamic parameters present in equation (8), any excess of the Gibbs free energy due to component mixing in solid solutions has been neglected. This is common practice in geothermometer calibrations where it is often assumed that the system is adequately described by G^{ideal} . However, if we consider, for example, $Fe^{2+}-Mg$ fractionation between orthopyroxene and clinopyroxene, there are multiple endmember components that can be calculated by mixing on sites. (see Figure 5, Morimoto 1989).

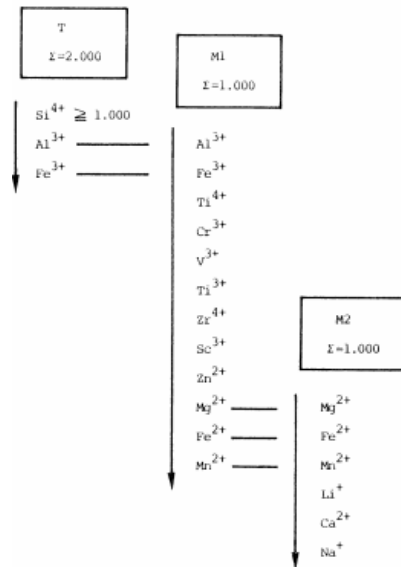
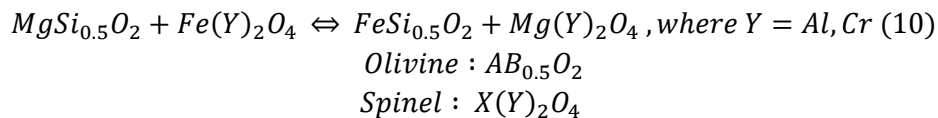


Figure 5: Flow chart showing the ideal site occupancy in the site T, M1 and M2 for cations in Pyroxenes

Although many of the possible theoretical endmembers are thermodynamically insignificant (due to the weak interactions they represent, hence showing low energy contributions), ΔG^{XS} must be calculated for the most prominent ones. A procedure to calculate ΔG^{XS} is by creating generalized Margules-type formulations. First, we need to classify the mineral solid solutions involved in a thermometer as symmetrical or asymmetrical. For instance, the equilibrium $Fe^{2+}-Mg$ exchange reaction between olivine and spinel may be written as (Engi 1983):



There are two possible cation exchanges:

- 1) Mg is only active to olivine where it substitutes the site X of Spinel, while Fe in Spinel substitutes the site X of Olivine.
- 2) There is additionally reciprocal exchange.

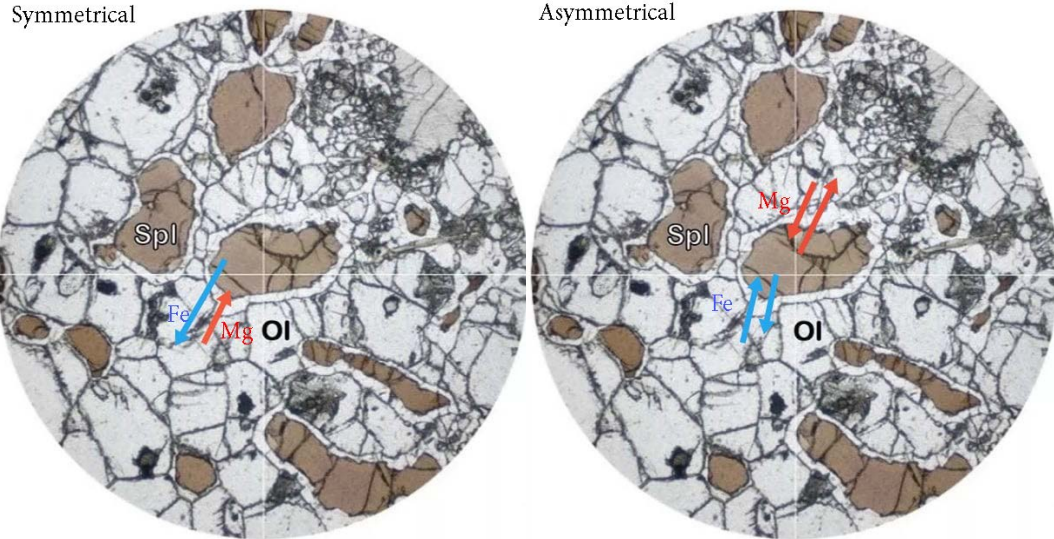


Figure 6: Two different interactions in Olivine Spinel exchange.(photo of Spinel Lherzolite, Spain, <https://www.virtualmicroscope.org/content/m19-spinel-lherzolite-spain>)

Activity coefficients and G^{XS} may be calculated as follows (Mukhopadhyay 1993 et al):

For the symmetrical case:

$$G^{XS} = \sum_{i < j}^n W_{ij} X_i X_j \quad (11)$$

$$RT \ln(\gamma_i) = \sum_{\substack{j=1 \\ j \neq i}}^n W_{ij} X_j - G^{XS} \quad (12)$$

i, j are different components, n = sum of components

W_{ij} : Margules parameter between i, j interaction

Where in symmetric solutions $W_{ij} = W_{ji}$ (13)

For the asymmetrical case:

$$G^{XS} = \sum_i^n \sum_{<j}^n X_i X_j [X_j W_{ij} + X_i W_{ji}] + \sum_i^n \sum_{<j}^n \sum_{<k}^n X_i X_j X_k C_{ijk} \quad (14)$$

$$RT \ln(\gamma_i) = 2 \sum_{\substack{j=1 \\ j \neq i}}^n X_i X_j W_{ji} + \sum_{\substack{j=1 \\ j \neq i}}^n X_j^2 W_{ij} + \sum_{\substack{j \\ j \neq i}}^n \sum_{\substack{k \\ k \neq i}}^n X_j X_k C_{ijk} - 2G^{XS} \quad (15)$$

i, j, k are different components

C_{ijk} : Margules parameter with i, j, k interaction

In asymmetric solutions $W_{ij} \neq W_{ji}$ (16)

If there are $n < 3$ components, then C_{ijk} is neglected

Chapter 2 Experimental samples and Opx/Sp Thermometry

2.0. Introduction

In this chapter are going to be presented the experimental samples with Orthopyroxene-Spinel interaction throughout the accessible literature. From 158 experimental analysis/publications, the 103 contain Orthopyroxene-Spinel pairs, in which 1188 samples had been found. Also, a new thermometer with Fe^{2+}/Mg exchange and a recalibration of Liermann's and Ganguly's thermometer are going to be presented. The aim of this chapter is the understanding of Opx/Sp chemical system interaction and their temperature relation via the experimental analysis that has been done, in order to create a formulation that calculates temperature in natural samples.

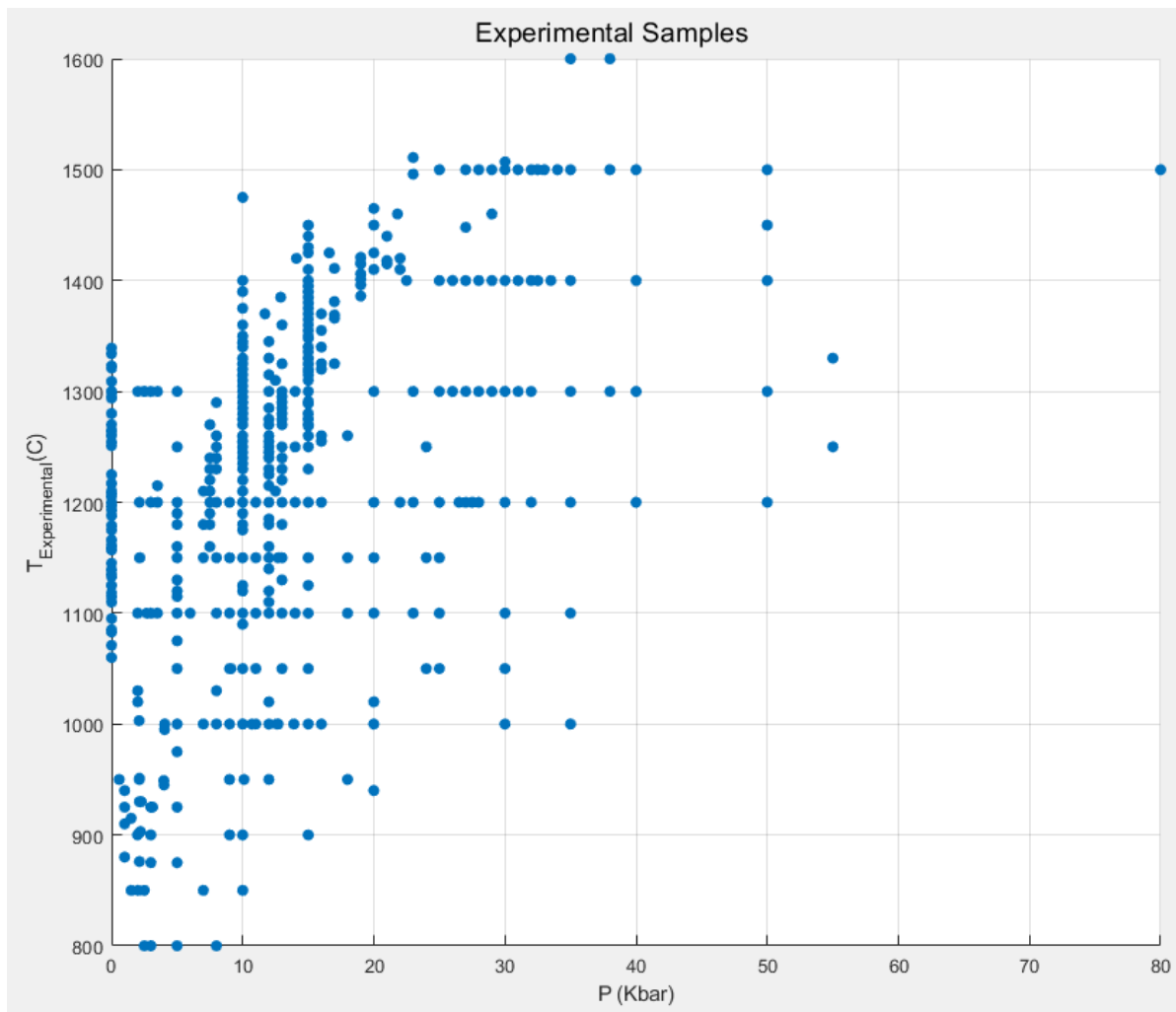
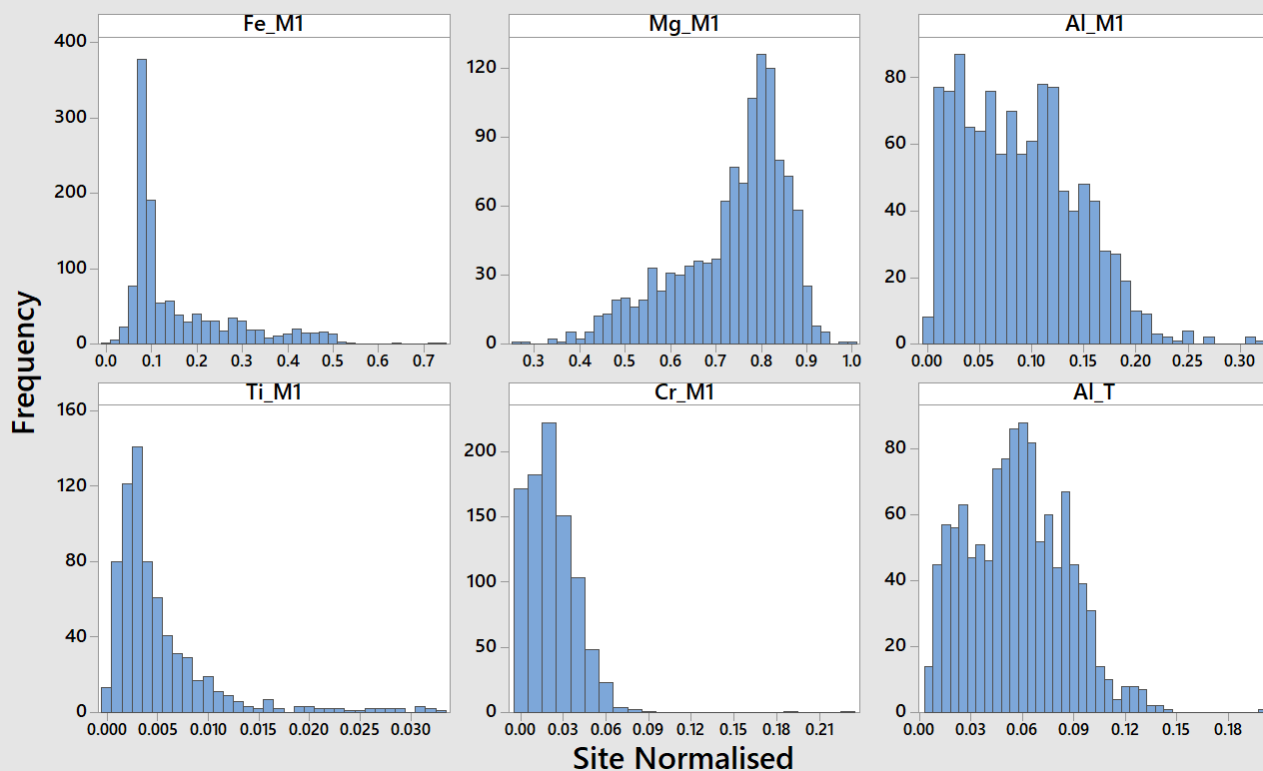


Figure 7: P-T Graph of Opx/Sp pairs of the collected experimental samples from all the accessible literature.

2.1. Chemical content of experimental Orthopyroxene and Spinel

The chemical composition of both Orthopyroxene and Spinel are the following:

Chemical Distribution of Orthopyroxene Site M1



Chemical Distribution of Orthopyroxene Site M2

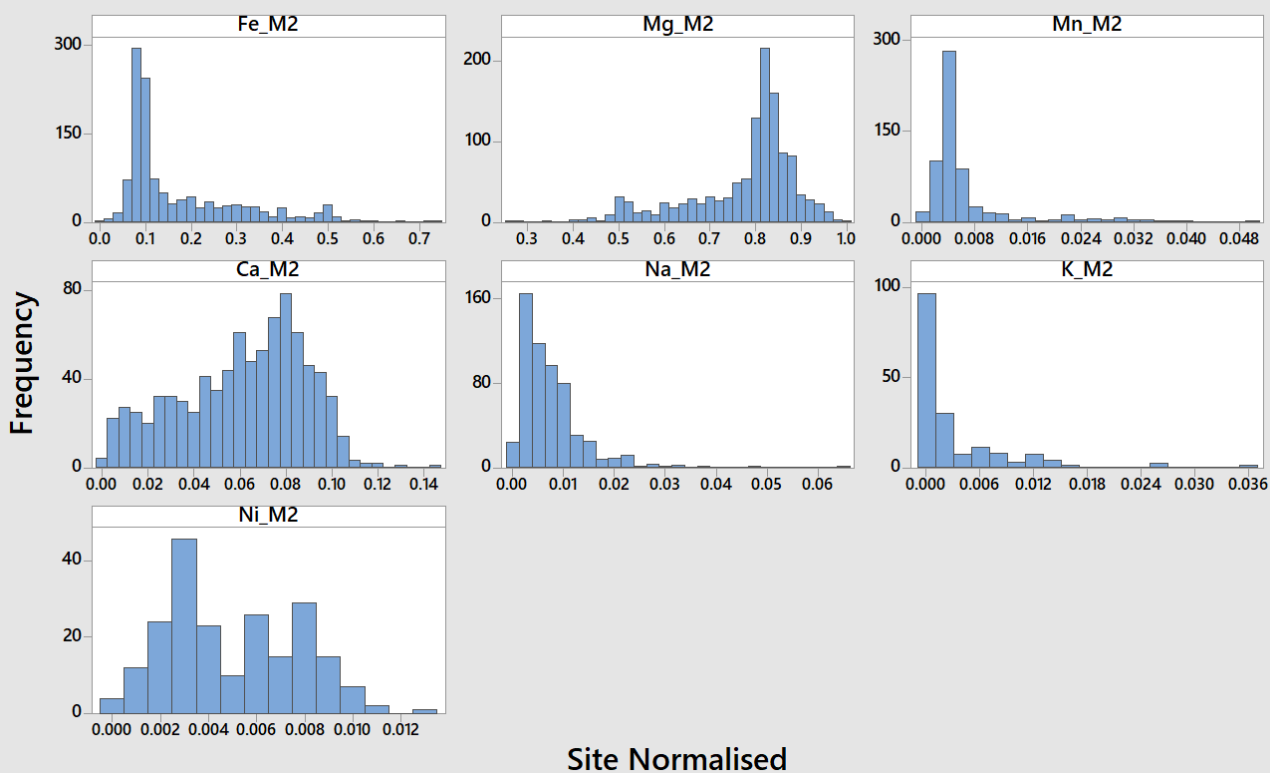


Figure 8: Histograms that depict the chemical distribution of Orthopyroxene in the mineral sites.

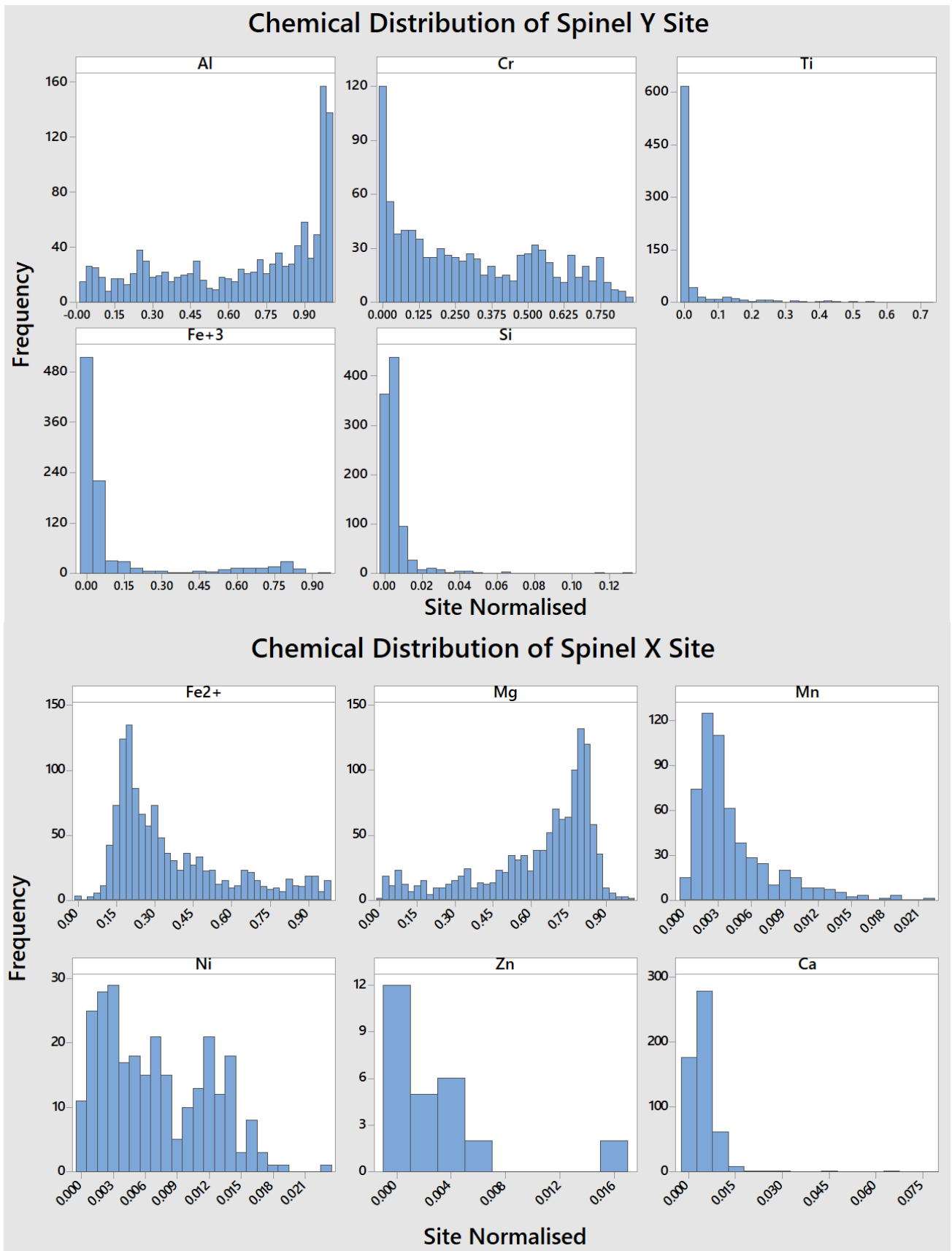


Figure 9: Histograms that depict the chemical distribution of Spinel in the mineral sites.

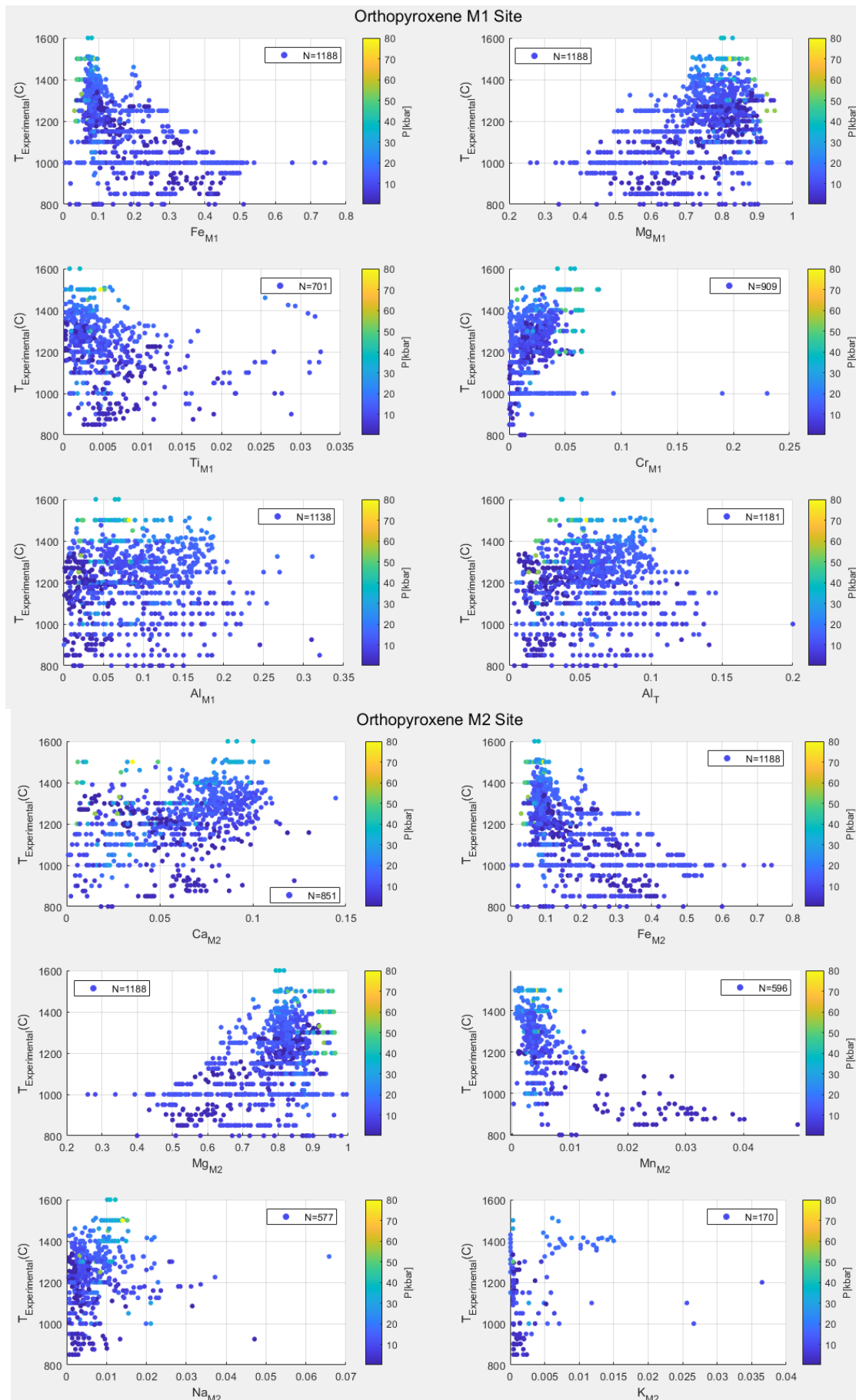


Figure 10: P-T-X Scatterplots that depict P-T relation of cations in Orthopyroxene mineral sites.

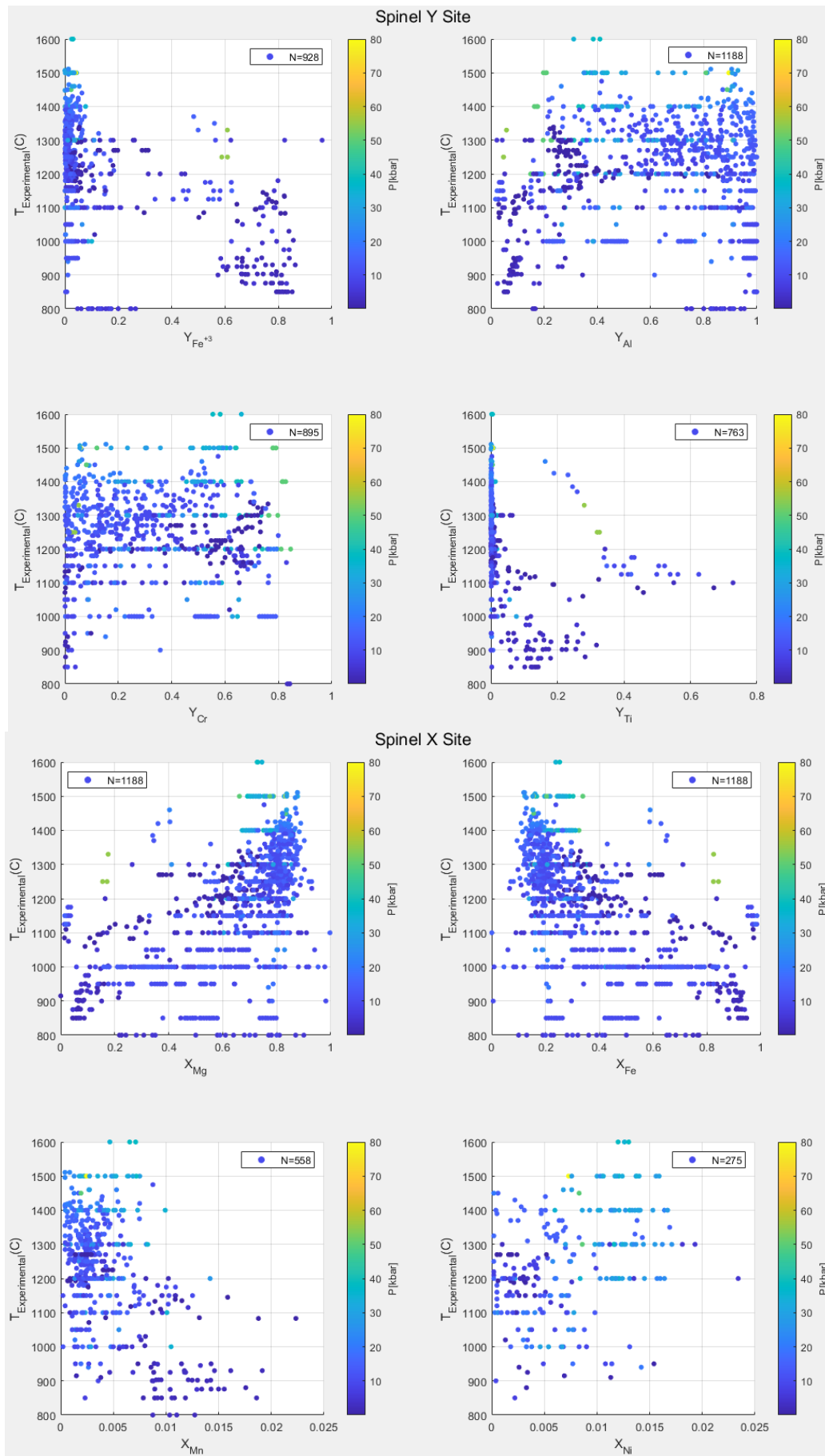
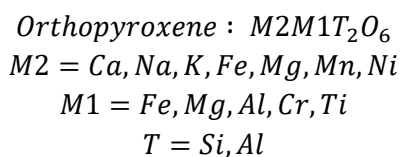


Figure 11: *P-T-X* Scatterplots that depict *P-T* relation of cations in Spinel mineral sites.

The site normalization for Orthopyroxene is has been calculated by this procedure:



In these site occupancies Fe, Mg, and Al can be in more than two sites, so those cations are treated as following:

$$All\ Fe = Fe_{sum} = Fe^{+2}$$

$$Fe_{M_1} = \left(\frac{Fe_{sum}}{Mg_{sum}} \right) * \frac{3 - Al - Ti - Cr - Fe_{sum}}{\frac{Fe_{sum}}{Mg_{sum}} + 1} \quad (16)$$

$$Fe_{M_2} = \left(\frac{Fe_{sum}}{Mg_{sum}} \right) * \left(Mg_{sum} - \frac{3 - Al - Si - Ti - Cr}{\frac{Fe_{sum}}{Mg_{sum}} + 1} \right) \quad (17)$$

$$Mg_{M_1} = \frac{3 - Al - Ti - Cr - Fe_{sum}}{\frac{Fe_{sum}}{Mg_{sum}} + 1} \quad (18)$$

$$Mg_{M_2} = Mg_{sum} - \frac{3 - Al - Si - Ti - Cr}{\frac{Fe_{sum}}{Mg_{sum}} + 1} \quad (19)$$

$$Al_{M_1} = IF \left(Al_{sum} - (2 - Si) < 0, 0, IF(Si > 2, Al_{sum}, Al_{sum} - (2 - Si)) \right) \quad (20)$$

$$Al_T = IF(1 - 0.5 * Si < 0, 0, 1 - 0.5 * Si) \quad (21)$$

$$Si_T = 0.5 * Si \quad (22)$$

After the calculations from equations 16-22 have been completed, then the normalization is the following:

for cation Z in M1 site

$$Z_{M_1} = \frac{Z}{Fe_{M_1} + Mg_{M_1} + Al_{M_1} + Cr + Ti} \quad (23)$$

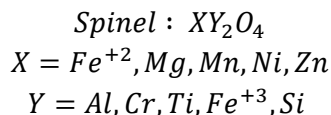
for cation X in M2 site

$$X_{M_2} = \frac{X}{Fe_{M_2} + Mg_{M_2} + Ca + Na + K + Mn + Ni} \quad (24)$$

for cation Y in T site

$$Y_T = \frac{Y}{Al_T + Si_T} \quad (25)$$

The site normalization for Spinel has been calculated by this procedure:



for cation A in X site:

$$A_X = \frac{A}{Fe^{+2} + Mg + Mn + Ni + Zn} \quad (26)$$

for cation B in Y site:

$$Fe^{+3} = IF \left(8 * \left(1 - \frac{3}{Total_{norm}} \right) < 0, 0, 8 * \left(1 - \frac{3}{Total_{norm}} \right) \right) (Droop 1987) (27)$$

$$B_Y = \frac{B}{Al + Cr + Ti + Fe^{+3} + Si} (28)$$

In figures 8, 9 it is shown the chemical content of Orthopyroxene and Spinel. Characterization of chemical distributions for each cation in chemical sites is the following:

Orthopyroxene in Site M1

- Fe : A skewed right distribution with peak at 0.08 and chemical range of 0-0.74.
- Mg: A skewed left distribution with peak at 0.8 and chemical range of 0.26-1.00.
- Al : A skewed right distribution, the bulk of the samples are 0.005-0.165 and the chemical range is 0-0.32.
- Ti : A skewed right distribution with peak at 0.003 and chemical range of 0-0.03.
- Cr : A normal distribution with peak at 0.02 ,with some outliers at 0.19-0.23 and a chemical range of 0-0.23.

Orthopyroxene in Site M2

- Fe : A skewed right distribution with peak at 0.08 and chemical range of 0.005-0.74.
- Mg: A skewed left distribution with peak at 0.82 and chemical range of 0.26-0.995.
- Mn: A skewed right distribution with peak at 0.004 and chemical range of 0-0.049.
- Ca : A skewed left distribution with peak at 0.08, the bulk is in range 0.005-0.100 and the chemical range is 0-0.144.
- Na : A skewed right distribution with peak at 0.0025 and chemical range of 0-0.0658.
- K : A logarithmic type right distribution with peak near 0 and chemical range of 0-0.0365.
- Ni: A bimodal distribution with a high peak at 0.003 and a lower at 0.008 with chemical range of 0-0.0126.

Spinel in Site Y

- Al : A logarithmic type left distribution with peak at 0.97 and chemical range of 0.02-1.00.
- Cr : A logarithmic type right distribution with peak near 0 and a chemical range of 0-0.84.
- Ti : A logarithmic type right distribution with peak near 0 and a chemical range of 0-0.73.
- Fe⁺³ : A bimodal distribution with a logarithmic type right distribution and peak near 0, and a second small bulk of samples with range of 0.45-0.85. The overall chemical range is 0-0.96.
- Si: A skewed right distribution with peak at 0.005 and chemical range of 0-0.128.

Spinel in Site X

- Fe⁺²: A skewed right distribution with peak at 0.4 and chemical range of 0-0.98.
- Mg : A skewed left distribution with peak at 0.8 and chemical range of 0-1.00.
- Mn : A skewed right distribution with peak at 0.002 and chemical range of 0-0.022.
- Ni : A bimodal distribution with a high peak at 0.003 and a lower peak at 0.012. The overall chemical range is 0-0.023.
- Zn : A skewed distribution with high peak near 0 and a chemical range of 0-0.0165.
- Ca : A normal distribution with peak at 0.005 and chemical range of 0-0.065.

In the above Scatterplots (Figure 10, 11) it is shown that there is a relation of temperature with Fe^{2+} and Mg in both Orthopyroxene and Spinel. In Opx, Fe^{2+} content decreases as temperature rises in both M1 and M2 site, whereas in Mg content there is the opposite effect, while in spinel there is the same phenomenon but with a different trend. It should be mentioned here that it is not appeared in the diagrams any significant relation of pressure with the Fe/Mg trends in both minerals.

Moreover, can be seen trends in other cations too. In orthopyroxene it seems that there is a correlation of temperature with Cr and Ti in M1 site and with Mn in site M2. Chromium has a positive correlation with temperature, in contrast with Ti and Mn. Also in Spinel there are correlations with Fe^{+3} and Ti in Y site and with Mn in X site, where there is a negative relation to temperature.

2.2. Chemical interaction of Opx/Sp

Orthopyroxene's and Spinel's interaction is not only in Fe^{+2} and Mg but in other cations as well. It is shown that there is an exchange with Al^{+3} and Cr^{+3} . The interaction of these 4 cations is portrayed in the figure below. The content of Fe^{+2} has a positive correlation in Opx/Sp and they follow the same pattern with temperature. As temperature is dropping, the content of Fe^{+2} is rising in both minerals. The same thing has been observed in Mg but with the opposite effect from temperature. As it is presented in figures 10-11, Fe^{+2} and Mg in both minerals have the same relation in temperature, but the trend is different, so the diffusion rate is expected to be different in relation to temperature. Alumina's interaction has a strong correlation that seems like a natural logarithmic interaction that is not derived strongly by temperature. Chromium's interaction on the other hand seems to have a very strong correlation and exchange rate which is not derived by temperature, but it appears that the Cr_{opx} increases and Cr_{sp} is constant the temperature rises. So there is a correlation with temperature and chromium content.

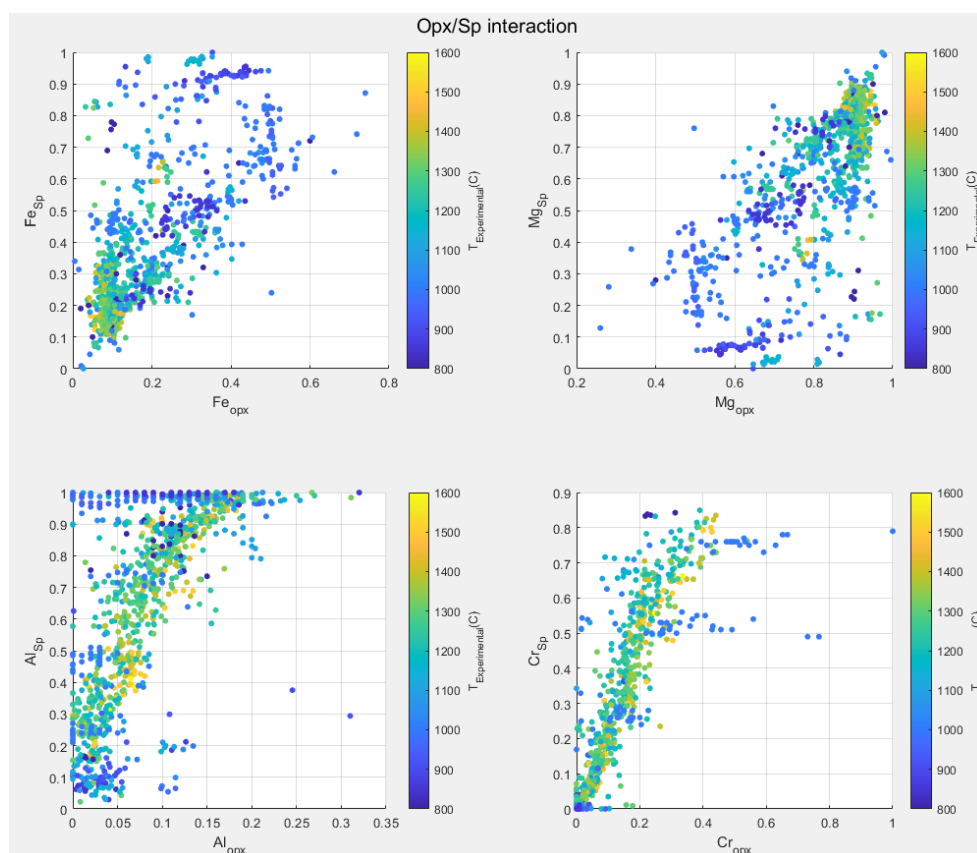
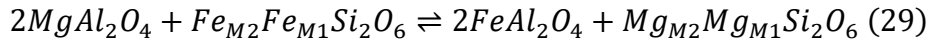


Figure12: Chemical interaction of Opx/Sp in Fe, Mg, Al and Cr. For mineral $c=\{\text{Opx,Sp}\}$, $\text{Fe}_c=\text{Fe}/(\text{Mg}+\text{Fe})$, $\text{Mg}_c=\text{Mg}/(\text{Mg}+\text{Fe})$, $\text{Cr}_c=\text{Cr}/(\text{Cr}+\text{Al})$, $\text{Al}_{\text{opx}}=\text{Al}_{\text{M1}}$ and $\text{Al}_{\text{sp}}=\text{Al}_Y$.

2.3. Opx/Sp equilibrium with Fe²⁺/Mg exchange

The reaction between Orthopyroxene and Spinel with Fe²⁺/Mg exchange is as follows:



Many exchange reaction thermometers have been expressed in a simpler way for the cation exchange of orthopyroxene for the simplicity of the method of calculating the constant equilibrium and consequently the creation of the thermometric model (Liermann & Ganguly 2003, Mukherjee 2010 et al). But in this way the complexity of orthopyroxene exchange sites is ignored. In this thermometric expression the complexity of orthopyroxene in the distribution of magnesium iron is included. By having (28) as equilibrium the constant parameter is has been calculated by the following procedure:

$$K = \frac{\alpha_{FeAl_2O_4}^{Spl} \cdot \alpha_{Mg_{M2}M1Si_2O_6}^{Opx}}{\alpha_{MgAl_2O_4}^{Spl} \cdot \alpha_{Fe_{M2}M1Si_2O_6}^{Opx}} = \frac{X_{FeAl_2O_4}^{Spl} \cdot X_{Mg_{M2}M1Si_2O_6}^{Opx}}{X_{MgAl_2O_4}^{Spl} \cdot X_{Fe_{M2}M1Si_2O_6}^{Opx}} \times \frac{\gamma_{FeAl_2O_4}^{Spl} \cdot \gamma_{Mg_{M2}M1Si_2O_6}^{Opx}}{\gamma_{MgAl_2O_4}^{Spl} \cdot \gamma_{Fe_{M2}M1Si_2O_6}^{Opx}} = K_D \cdot K_Y \quad (30)$$

$$K_D = \frac{(X_{Fe}^{Spl})^2 \cdot (X_{Al}^{Spl})^4 \cdot (X_{Mg,M2}^{Opx}) \cdot (X_{Mg,M1}^{Opx}) \cdot (X_{Si,T}^{Opx})^2}{(X_{Mg}^{Spl})^2 \cdot (X_{Al}^{Spl})^4 \cdot (X_{Fe,M2}^{Opx}) \cdot (X_{Fe,M1}^{Opx}) \cdot (X_{Si,T}^{Opx})^2} = \frac{(X_{Fe}^{Spl})^2 \cdot (X_{Mg,M2}^{Opx}) \cdot (X_{Mg,M1}^{Opx})}{(X_{Mg}^{Spl})^2 \cdot (X_{Fe,M2}^{Opx}) \cdot (X_{Fe,M1}^{Opx})}$$

$$K_D = \frac{\left(\frac{Fe^{2+}}{Mg}\right)_{Sp}^2}{\left(\frac{Fe_{M2}^{2+} \cdot Fe_{M1}^{2+}}{Mg_{M2} \cdot Mg_{M1}}\right)_{Opx}} \quad (31)$$

In equations 29-30 there is the activity coefficient of each chemical component. In order to further calculate the activity coefficients, the components partitioning in the system must first be selected. So to do that the cations that orthopyroxene and Spinel have interaction, and cations that have an effect in equilibrium are needed to formulate an activity coefficient model.

2.4. Effect of Al³⁺, Cr³⁺, Fe³⁺ and Ti⁴⁺ in Spinel with K_D

The effect of Chromium in Spinel for thermometry has been discussed by many researchers (Engi 83, Mukherjee 90 et al, Liermann & Ganguly 03) regarding the mixing behavior of Fe-Mg. Most of them have concluded that it makes the equilibrium fractionation less ideal as the Chromium content in Spinel increases. Moreover, it has been observed that as the Chromium content increases, K_D tilts vertically. The equilibrium (28) tends to the products, as the Y_{Cr^{Sp}} rises in an isothermic environment. Furthermore, Chromium seems to have a thermometric relation as well. It appears that as the Temperature rises, Chromium has less effect in K_D than in lower Temperatures. Hence the Chromium is proven to be a necessary Thermometric descriptor that shows a differentiated linear relation to temperature. So, in order to calibrate the Fe²⁺-Mg thermometric interaction, Chromium in the multicomponent solution equation oughts to be included, because the function of K_D is Chromium dependent.

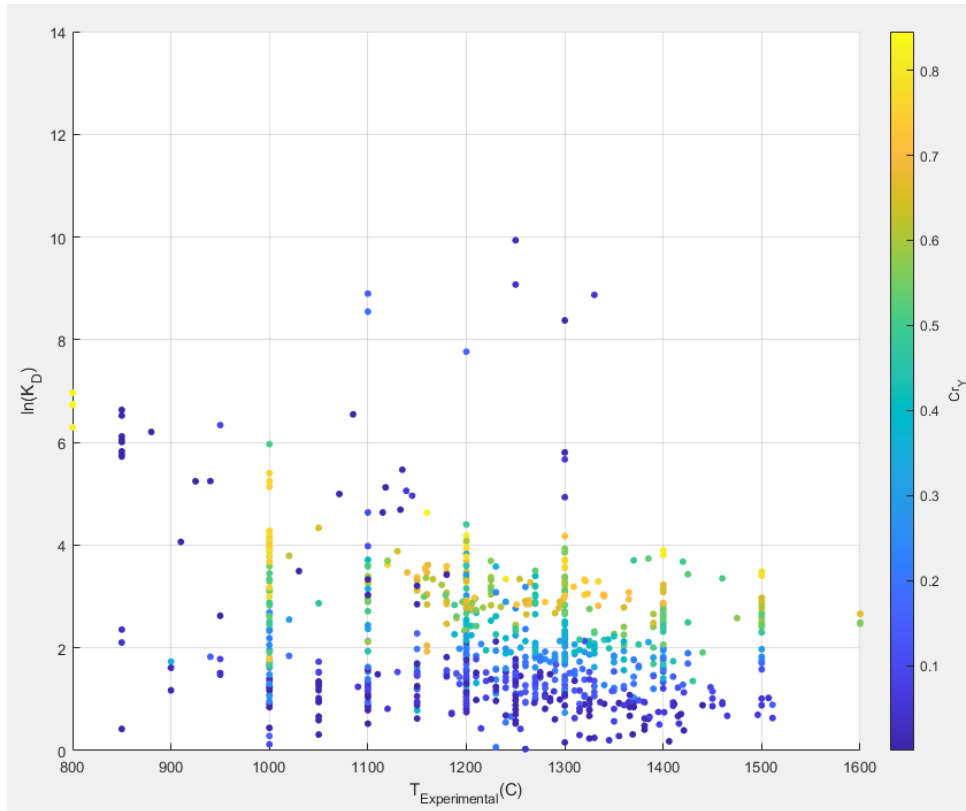


Figure 13: Plot of $\ln K_D$ vs $T_{\text{experimental}}$ with a colorbar of $Y_{\text{Cr}}^{\text{Sp}}$. It is shown that K_D is derived by the content of Chromium in Spinel.

Same interaction it appears that other cations have with K_D . It is found that Ti^{+4} and Fe^{+3} have a similar effect in K_D . In figure 14 it is presented that there is a dependence of Fe^{+3} as temperature stays stable. This effect seems that has a different ratio as temperature rises. The same case is with Ti^{+4} as presented in Figure 15.

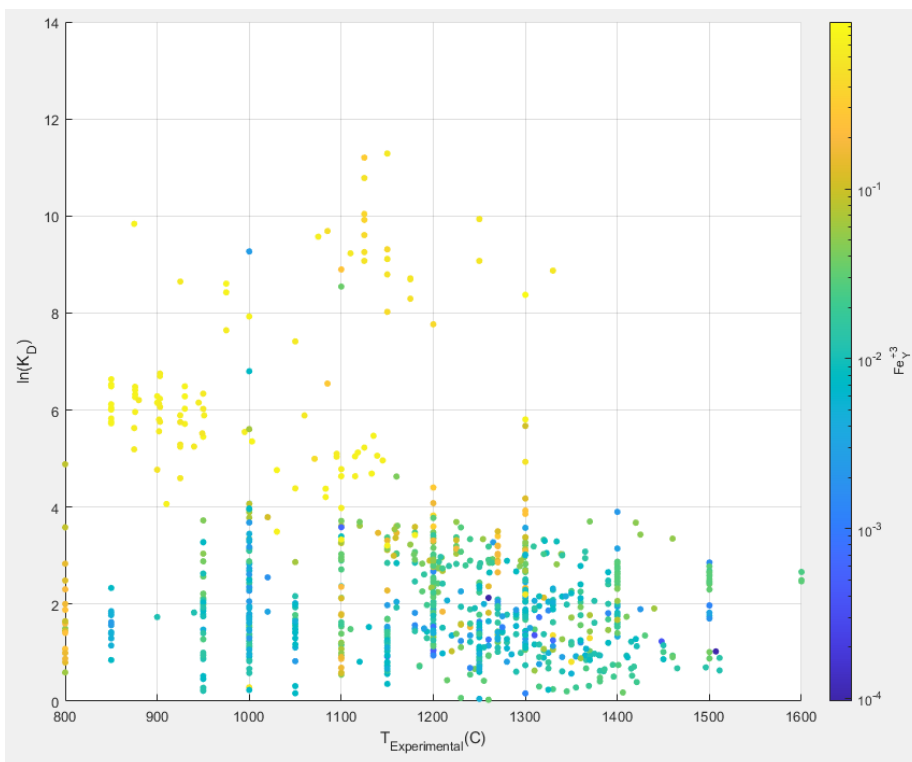


Figure 14: Plot of $\ln K_D$ vs $T_{\text{experimental}}$ with a logarithmic colorbar of Fe^{+3}_Y . It is shown that K_D is derived by the content of trivalent Iron in Spinel.

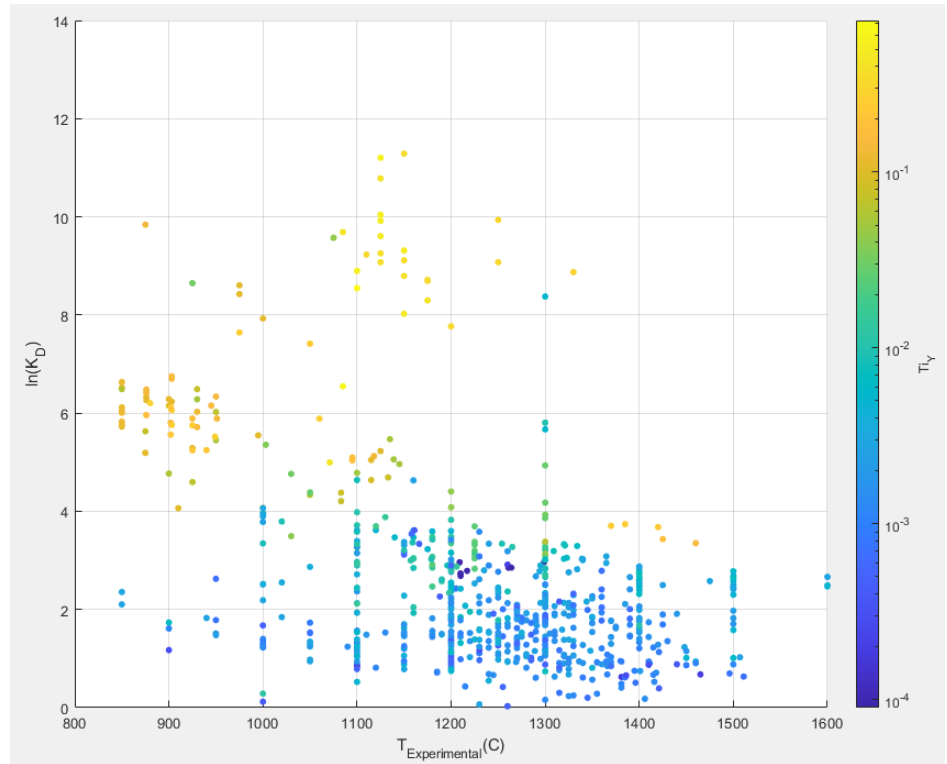


Figure 15: Plot of $\ln K_D$ vs $T_{\text{experimental}}$ with a logarithmic colorbar of Fe^{+3}_Y . It is shown that K_D is derived by the content of Titanium in Spinel.

In addition, it is known that Al^{+3} is primary content in Spinel that has a strong correlation with temperature. In the addition of other cations into Y site it has been shown that K_D rises vertically, but the opposite happened with Al^{+3} as expected cause of Cr^{+3} , Fe^{+3} and Ti^{+4} substitution effect.

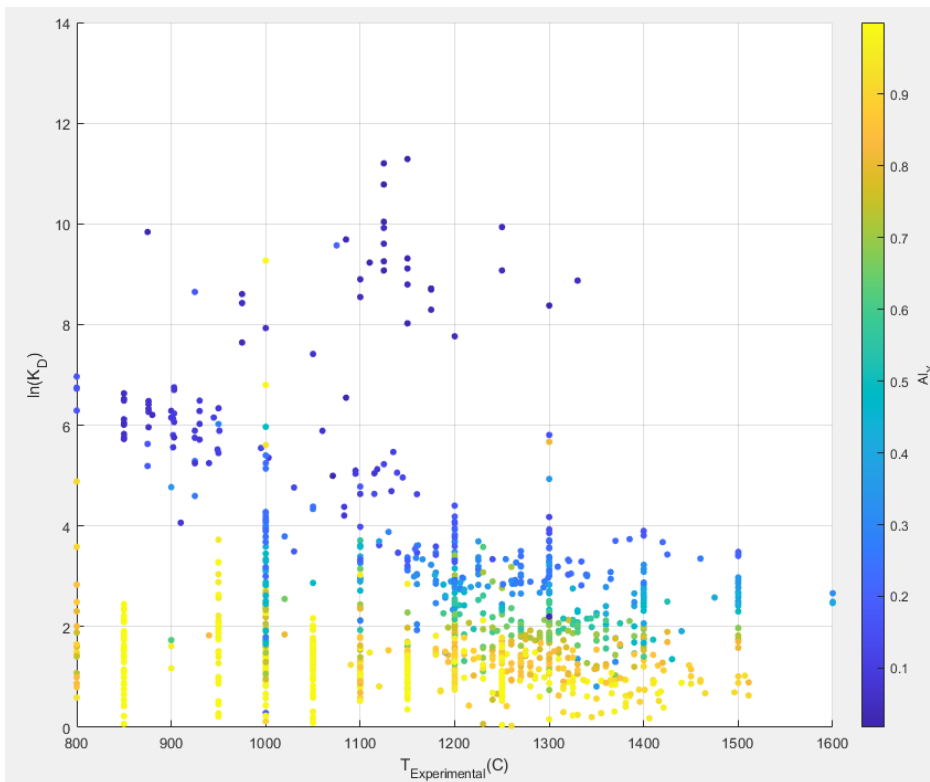


Figure 16: Plot of $\ln K_D$ vs $T_{\text{experimental}}$ with a logarithmic colorbar of Fe^{+3}_Y . It is shown that K_D is derived by the content of Aluminum in Spinel.

In conclusion, according to paragraph 2.2., Al^{+3} and Cr^{+3} have an exchange betwixt Opx and Sp, while there is dependence with temperature. So end members that contain Al^{+3} and Cr^{+3} in both minerals are going to be included. Furthermore after an interaction was found between the K_D and cations Fe^{+3} and Ti^{+4} in spinel, the cations will also be inserted into multicomponent formulation as well. Finally Ca^{+} in Orthopyroxene will be included too, because is a primary element that occupies M2 site.

2.5. Formulation of Opx/Sp multicomponent solid solution with Margule parameters

Based on the cations that have been selected, the end members that are included in the Margule formulation are the following:

Table1: End members for Orthopyroxene

n	Name	Abb.	Chem. Formula	Activity
1	<i>Ferrosilite</i>	<i>Fs</i>	$Fe_2Si_2O_6$	$(X_{Fe,M2}^{Opx}) \cdot (X_{Fe,M1}^{Opx}) \cdot (X_{Si,T}^{Opx})^2$
2	<i>Enstatite</i>	<i>En</i>	$Mg_2Si_2O_6$	$(X_{Mg,M2}^{Opx}) \cdot (X_{Mg,M1}^{Opx}) \cdot (X_{Si,T}^{Opx})^2$
3	<i>Diopside</i>	<i>Di</i>	$CaMgSi_2O_6$	$(X_{Ca,M2}^{Opx}) \cdot (X_{Mg,M1}^{Opx}) \cdot (X_{Si,T}^{Opx})^2$
4	<i>Hedenbergite</i>	<i>Hd</i>	$CaFeSi_2O_6$	$(X_{Ca,M2}^{Opx}) \cdot (X_{Fe,M1}^{Opx}) \cdot (X_{Si,T}^{Opx})^2$
5	<i>Mg Tschermak's</i>	<i>MgTs</i>	$MgAl_2SiO_6$	$4 \cdot (X_{Mg,M2}^{Opx}) \cdot (X_{Al,M1}^{Opx}) \cdot (X_{Al,T}^{Opx}) \cdot (X_{Si,T}^{Opx})$
6	<i>Mg – Cr Tschermak's</i>	<i>MgCrTs</i>	$MgCrAlSiO_6$	$4 \cdot (X_{Mg,M2}^{Opx}) \cdot (X_{Cr,M1}^{Opx}) \cdot (X_{Al,T}^{Opx}) \cdot (X_{Si,T}^{Opx})$
7	<i>Fe Tschermak's</i>	<i>FeTs</i>	$FeAl_2SiO_6$	$4 \cdot (X_{Fe,M2}^{Opx}) \cdot (X_{Al,M1}^{Opx}) \cdot (X_{Al,T}^{Opx}) \cdot (X_{Si,T}^{Opx})$
8	<i>Fe – Cr Tschermak's</i>	<i>FeCrTs</i>	$FeCrAlSiO_6$	$4 \cdot (X_{Fe,M2}^{Opx}) \cdot (X_{Cr,M1}^{Opx}) \cdot (X_{Al,T}^{Opx}) \cdot (X_{Si,T}^{Opx})$

Table 2: End members for Spinel

n	Name	Abb.	Chem. Formula	Activity
1	<i>Hercynite</i>	<i>Hc</i>	$FeAl_2O_4$	$(X_{Fe}^{Spl}) \cdot (X_{Al}^{Spl})^2$
2	<i>Spinel</i>	<i>Spl</i>	$MgAl_2O_4$	$(X_{Mg}^{Spl}) \cdot (X_{Al}^{Spl})^2$
3	<i>Chromite</i>	<i>Chr</i>	$FeCr_2O_4$	$(X_{Fe}^{Spl}) \cdot (X_{Cr}^{Spl})^2$
4	<i>Magnesiochromite</i>	<i>Mchr</i>	$MgCr_2O_4$	$(X_{Mg}^{Spl}) \cdot (X_{Cr}^{Spl})^2$
5	<i>Magnetite</i>	<i>Mag</i>	$Fe^{2+}Fe_2^{3+}O_4$	$(X_{Fe^{2+}}^{Spl}) \cdot (X_{Fe^{3+}}^{Spl})^2$
6	<i>Magnesioferrite</i>	<i>Mfr</i>	$MgFe_2^{3+}O_4$	$(X_{Mg}^{Spl}) \cdot (X_{Fe^{3+}}^{Spl})^2$
7	<i>Ulvöspinel</i>	<i>Usp</i>	Fe_2TiO_4	$(X_{Fe}^{Spl})^2 \cdot (X_{Ti}^{Spl})$
8	<i>Qandilite</i>	<i>Qnd</i>	Mg_2TiO_4	$(X_{Mg}^{Spl})^2 \cdot (X_{Ti}^{Spl})$

Orthopyroxene's end members are the four classic members Fs, En, Di, Hd (Morimoto 1988) and the Tschermak's components with Fe^{+2} -Mg interaction and Al^{+3} - Cr^{+3} substitution. The end members in spinel are following the modified Johnson spinel prism (Stevens 1944, Ferracutti 2015 et al) with Mg and Fe^{+2} interaction in X site and Substitutions with Al^{+3} , Cr^{+3} , Fe^{+3} , Ti^{+4} in Y site. By having an octal orthopyroxene and spinel the only thing that remains to know is which solution model to use. Both solution methods have been used to find the parameters, both symmetric and asymmetric. The end result is that both systems produce

similar results with the asymmetric having a smaller standard deviation of 2-5^oC, which is a relatively small difference knowing that the asymmetric model has much greater complexity in its parameterization. So to create the equation for the activity coefficient, the procedure is as follows:

$$RT\ln(K_\gamma) = RT\ln\left(\frac{\gamma_{FeAl_2O_4}^{Spl} \cdot \gamma_{Mg_2Si_2O_6}^{Opx}}{\gamma_{MgAl_2O_4}^{Spl} \cdot \gamma_{Fe_2Si_2O_6}^{Opx}}\right) \quad (32)$$

$$RT\ln(K_\gamma) = RT\ln(\gamma_{FeAl_2O_4}^{Spl}) + RT\ln(\gamma_{Mg_2Si_2O_6}^{Opx}) - RT\ln(\gamma_{MgAl_2O_4}^{Spl}) - RT\ln(\gamma_{Fe_2Si_2O_6}^{Opx}) \quad (33)$$

by using equation (12) for symmetrical solutions

For octal Orthopyroxene with 1:F_s and 2:En activity coefficients:

$$RT\ln(\gamma_1) = W_{12}X_2 + W_{13}X_3 + W_{14}X_4 + W_{15}X_5 + W_{16}X_6 + W_{17}X_7 + W_{18}X_8 - G^{XS} \quad (34)$$

$$RT\ln(\gamma_2) = W_{21}X_1 + W_{23}X_3 + W_{24}X_4 + W_{25}X_5 + W_{26}X_6 + W_{27}X_7 + W_{28}X_8 - G^{XS} \quad (35)$$

$$RT\ln(\gamma_{Fs}) = W_{FsEn}X_{En} + W_{FsDi}X_{Di} + W_{FsHd}X_{Hd} + W_{FsMgTs}X_{MgTs} + W_{FsMgCrTs}X_{MgCrTs} + W_{FsFeTs}X_{FeTs} + W_{FsFeCrTs}X_{FeCrTs} - G^{XS} \quad (36)$$

$$RT\ln(\gamma_{En}) = W_{EnFs}X_{Fs} + W_{EnDi}X_{Di} + W_{EnHd}X_{Hd} + W_{EnMgTs}X_{MgTs} + W_{EnMgCrTs}X_{MgCrTs} + W_{EnFeTs}X_{FeTs} + W_{EnFeCrTs}X_{FeCrTs} - G^{XS} \quad (37)$$

For octal Spinel with 1:Hc and 2:Spl activity coefficients:

$$RT\ln(\gamma_1) = W_{12}X_2 + W_{13}X_3 + W_{14}X_4 + W_{15}X_5 + W_{16}X_6 + W_{17}X_7 + W_{18}X_8 - G^{XS} \quad (38)$$

$$RT\ln(\gamma_2) = W_{21}X_1 + W_{23}X_3 + W_{24}X_4 + W_{25}X_5 + W_{26}X_6 + W_{27}X_7 + W_{28}X_8 - G^{XS} \quad (39)$$

$$RT\ln(\gamma_{Hc}) = W_{HcSpl}X_{Spl} + W_{HcChr}X_{Chr} + W_{HcMchr}X_{Mchr} + W_{HcMag}X_{Mag} + W_{HcMfr}X_{Mfr} + W_{HcUsp}X_{Usp} + W_{HcQnd}X_{Qnd} - G^{XS} \quad (40)$$

$$RT\ln(\gamma_{Spl}) = W_{SplHc}X_{Hc} + W_{SplChr}X_{Chr} + W_{SplMchr}X_{Mchr} + W_{SplMag}X_{Mag} + W_{SplMfr}X_{Mfr} + W_{SplUsp}X_{Usp} + W_{SplQnd}X_{Qnd} - G^{XS} \quad (41)$$

Adding (35), (36), (39), (40) to (32)

$$RT\ln(K_\gamma) = W_{HcSpl}X_{Spl} + W_{HcChr}X_{Chr} + W_{HcMchr}X_{Mchr} + W_{HcMag}X_{Mag} + W_{HcMfr}X_{Mfr} + W_{HcUsp}X_{Usp} + W_{HcQnd}X_{Qnd} - G^{XS} + W_{EnFs}X_{Fs} + W_{EnDi}X_{Di} + W_{EnHd}X_{Hd} + W_{EnMgTs}X_{MgTs} + W_{EnMgCrTs}X_{MgCrTs} + W_{EnFeTs}X_{FeTs} + W_{EnFeCrTs}X_{FeCrTs} - G^{XS} - W_{SplHc}X_{Hc} - W_{SplChr}X_{Chr} - W_{SplMchr}X_{Mchr} - W_{SplMag}X_{Mag} - W_{SplMfr}X_{Mfr} - W_{SplUsp}X_{Usp} - W_{SplQnd}X_{Qnd} + G^{XS} - W_{FsEn}X_{En} - W_{FsDi}X_{Di} - W_{FsHd}X_{Hd} - W_{FsMgTs}X_{MgTs} - W_{FsMgCrTs}X_{MgCrTs} - W_{FsFeTs}X_{FeTs} - W_{FsFeCrTs}X_{FeCrTs} + G^{XS}$$

$$RT\ln(K_\gamma) = W_{HcSpl}X_{Spl} - W_{SplHc}X_{Hc} + W_{HcChr}X_{Chr} - W_{SplChr}X_{Chr} + W_{HcMchr}X_{Mchr} - W_{SplMchr}X_{Mchr} + W_{HcMag}X_{Mag} - W_{SplMag}X_{Mag} + W_{HcMfr}X_{Mfr} - W_{SplMfr}X_{Mfr} + W_{HcUsp}X_{Usp} - W_{SplUsp}X_{Usp} + W_{HcQnd}X_{Qnd} - W_{SplQnd}X_{Qnd} + W_{EnFs}X_{Fs} - W_{FsEn}X_{En} + W_{EnDi}X_{Di} - W_{FsDi}X_{Di} + W_{EnHd}X_{Hd} - W_{FsHd}X_{Hd} + W_{EnMgTs}X_{MgTs} - W_{FsMgTs}X_{MgTs} + W_{EnMgCrTs}X_{MgCrTs} - W_{FsMgCrTs}X_{MgCrTs} + W_{EnFeTs}X_{FeTs} - W_{FsFeTs}X_{FeTs} + W_{EnFeCrTs}X_{FeCrTs} - W_{FsFeCrTs}X_{FeCrTs} - G^{XS} + G^{XS} - G^{XS} + G^{XS} \xrightarrow{W_{ij}=W_{ji} \text{ (13)}} \quad (42)$$

$$\begin{aligned}
RT\ln(K_\gamma) = & (X_{Spl} - X_{Hc})W_{HcSpl} + X_{Mchr}(W_{HcMchr} - W_{SplMchr}) + X_{Mag}(W_{HcMag} - W_{SplMag}) \\
& + X_{Mfr}(W_{HcMfr} - W_{SplMfr}) + X_{Usp}(W_{HcUsp} - W_{SplUsp}) + X_{Qnd}(W_{HcQnd} \\
& - W_{SplQnd}) + (X_{Fs} - X_{En})W_{EnFs} + X_{Di}(W_{EnDi} - W_{FsDi}) + X_{Hd}(W_{EnHd} - W_{FsHd}) \\
& + X_{MgTs}(W_{EnMgTs} - W_{FsMgTs}) + X_{MgCrTs}(W_{EnMgCrTs} - W_{FsMgCrTs}) \\
& + X_{FeTs}(W_{EnFeTs} - W_{FsFeTs}) + X_{FeCrTs}(W_{EnFeCrTs} - W_{FsFeCrTs}) \quad (43)
\end{aligned}$$

2.6. T_{KG21}: A new Opx/Sp Geothermometer

The Arrhenius equation will not be used to create the thermometric equation. Instead, a different approach will be implemented, starting from equation (5):

$$\begin{aligned}
\Delta G + (RT \ln(K_\gamma * K_D)) &= 0 \stackrel{(6)}{\Rightarrow} \\
\Delta H + P * \Delta V - T * \Delta S + RT \ln(K_D) + RT \ln(K_\gamma) &= 0 \quad (44) \\
T(\Delta S - R \ln(K_D)) &= \Delta H + P * \Delta V + RT \ln(K_\gamma) \quad (45)
\end{aligned}$$

In this equation temperature, pressure and the molar fraction of end members are known. On the contrary enthalpy, volume, entropy and Margules are unknown thermodynamic parameters. In order to be able to solve the equation and calibrate the unknown parameters, calculating the entropy of the system is needed. For this purpose, the thermodynamic properties (Robie & Hemingway 1995, p.21&34) of the mineral phases that take part in the thermometric equilibrium will be used to calculate its entropy.

$$\begin{aligned}
\text{Hercynite: } S_{Hc}^0 &= 117.0 \pm 3 \text{ (Jmol}^{-1}\text{K}^{-1}\text{)} \\
\text{Spinel: } S_{Spl}^0 &= 88.7 \pm 4 \text{ (Jmol}^{-1}\text{K}^{-1}\text{)} \\
\text{Ferrosilite: } S_{Fs}^0 &= 94.6 \pm 0.3 \text{ (Jmol}^{-1}\text{K}^{-1}\text{)} \\
\text{Enstatite: } S_{En}^0 &= 66.3 \pm 0.1 \text{ (Jmol}^{-1}\text{K}^{-1}\text{)}
\end{aligned}$$

$$\begin{aligned}
\Delta S_{Opx/Sp}^0 \text{ (Jmol}^{-1}\text{K}^{-1}\text{)} &= (S_{Hc}^0 + S_{En}^0)_{Products} - (S_{Spl}^0 + S_{Fs}^0)_{Reactants} \Rightarrow \\
\Delta S_{Opx/Sp}^0 \text{ (Jmol}^{-1}\text{K}^{-1}\text{)} &= (117 + 66.3)_{Products} - (88.7 + 94.6)_{Reactants} \Rightarrow \\
\Delta S_{Opx/Sp}^0 \text{ (Jmol}^{-1}\text{K}^{-1}\text{)} &= (183.3)_{Products} - (183.3)_{Reactants} \Rightarrow \\
\Delta S_{Opx/Sp}^0 \text{ (Jmol}^{-1}\text{K}^{-1}\text{)} &= 0 \quad (46)
\end{aligned}$$

As a result, the entropy of the equilibrium equals to 0. It has also been checked that there are no Margule parameters that have different properties in terms of entropy. Hence entropy is neglected for this thermometric expression and the form is the following:

$$\begin{aligned}
T(-R \ln(K_D)) = & \Delta H + P * \Delta V + (X_{Spl} - X_{Hc})W_{HcSpl} + X_{Mchr}(W_{HcMchr} - W_{SplMchr}) + X_{Mag}(W_{HcMag} \\
& - W_{SplMag}) + X_{Mfr}(W_{HcMfr} - W_{SplMfr}) + X_{Usp}(W_{HcUsp} - W_{SplUsp}) + X_{Qnd}(W_{HcQnd} \\
& - W_{SplQnd}) + (X_{Fs} - X_{En})W_{EnFs} + X_{Di}(W_{EnDi} - W_{FsDi}) + X_{Hd}(W_{EnHd} - W_{FsHd}) \\
& + X_{MgTs}(W_{EnMgTs} - W_{FsMgTs}) + X_{MgCrTs}(W_{EnMgCrTs} - W_{FsMgCrTs}) \\
& + X_{FeTs}(W_{EnFeTs} - W_{FsFeTs}) + X_{FeCrTs}(W_{EnFeCrTs} - W_{FsFeCrTs}) \quad (47)
\end{aligned}$$

By having this formulation, the equation is solvable so that linear regression can take place. After the linear regression and the fixation of the thermometric equation, there are some experimental pairs that have different types of analytical errors. For instance, different temperatures inside the capsule or a different temperature than the one listed or Opx/Sp pairs which may not be in thermodynamic equilibrium. These samples have a large difference between calculated and experimental temperature, and thus the creation of a robust geothermometer demands that some of the experimental data be eliminated. The process of excluding samples is the elimination of the maximum relative deviation ($(T_{\text{exp}} - T_{\text{calc}})/T_{\text{exp}}$) one by one. From 1188 experimental samples, 164 have been eliminated or the 13.8% of them, giving an overall standard deviation of 219°C, where the different expressions of Liermann's and Ganguly's geothermometers (Liermann & Ganguly 2003, Table 4) have standard deviations of 243-447°C. Here is important to mention that within $\pm 200^\circ\text{C}$ is the 67.38% of the samples with a standard deviation of $\pm 101^\circ\text{C}$. The final thermometric equation is the following:

$$T_{KG21}(\text{°K}) = \frac{4930.98 + 205.58 * P(\text{Kbar}) + RT \ln(K_\gamma)}{R * \ln(K_D)} \quad (48)$$

$$\text{With } \ln(K_D) = \ln \left(\frac{\left(\frac{Fe^{2+}}{Mg} \right)_{Sp}^2}{\left(\frac{Fe_{M2}^{2+} \cdot Fe_{M1}^{2+}}{Mg_{M2} \cdot Mg_{M1}} \right)_{Opx}} \right) \quad (49)$$

$$\begin{aligned} RT \ln(K_\gamma) = & 33678.88(X_{Hc} - X_{Spl}) + 25630.65 * X_{Chr} - 6195.58 * X_{Mchr} + 47258.56 * X_{Mag} \\ & - 27969.63 * X_{Mfr} + 105130.74 * X_{Usp} - 93914.69 * X_{Qnd} + 30410.81 * (X_{En} - X_{Fs}) \\ & + 98894.14 * X_{Di} - 381529.99 * X_{Hd} + 12886.55 * X_{MgTs} + 180750.91 * X_{MgCrTs} \\ & - 175575.25 * X_{FeTs} - 634363.98 * X_{FeCrTs} \quad (50) \\ \text{Gas Constant : } R(\text{Jmol}^{-1}\text{K}^{-1}) = & 8.3144598 \end{aligned}$$

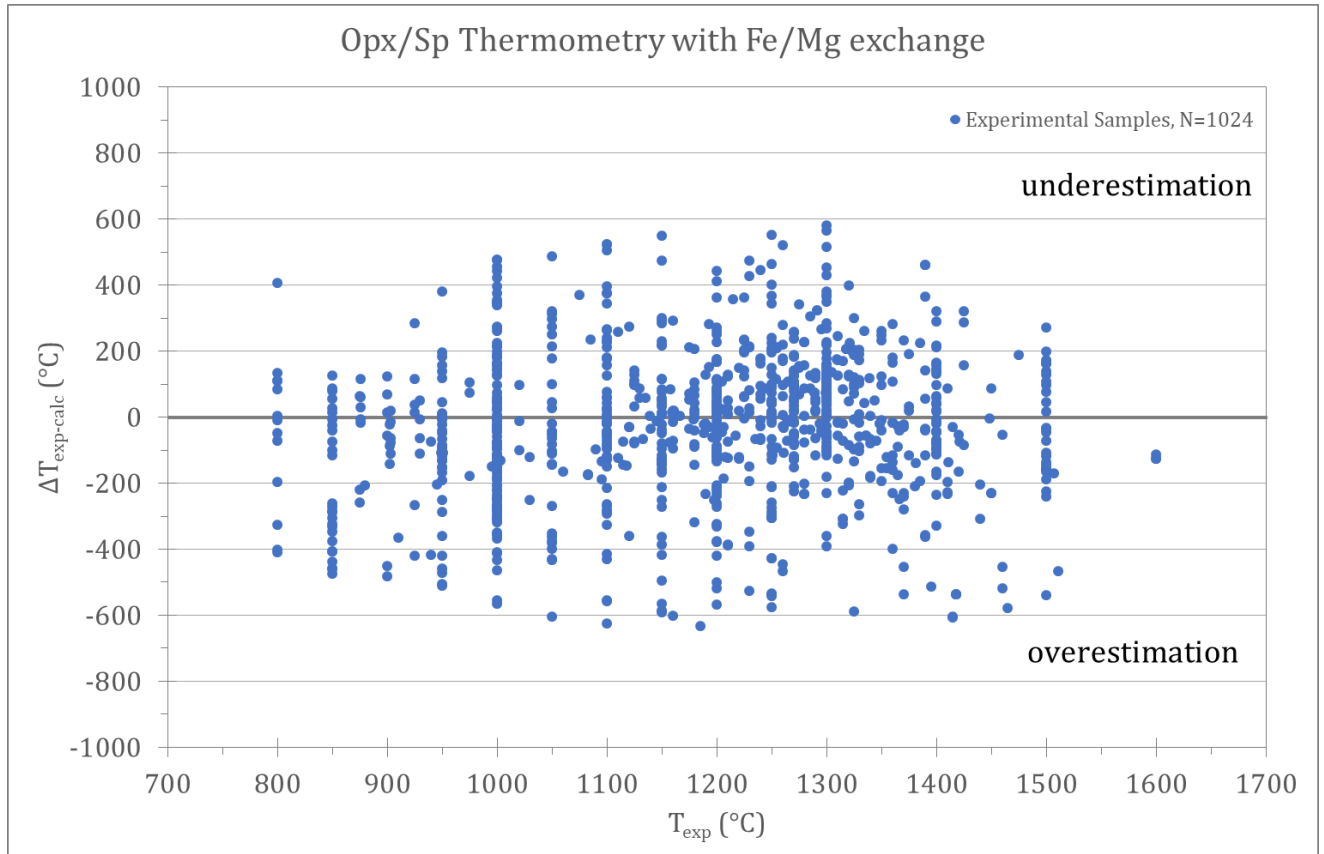


Figure17: $\Delta T_{\text{Exp-Calc}}$ vs T_{Exp} final experimental results of the T_{KG21} .

Charts were created with $\Delta T_{Exp-Calc}$ to check how well the parameters were determined in T_{KG21} :

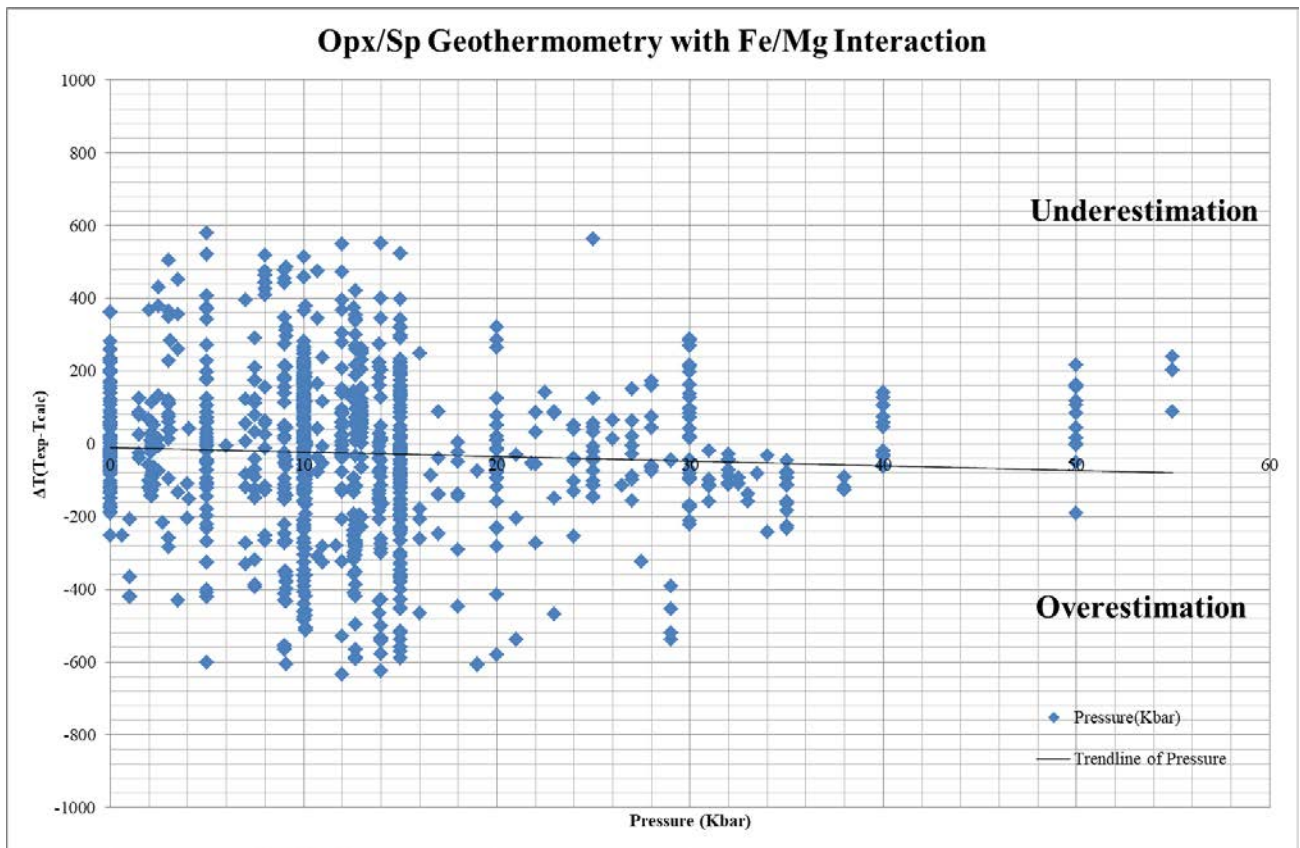


Figure 18: Chart with $\Delta T_{Exp-Calc}$ vs Pressure (Kbar) to show the robustness of the Thermometer.

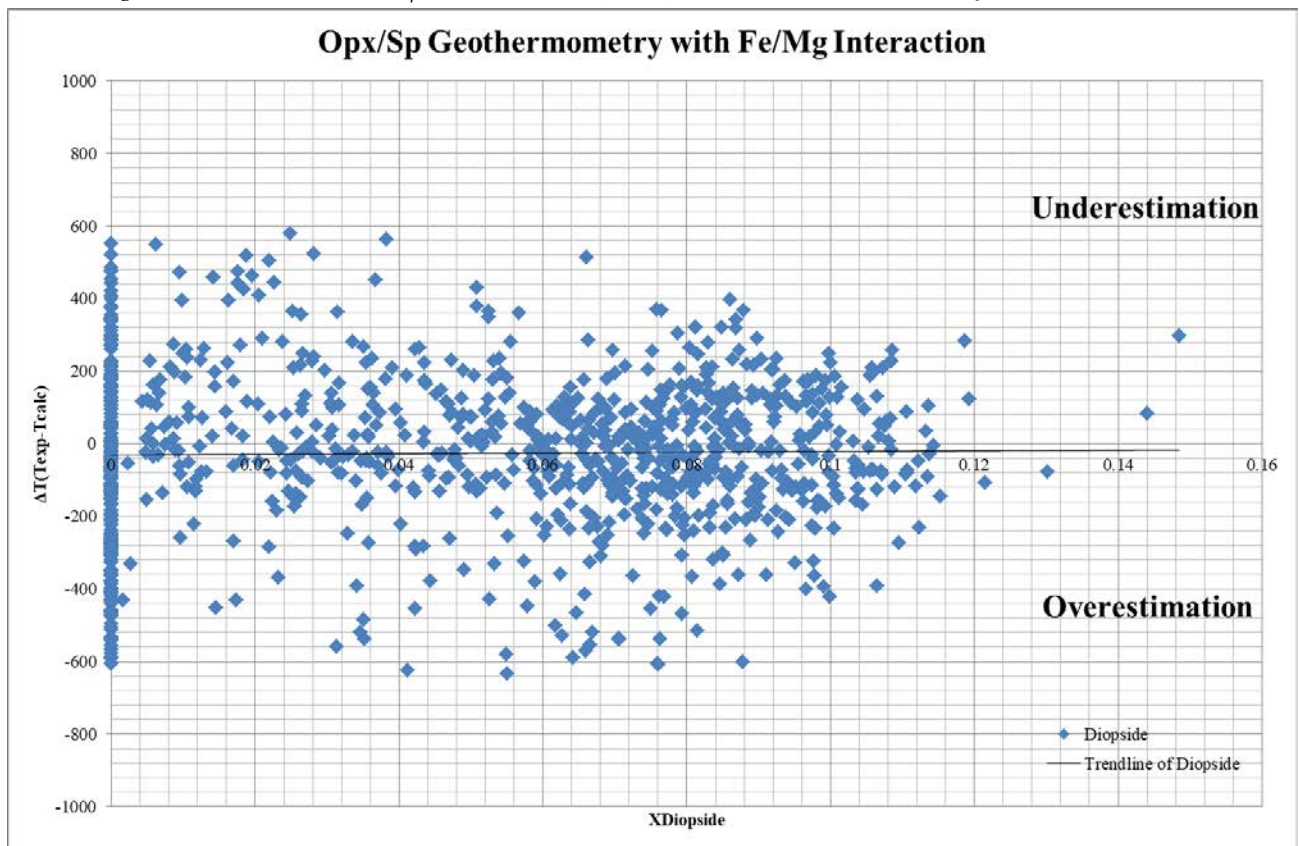


Figure 19: Chart with $\Delta T_{Exp-Calc}$ vs X_{Di} to show the robustness of the Thermometer.

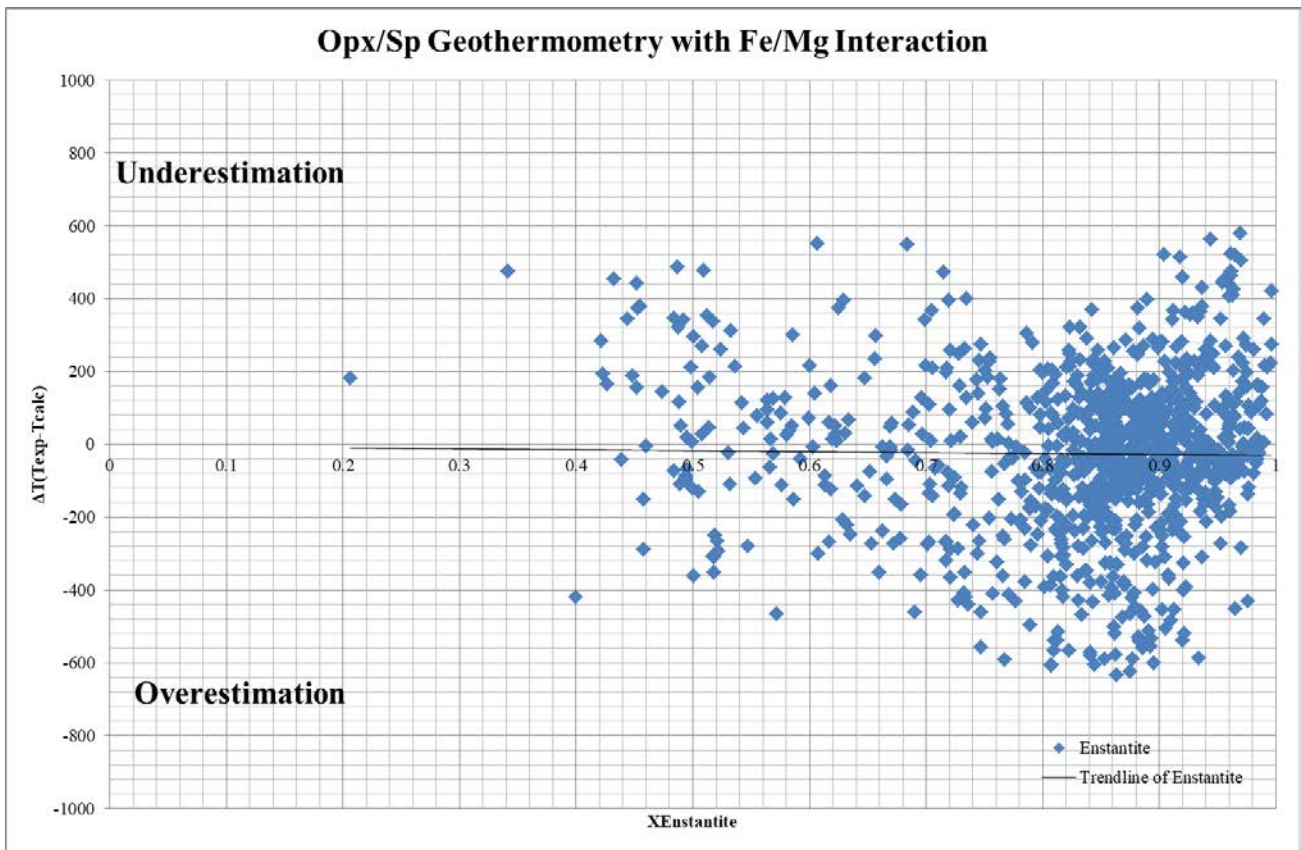


Figure 20: Chart with $\Delta T_{Exp-Calc}$ vs X_{En} to show the robustness of the Thermometer.

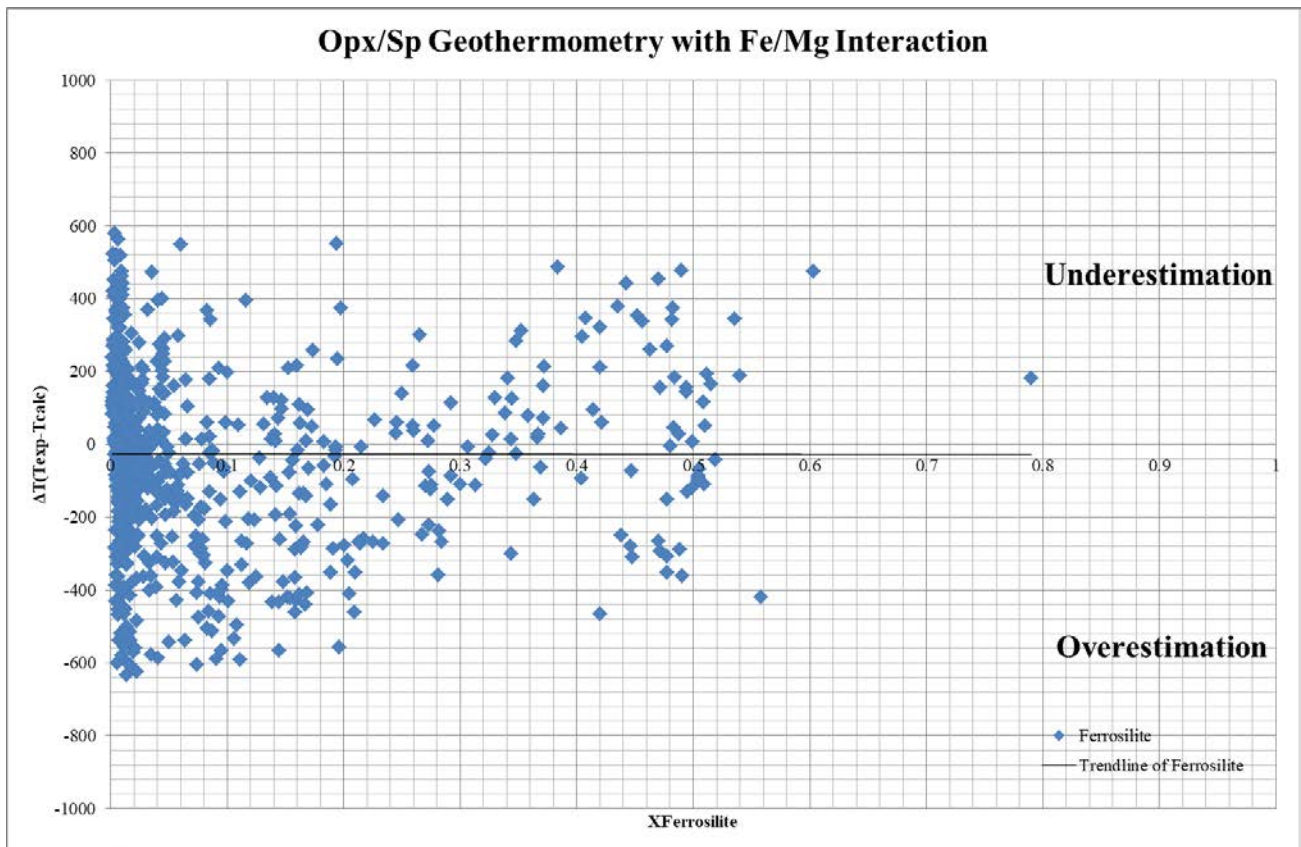


Figure 21: Chart with $\Delta T_{Exp-Calc}$ vs X_{Fs} to show the robustness of the Thermometer.

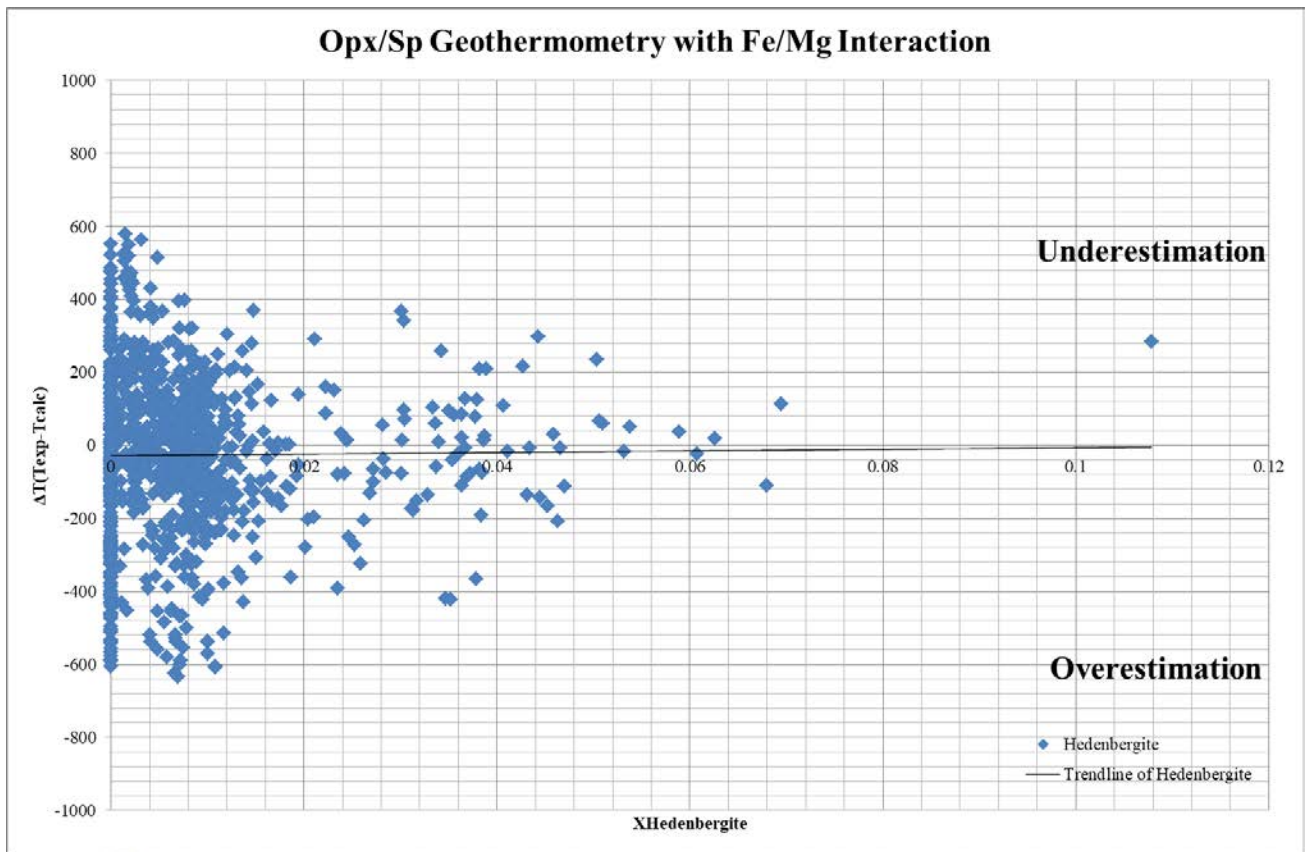


Figure 22: Chart with $\Delta T_{Exp-Calc}$ vs X_{Hd} to show the robustness of the Thermometer.

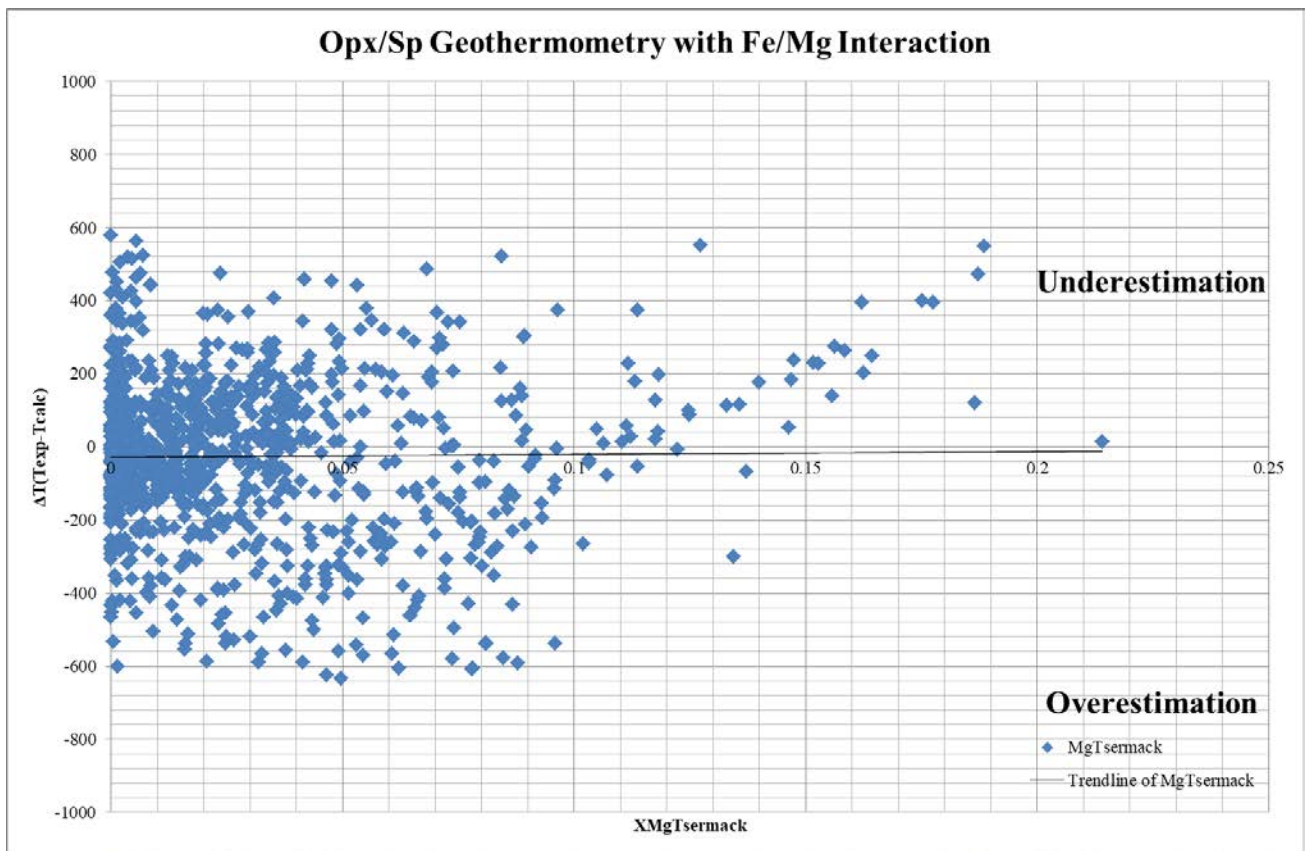


Figure 23: Chart with $\Delta T_{Exp-Calc}$ vs X_{MgTs} to show the robustness of the Thermometer.

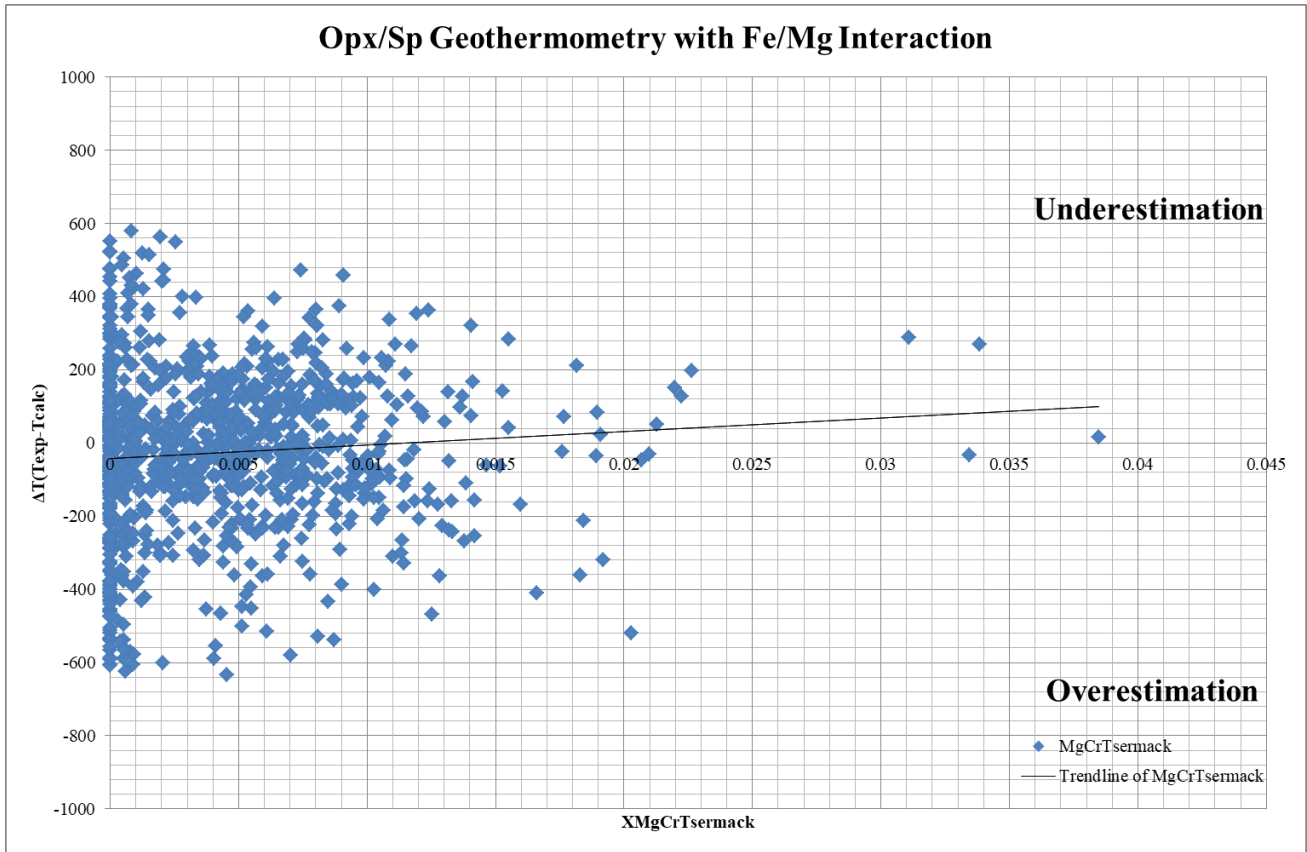


Figure 24: Chart with $\Delta T_{Exp-Calc}$ vs X_{MgCrTs} to show the robustness of the Thermometer.

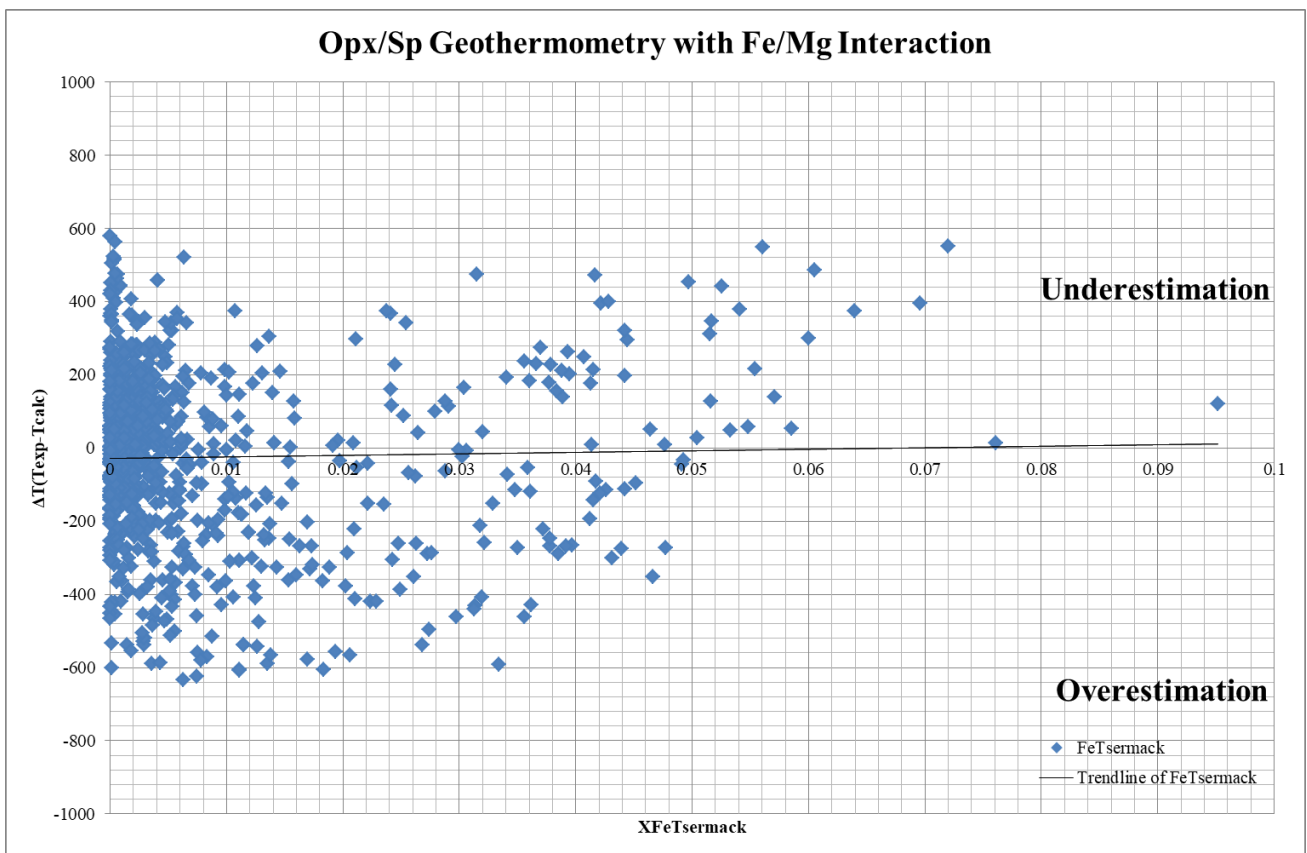


Figure 25: Chart with $\Delta T_{Exp-Calc}$ vs X_{FeTs} to show the robustness of the Thermometer.

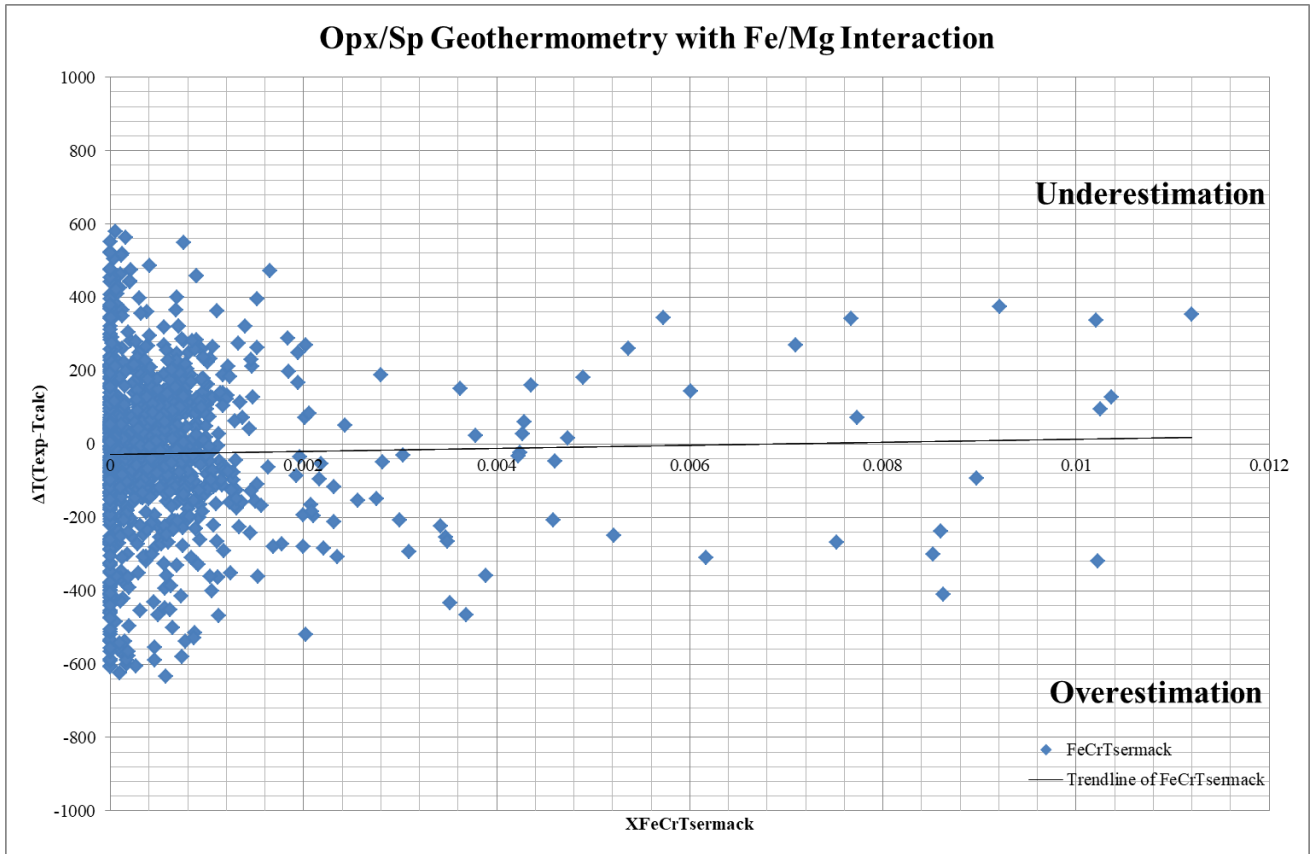


Figure 26: Chart with $\Delta T_{Exp-Calc}$ vs X_{FeCrTs} to show the robustness of the Thermometer.

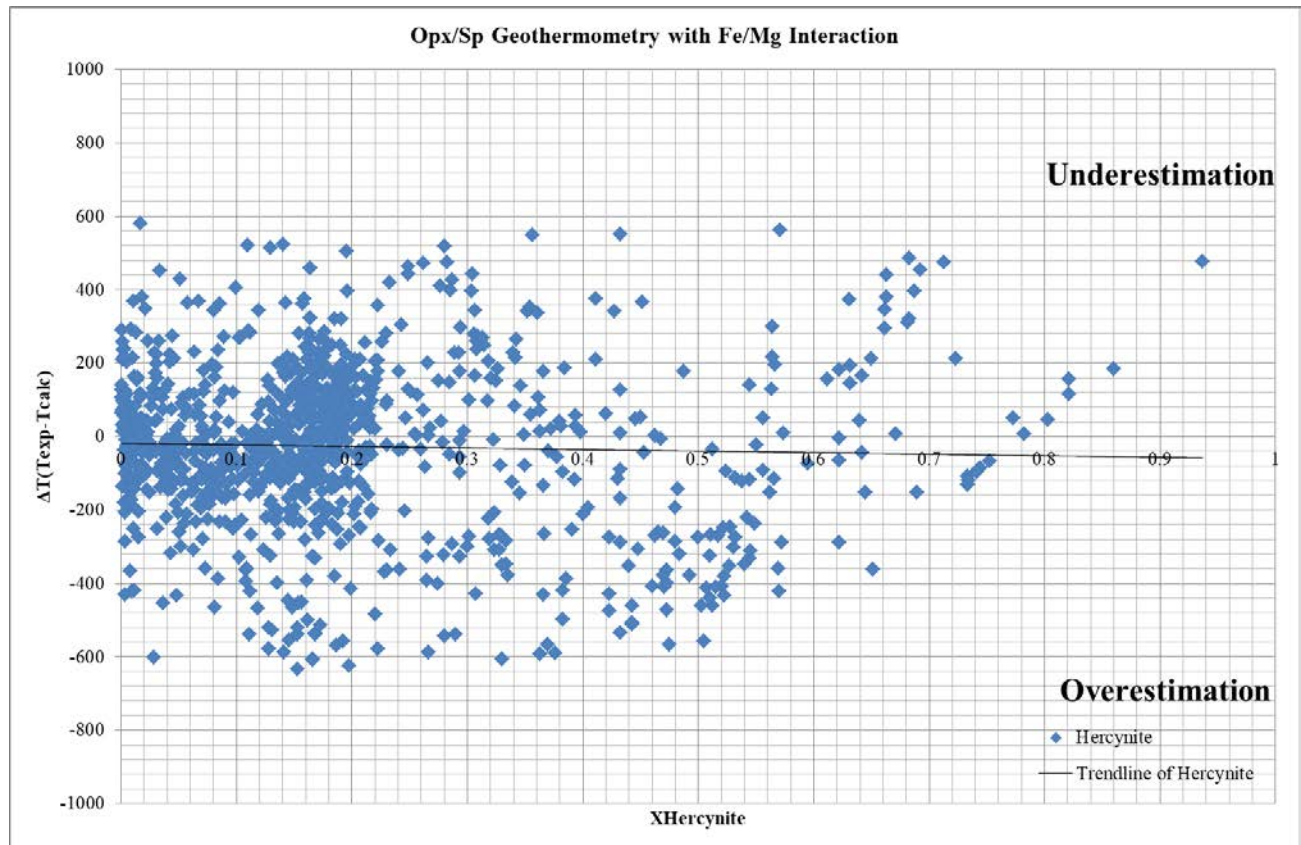


Figure 27: Chart with $\Delta T_{Exp-Calc}$ vs X_{Hc} to show the robustness of the Thermometer.

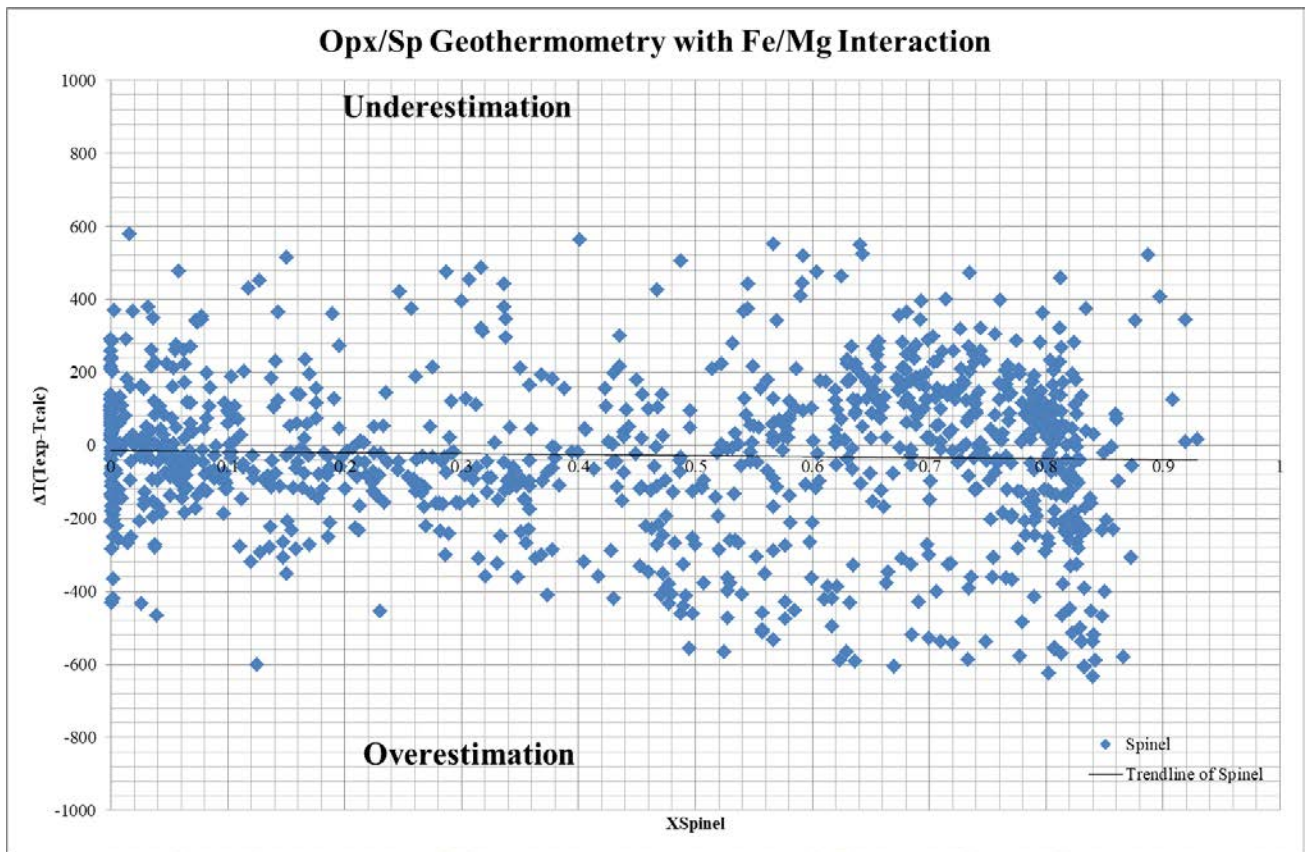


Figure 28: Chart with $\Delta T_{Exp-Calc}$ vs X_{Spl} to show the robustness of the Thermometer.

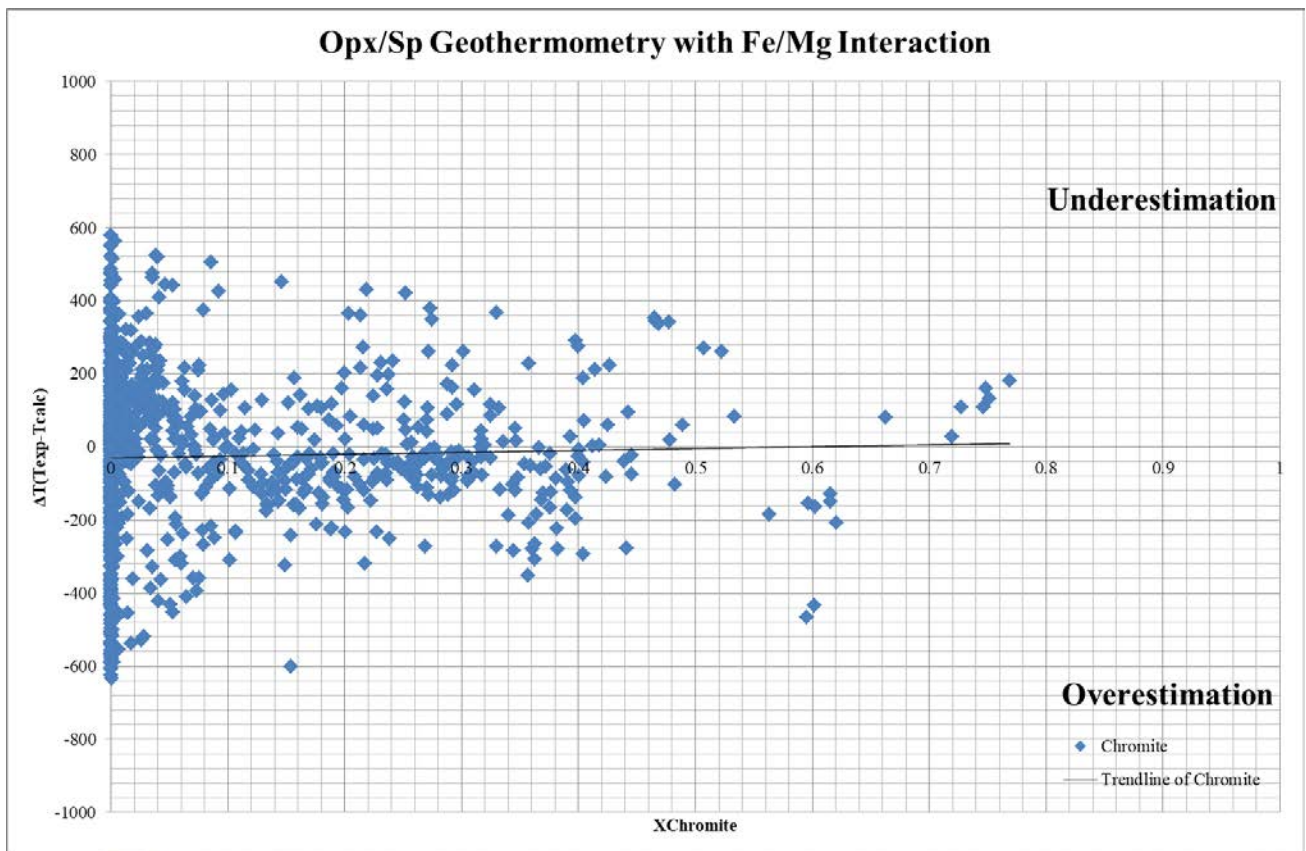


Figure 29: Chart with $\Delta T_{Exp-Calc}$ vs X_{Chr} to show the robustness of the Thermometer.

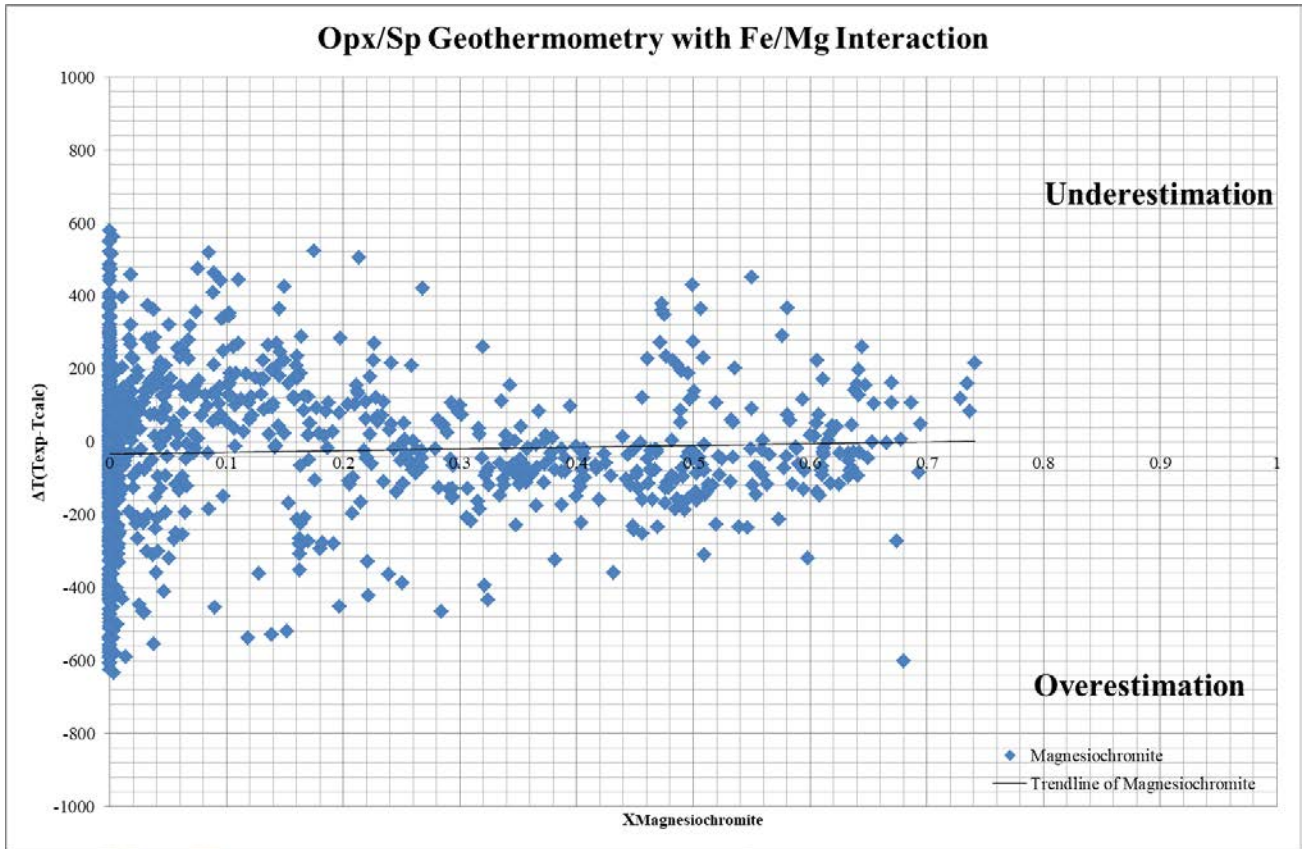


Figure 30: Chart with $\Delta T_{Exp-Calc}$ vs X_{Mchr} to show the robustness of the Thermometer.

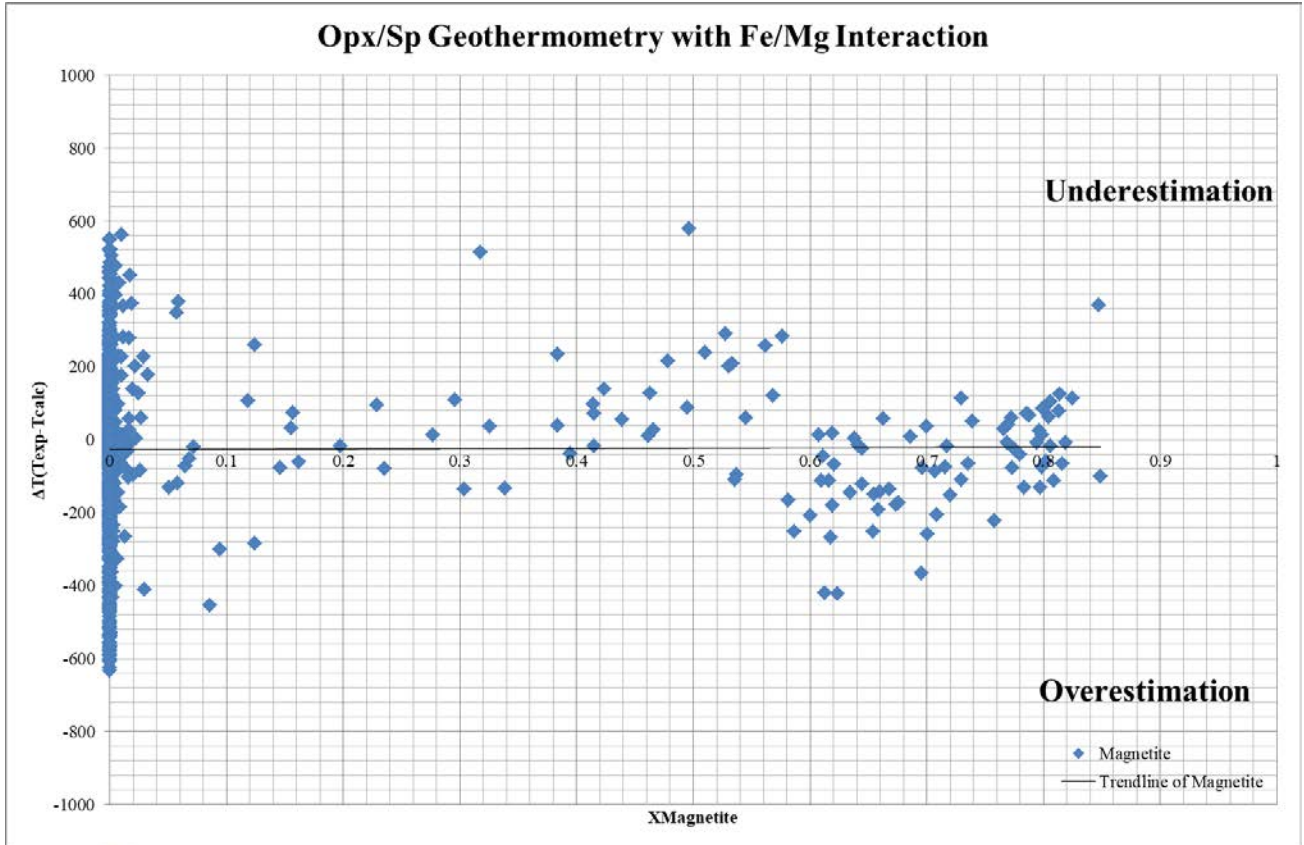


Figure 31: Chart with $\Delta T_{Exp-Calc}$ vs X_{Mag} to show the robustness of the Thermometer.

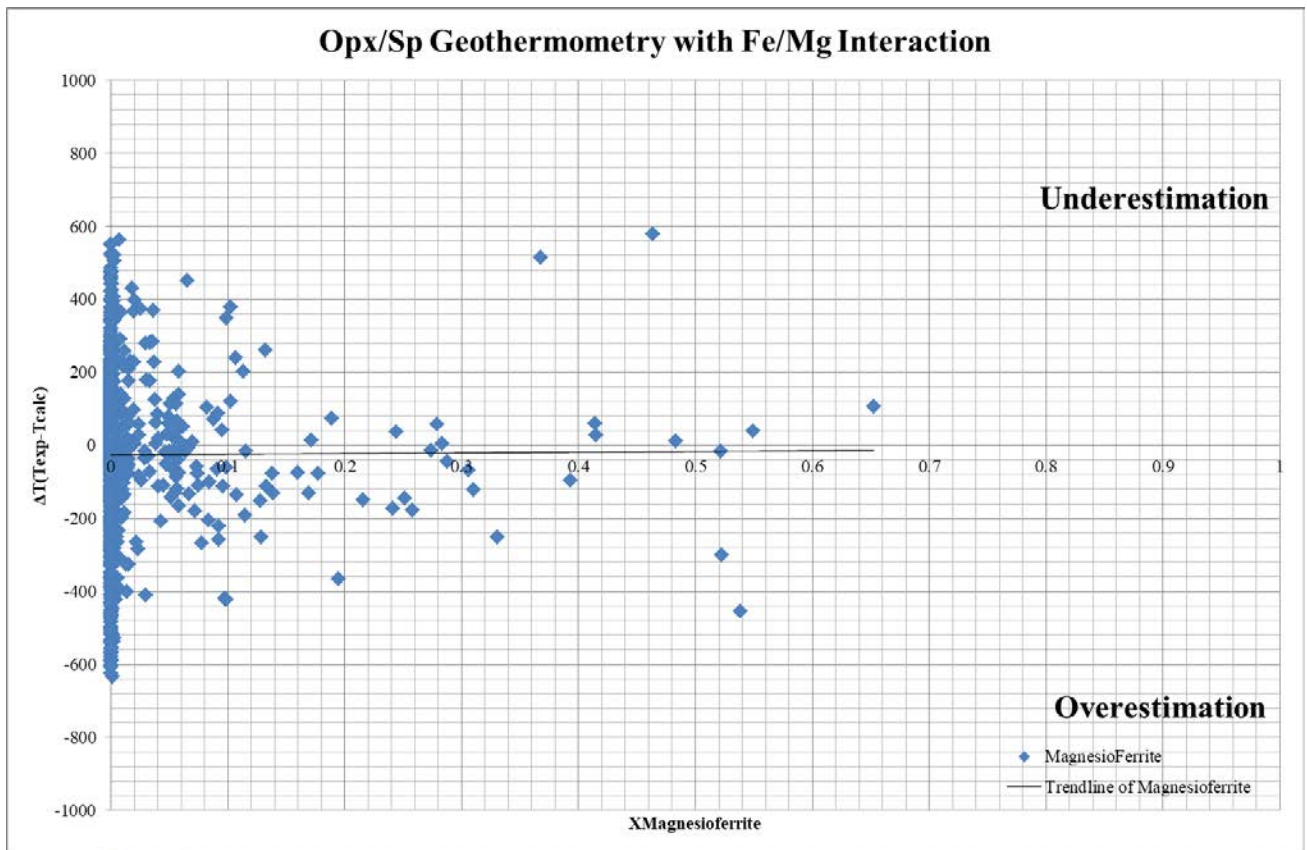


Figure 32: Chart with $\Delta T_{Exp-Calc}$ vs X_{Mfr} to show the robustness of the Thermometer.

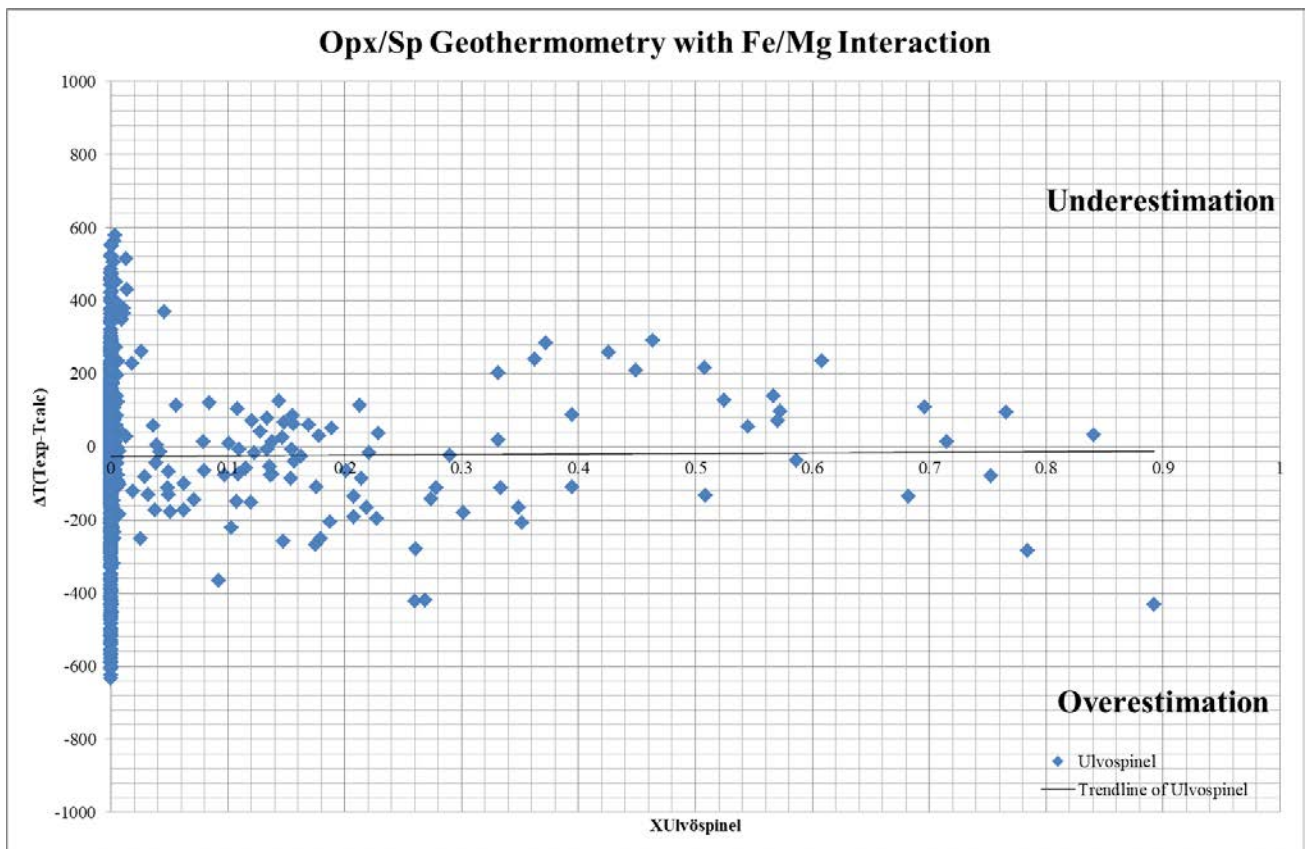


Figure 33: Chart with $\Delta T_{Exp-Calc}$ vs X_{Usp} to show the robustness of the Thermometer.

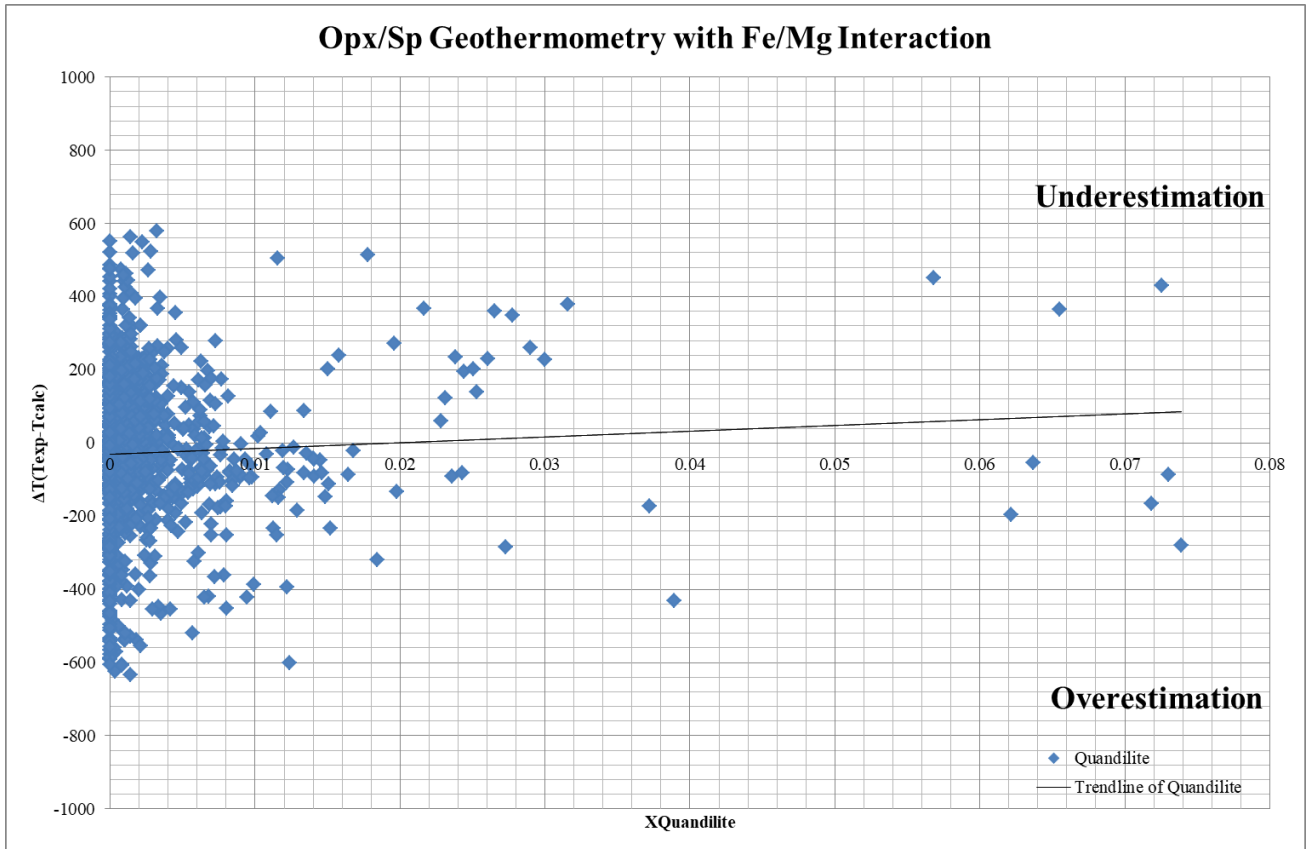


Figure 34: Chart with $\Delta T_{Exp-Calc}$ vs X_{Qnd} to show the robustness of the Thermometer.

From the charts 18-34 it appears that X_{Di} , X_{En} , X_{Hd} , X_{Fs} , X_{MgTs} , X_{FeTs} , X_{FeCrTs} , X_{Hc} , X_{Sp} , X_{Chr} , X_{Mchr} , X_{Mag} , X_{Mfr} and X_{Usp} have a deviation from 5°C to 25°C across their ranges. However in relation to Pressure it is shown that there is a deviation from 1atm with -2°C and in 55Kbar is -80°C, this indicates that there is a gradual overestimation as pressure increases. Other parameters with relatively large deviations are X_{MgCrTs} and X_{Qnd} . In X_{MgCrTs} it is shown that near 0 values have a -18°C deviation and escalate to +90°C in 0.039, but within the bulk of the samples which are in range 0-0.015 the deviation is -18°C to +5°C. Similarly in the molar fraction of Quandilite, there is a deviation where it starts from $X_{Qnd}=0$ with -15°C and increases to $X_{Qnd}=0.074$ with +80°C, whereas in the bulk of the samples which is in range 0-0.02 the deviation is -18°C to 0°C. Therefore, all the parameters have a good calibration with a variation in deviation between 5-35°C across their ranges or in the bulk of the samples, with pressure having a gradual overestimation as increases.

Nevertheless, there are some features in the database that need to be mentioned. Like, that the chemical content is inhomogeneous across the temperature range. As shown in the charts below, it can be seen that between 800 and 1000 °C there is the presence of Aluminum, trivalent iron and titanium, whereas the presence of Chromium is not sufficient. As a result, the geothermometer is biased at these temperatures and in case there is a natural sample that has been created by temperatures in this range, then the result will be coordinated by the calibration that exists at other temperatures. However, the database consists of all the available experimental data, where no samples containing chromite in the spinel have been found in these temperature ranges. So in order for the T_{KG21} to be improved in the future, experimental data in this temperature spectrum are required.

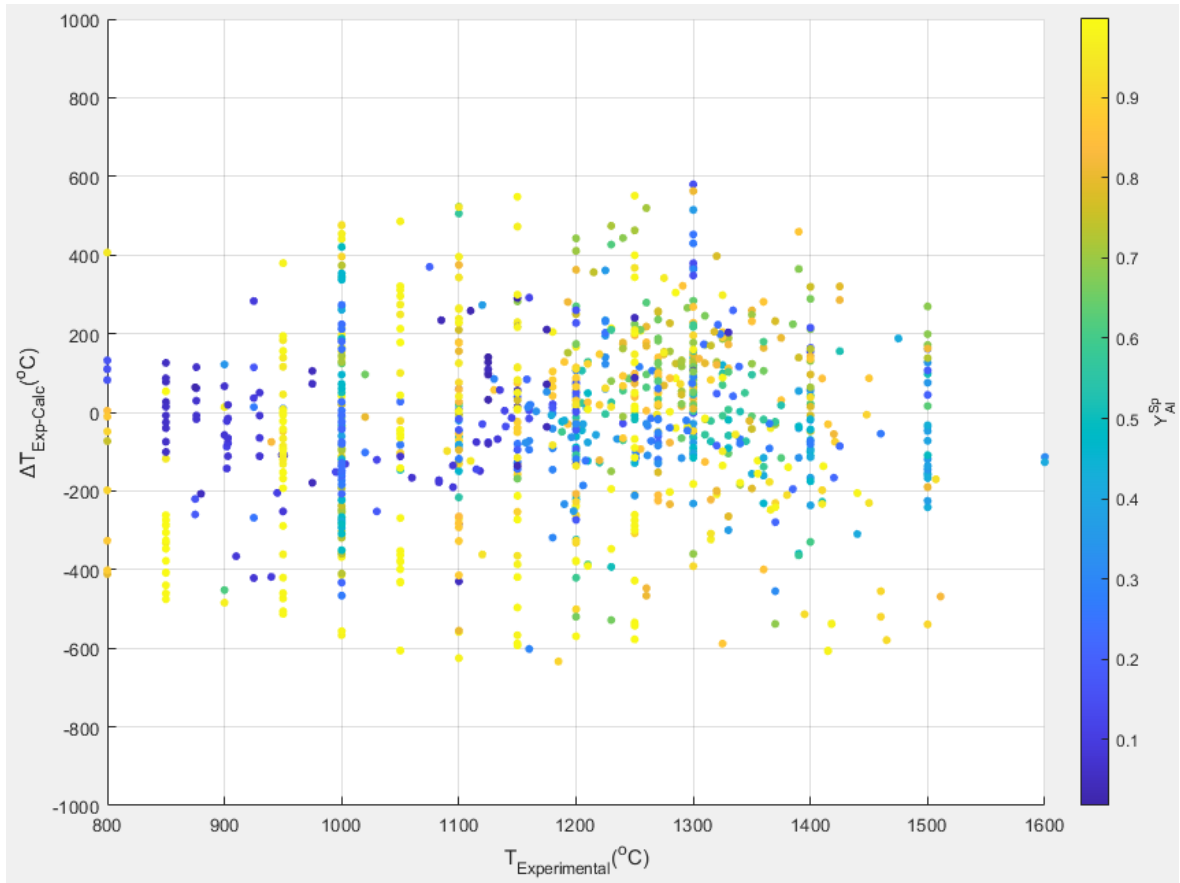


Figure 35: Chart with $\Delta T_{Exp-Calc}$ vs T_{Exp} in relation with Al^{3+} in Y site of Spinel.

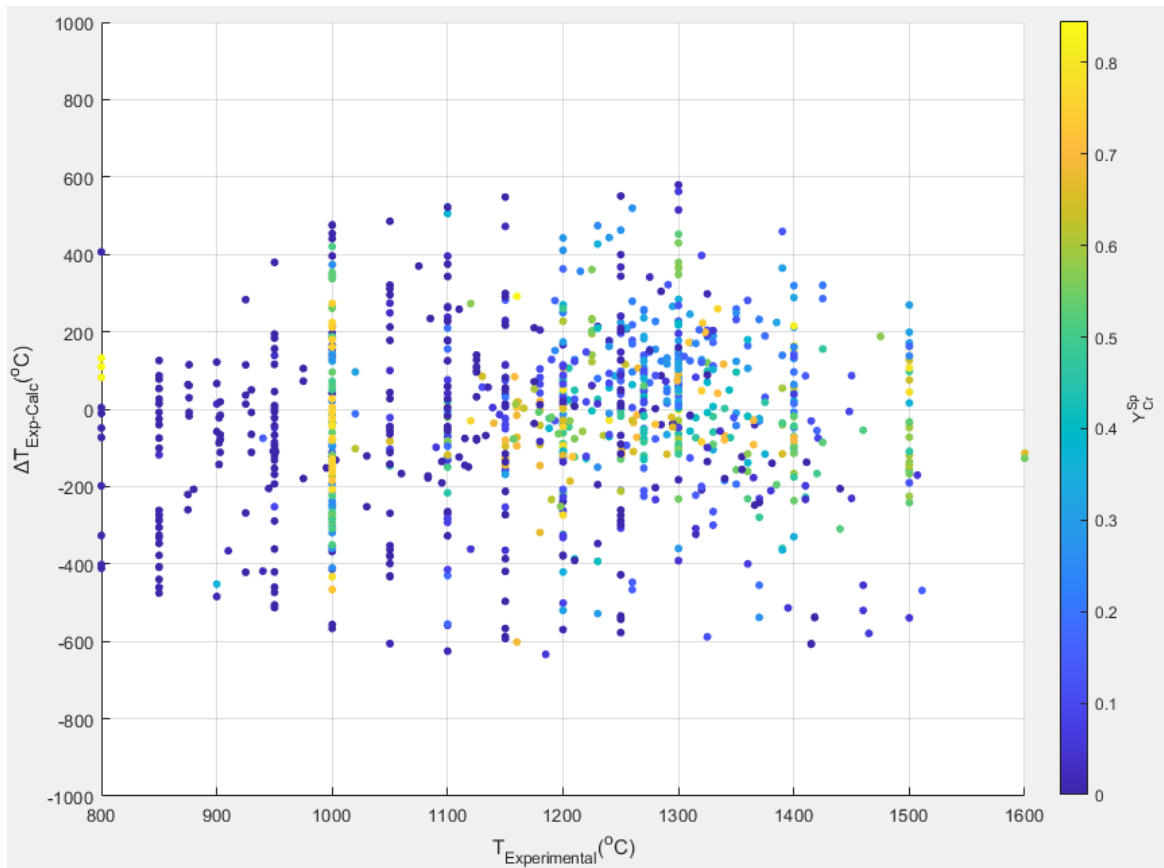


Figure 36: Chart with $\Delta T_{Exp-Calc}$ vs T_{Exp} in relation with Cr^{3+} in Y site of Spinel.

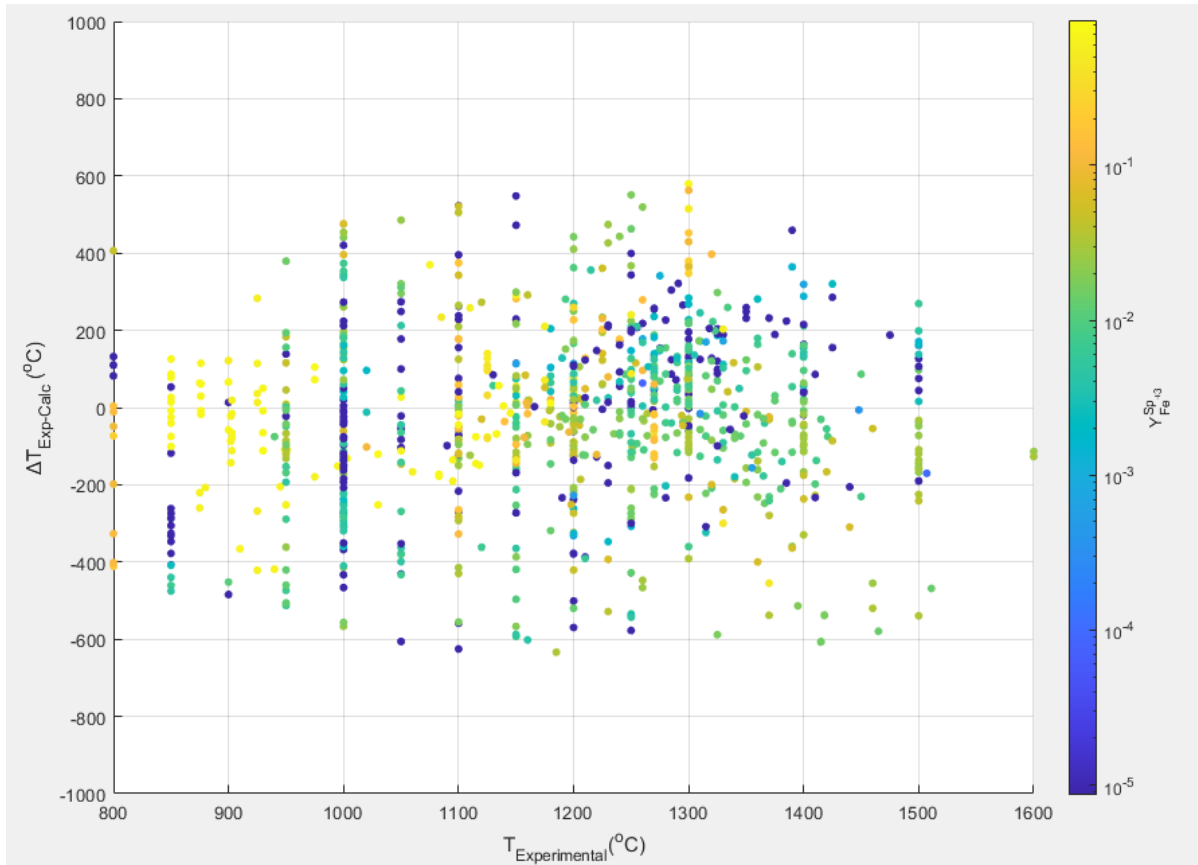


Figure 37: Chart with $\Delta T_{Exp-Calc}$ vs T_{Exp} in relation with Fe^{3+} in Y site of Spinel.

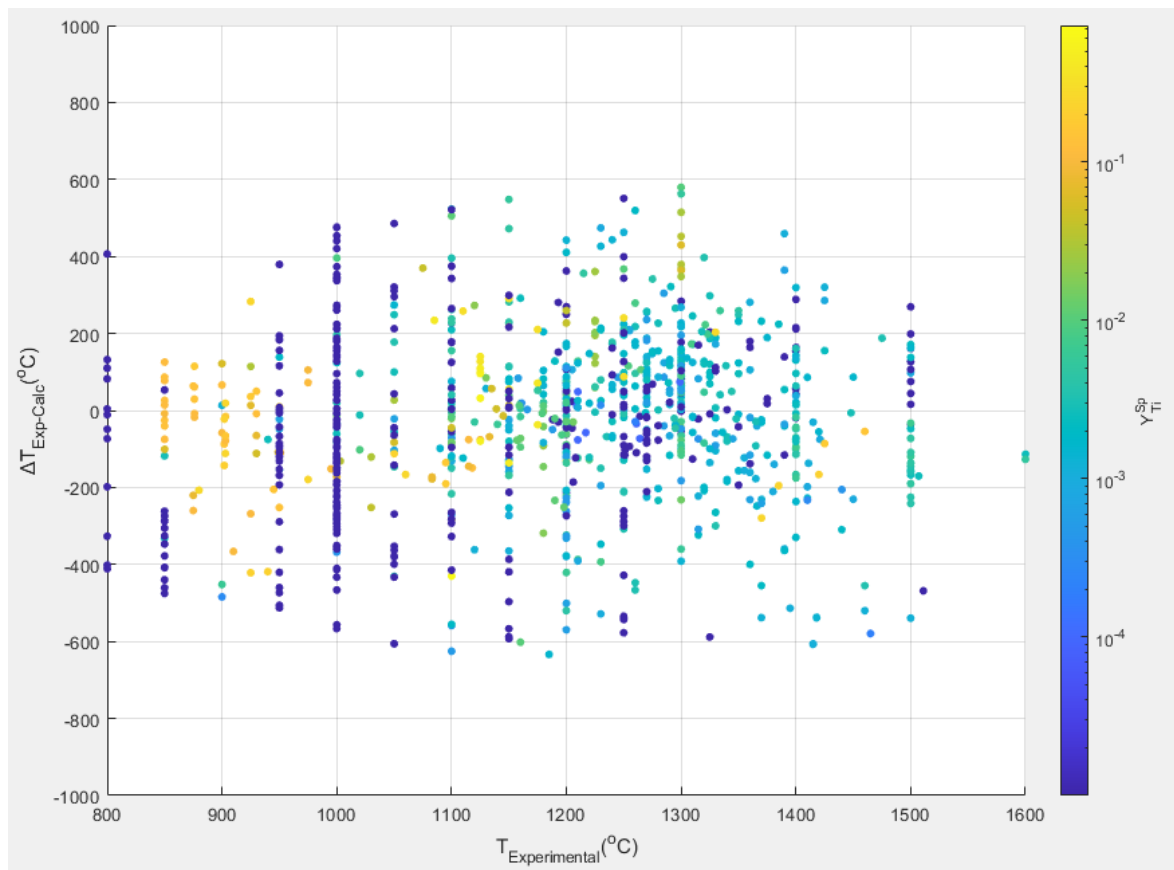


Figure 38: Chart with $\Delta T_{Exp-Calc}$ vs T_{Exp} in relation with Ti^{4+} in Y site of Spinel.

2.7. Recalibration of Liermann and Ganguly Opx/Sp Thermometer

Hans Peter Liermann in his PhD (Liermann 2000) with his advisor Jibamitra Ganguly had presented a new robust Geothermometer with Fe^{2+} -Mg fractionation between orthopyroxene and spinel. In their paper that was published in 2003 it has been shown their thermometric expression, which has been calibrated in conditions at 9-14 Kbar, 850-1250°C with some Cr-bearing experiments at 12.4 Kbar and 1000°C. Also the system of the experiments is FeO - MgO - Al_2O_3 - Cr_2O_3 - SiO_2 .

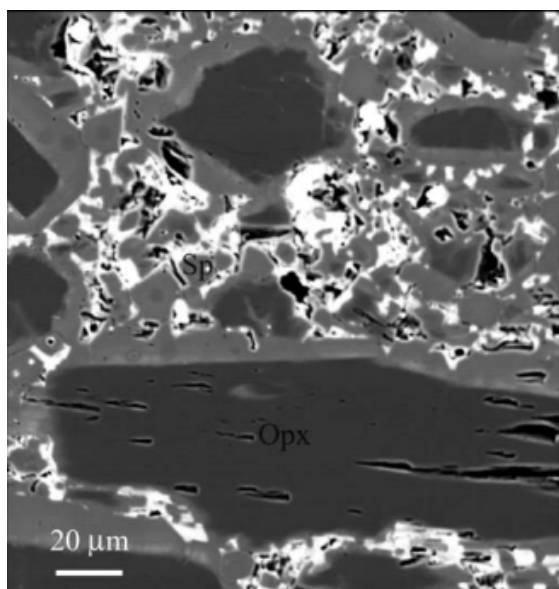


Figure 39: Image from a fractionation experiment at 1.27 GPa and 1150°C. The BSE image shows small spinel crystals (light gray) that are surrounding large Orthopyroxene crystals (dark gray), with a white material of PbO - PbF_2 flux that covers all the interstitial spaces. (Liermann & Ganguly 2003, Figure 2)

In addition the experimental study aimed to systematically determine the equilibrium constant for the fractionation of Fe-Mg in the aforementioned P-T conditions. The thermometer is calibrated with different schemes that are depending on how the experimental samples are treated.

Table 3: Thermometric expressions of Liermann and Ganguly.

T_{LG03}	Without Ti^{+4} Correction	With Ti^{+4} Correction
Fe^{+3} Correction with Charge Balance	$T_{LG03.1}(K) = \frac{1450 + 76.26P(GPa) + 2484Y_{Cr}^{Sp}}{\ln(K_D) + 0.6}$	$T_{LG03.1.Ti}(K) = \frac{1450 + 76.26P(GPa) + 2484Y_{Cr}^{Sp} + 3037(Y_{Fe^{+3}}^{Sp} + Y_{Ti}^{Sp})}{\ln(K_D) + 0.6}$
Fe^{+3} Correction with Mössbauer	$T_{LG03.2}(K) = \frac{1372 + 76.26P(GPa) + 2558Y_{Cr}^{Sp}}{\ln(K_D) + 0.55}$	$T_{LG03.2.Ti}(K) = \frac{1372 + 76.26P(GPa) + 2558Y_{Cr}^{Sp} + 3037(Y_{Fe^{+3}}^{Sp} + Y_{Ti}^{Sp})}{\ln(K_D) + 0.55}$
Al(Opx) effect and Fe^{+3} correction with Charge Balance	$T_{LG03.3}(K) = \frac{1217 + 76.26P(GPa) + 2345Y_{Cr}^{Sp} - 1863X_{Al}^{Opx}}{\ln(K_D) + 0.351}$	$T_{LG03.3.Ti}(K) = \frac{1217 + 76.26P(GPa) + 2345Y_{Cr}^{Sp} - 1863X_{Al}^{Opx} + 3037(Y_{Fe^{+3}}^{Sp} + Y_{Ti}^{Sp})}{\ln(K_D) + 0.351}$
Al(Opx) effect and Fe^{+3} Correction with Mössbauer	$T_{LG03.4}(K) = \frac{1174 + 76.26P(GPa) + 2309Y_{Cr}^{Sp} - 1863X_{Al}^{Opx}}{\ln(K_D) + 0.296}$	$T_{LG03.4.Ti}(K) = \frac{1174 + 76.26P(GPa) + 2309Y_{Cr}^{Sp} - 1863X_{Al}^{Opx} + 3037(Y_{Fe^{+3}}^{Sp} + Y_{Ti}^{Sp})}{\ln(K_D) + 0.296}$

In an erratum on 2007 the pressure coefficient term has been corrected to 76.26 instead of 122 which was in the original publication.

Parameters of the T_{LG03} equation

$$Y_{Cr}^{Sp} = \frac{Cr}{Cr + Al + Fe^{+3}} \quad (51)$$

$$X_{Al}^{Opx} = \frac{Al_2O_3}{Al_2O_3 + MgSiO_3 + FeSiO_3} \quad (52)$$

$$(Y_{Fe^{+3}} + Y_{Ti^{+4}})^{Sp} = \frac{Fe^{+3} + Ti^{+4}}{Fe^{+3} + Ti^{+4} + Cr + Al} \quad (53)$$

$$K_D = \frac{\left(\frac{Fe^{+2}}{Mg}\right)_{Sp}}{\left(\frac{Fe^{+2}}{Mg}\right)_{Opx}} \quad (54)$$

In Liermann's PhD (Liermann 2000) are included the microprobe analyses, with which the study was structured. The data consists of 277 samples, where 17 samples have $Y_{Cr}^{Sp} = 0.26$, 25 with $Y_{Cr}^{Sp} = 0.53$ and 23 with $Y_{Cr}^{Sp} = 0.76$. These samples have been included in the database as they have also contributed to the creation of T_{KG21} . Nevertheless, from the expressions of the thermometric equation, $T_{LG03.2.Ti}$ has the best performance in calculating the experimental samples, where it presents a standard deviation of 243°C. Below are the results of the geothermometer.

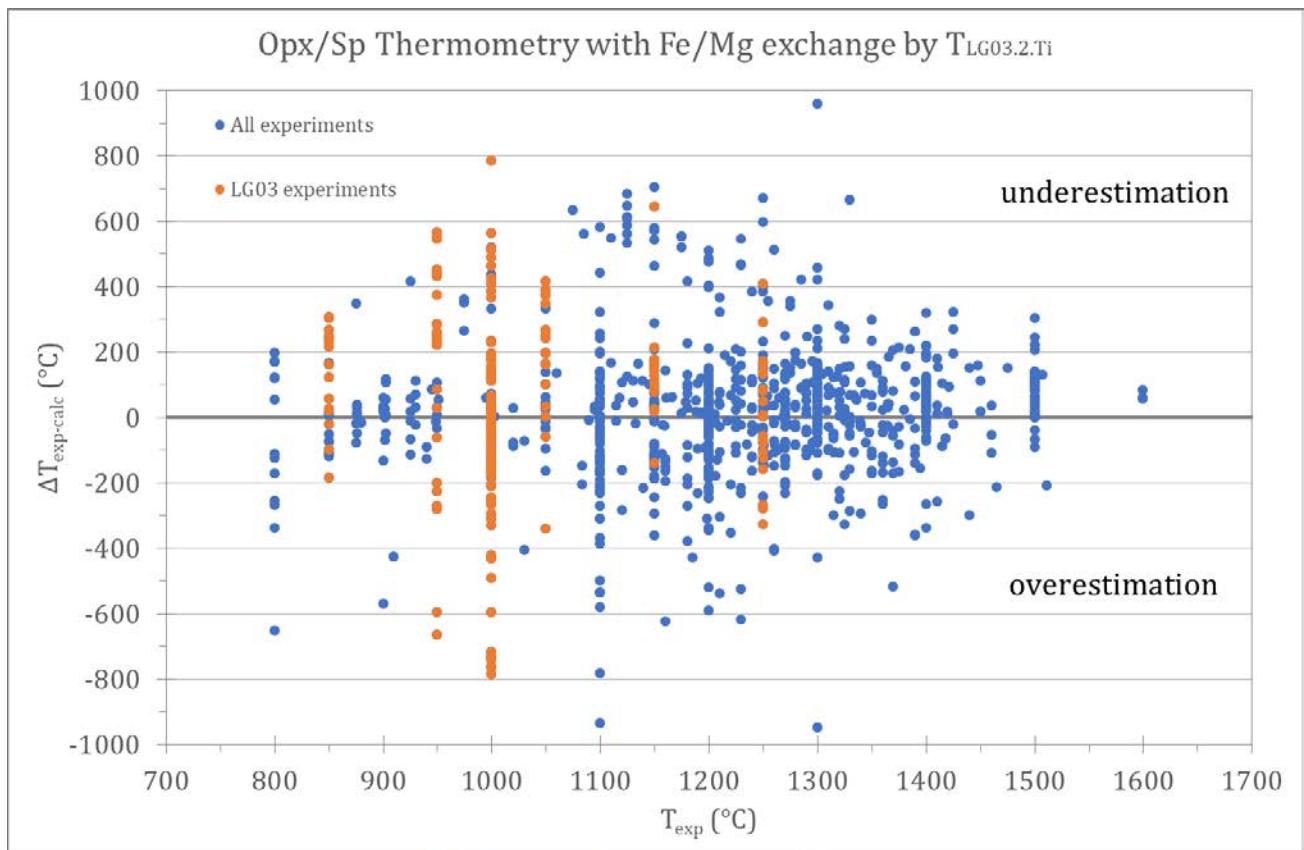


Figure40: $\Delta T_{Exp-Calc}$ vs T_{Exp} with the final experimental samples that T_{KG21} has been calibrated, where the temperature has been calculated by $T_{LG03.2.Ti}$. The orange dots are experimental samples from Liermann 2000.

By having a big amount of experimental samples with a big range in P-T conditions and multiple chemical systems, a recalibration of Liermann and Ganguly formulation was done, in order to extend the conditions of its applicability. The thermometer was calibrated with linear regression as the Arrhenius equation (9) with the same elimination procedure as T_{KG21} . From this method it has been created a formulation that has an overall

standard deviation of 226°C, by eliminating 190 samples or the 16% of the experimental data. Additionally the experiments that are within $\Delta T = \pm 200^\circ\text{C}$ is the 69% of the final experimental samples with a standard deviation of 103°C. The thermometer is the following:

$$T_{LG03.Rec} (^{\circ}\text{K}) = \frac{1714 + 81.05P(\text{GPa}) + 1856Y_{Cr}^{Sp} - 6462X_{Al}^{Opx} + 1851(Y_{Fe^{+3}}^{Sp} + Y_{Ti}^{Sp})}{\ln(K_D) + 0.39} \quad (55)$$

$$\text{With } \ln(K_D) = \ln \left(\frac{\left(\frac{Fe^{+2}}{Mg} \right)_{Sp}}{\left(\frac{Fe^{+2}}{Mg} \right)_{Opx}} \right) \quad (56)$$

$$Y_{Cr}^{Sp} = \frac{Cr}{Fe^{+3} + Ti^{+4} + Cr + Al} \quad (57)$$

$$X_{Al}^{Opx} = \frac{0.5Al}{0.5Al + Mg + Fe} \quad (58)$$

$$(Y_{Fe^{+3}} + Y_{Ti^{+4}})^{Sp} = \frac{Fe^{+3} + Ti^{+4}}{Fe^{+3} + Ti^{+4} + Cr + Al} \quad (53)$$

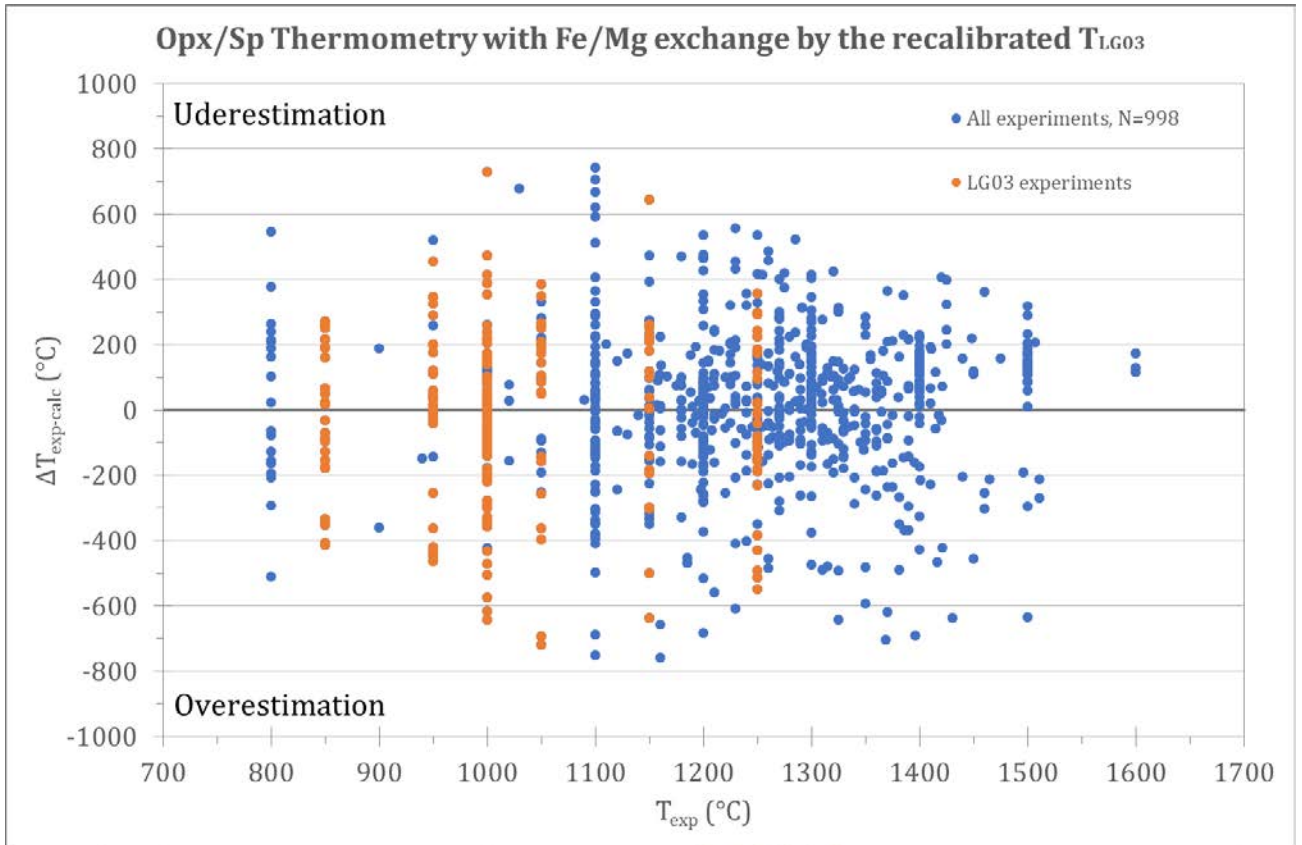


Figure 41: $\Delta T_{Exp-Calc}$ vs T_{Exp} final experimental results of the $T_{LG03.Rec}$. The orange dots are experimental samples from Liermann 2000 PhD.

In the new formula it is apparent that there are both minor and major changes. First, in the calculation of Y_{Cr}^{Sp} it has been added the Ti^{+4} content, because in the previous formulation Ti^{+4} was only in the $(Y_{Fe^{+3}}^{Sp} + Y_{Ti^{+4}}^{Sp})$ calculation. Furthermore, the calculation for the X_{Al}^{Opx} has remain the same but it is written with the cation

form and not with the oxides. In the indices of the parameters, ΔH , ΔV and ΔS have relatively small changes in relation to the chemical parameters that have change a lot , especially the X_{Al}^{Opx} which its effect is multiplied almost by 3.5 times. Finally, the results of the geothermometer are satisfactory, especially seeing that there is a good orientation of the samples at $\Delta T = 0$. In addition, it has a very good ability to calculate the experiments that the formula was originally created.

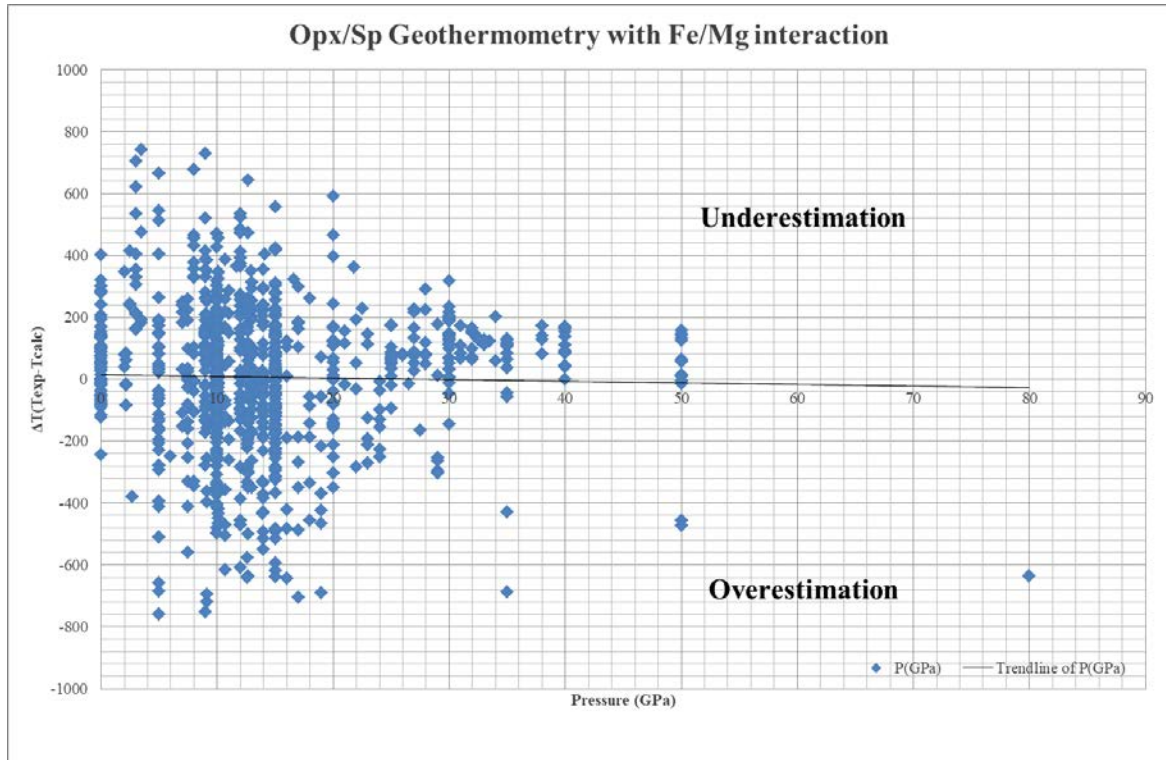


Figure 42: Chart with $\Delta T_{Exp-Calc}$ vs Pressure (GPa) to show the robustness of the Thermometer.

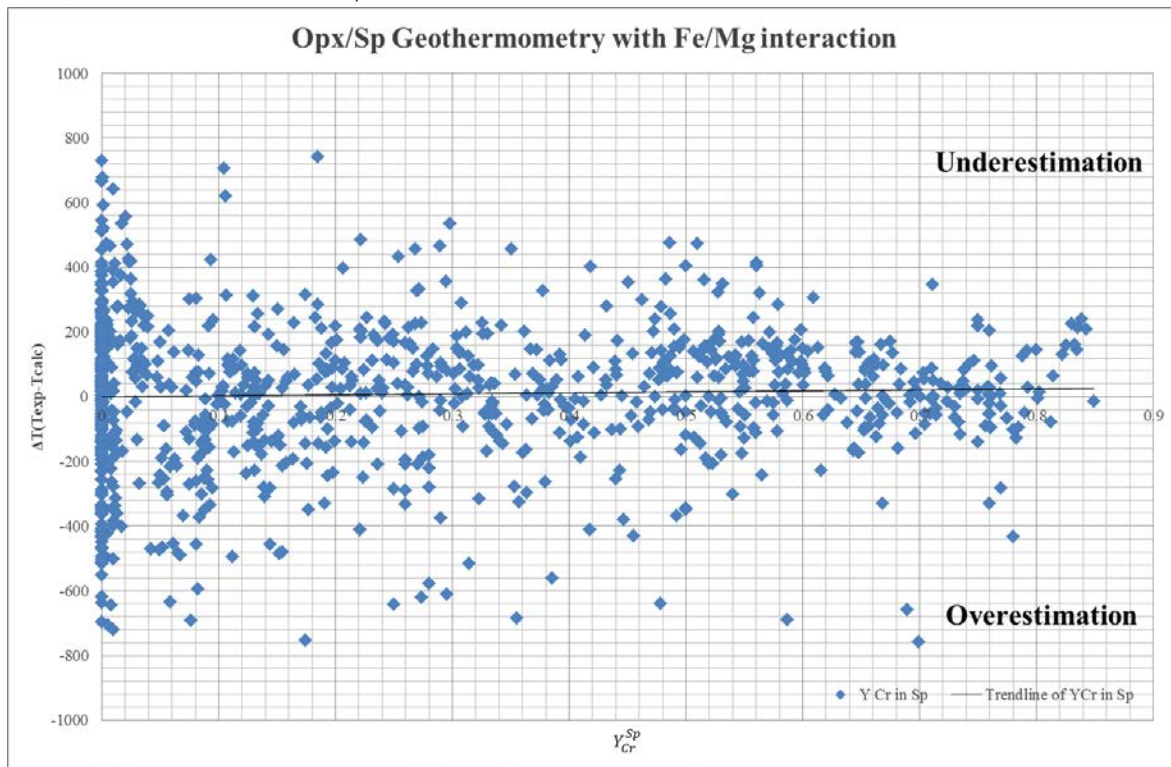


Figure 43: Chart with $\Delta T_{Exp-Calc}$ vs Y_{Cr}^{Sp} to show the robustness of the Thermometer.

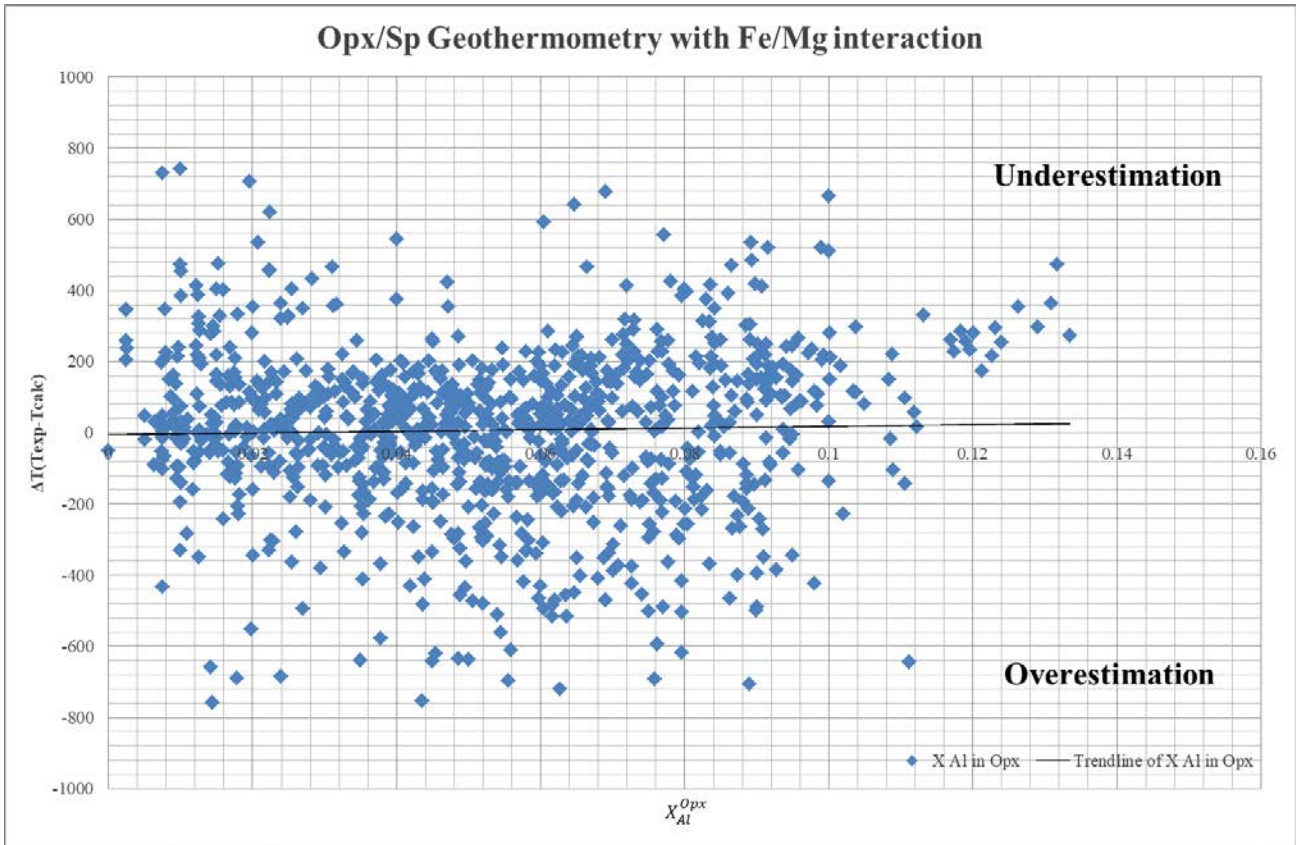


Figure 43: Chart with $\Delta T_{Exp-Calc}$ vs X_{Al}^{Opx} to show the robustness of the Thermometer.

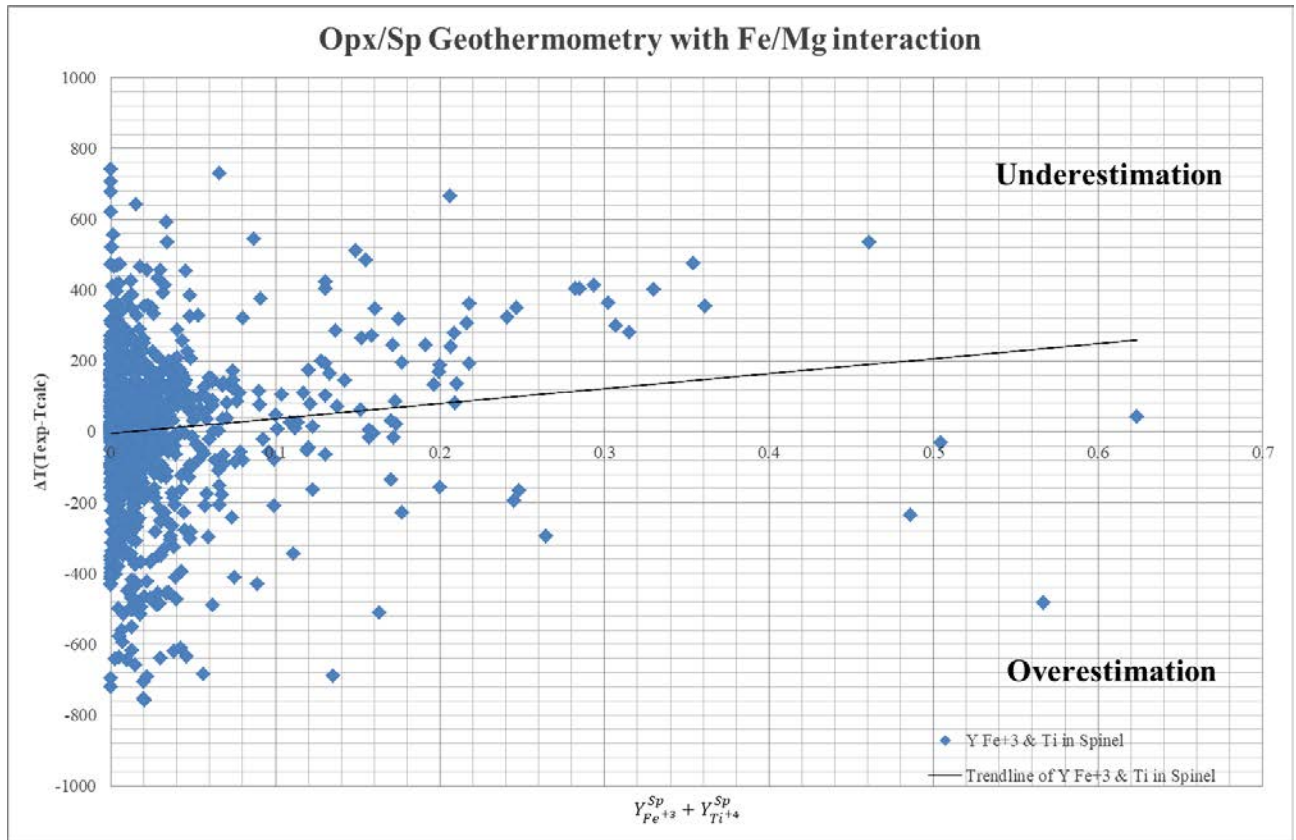


Figure 43: Chart with $\Delta T_{Exp-Calc}$ vs $Y_{Fe^{+3}}^{Sp} + Y_{Ti^{+4}}^{Sp}$ to show the robustness of the Thermometer.

From the above charts it is shown that Pressure, Y_{Cr}^{Sp} and X_{Al}^{Opx} have been well calibrated with a deviation of 0-30°C across their spectrum of values, in contrast to $Y_{Fe^{+3}}^{Sp} + Y_{Ti^{+4}}^{Sp}$ that have an increasingly underestimation as the term increases from 0°C to 240°C. However in the bulk of the samples in range of 0-0.1 the underestimation is among 0-40°C. Therefore when using the geothermometer, it is recommended that the values $Y_{Fe^{+3}}^{Sp} + Y_{Ti^{+4}}^{Sp}$ are relatively low, with knowing that it tends to underestimate the result as increases.

Chapter 3 Testing of T_{KG21} , $T_{LG03.Rec}$ and $T_{LG03.2.Ti}$ on Natural Samples

3.0 Introduction

To verify that the thermometers are sufficiently calibrated, they were tested on natural samples of various geotectonic environments. The Orthopyroxene and Spinel paragenesis takes parts in a variety of tectonic settings. The purpose of creating a thermometric model between those minerals is to further unfold their geologic history upon their petrogenetic processes. The environments that are going to be presented are Abyssal peridotites, Ophiolites and Continental Ultramafic rocks. Aim of this research is to explore the history of those aforementioned environments, while the thermometers are tested for their efficacy.

3.1 Abyssal Peridotites

Abyssal Peridotites are the products/residues of adiabatic decompression melting that are located in mid ocean ridges. Mantle upwelling beneath ocean ridges is the process that creates oceanic lithospheric mantle and oceanic crust. The source for the abyssal peridotites is the depleted mantle, whose composition in many cases varies because of compositional heterogeneities. For this tectonic setting, samples from Warren 2016 and Birner et al., 2018b databases are included, where 590 Opx/Sp pairs were found in various mid ocean ridges.

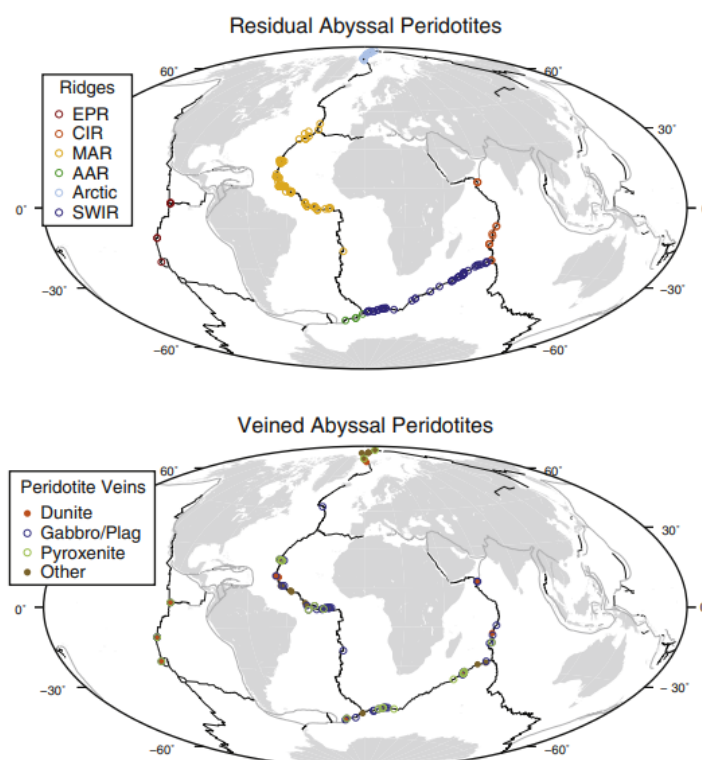


Figure 44: Global Distribution of abyssal peridotites samples categorized by their location, their lithologic type and their texture. (Warren 2016, figure 1)

The ocean ridges that have been studied are the East Pacific Rise (EPR), Central Indian Ridge/Carlsberg Ridge (CIR), Mid-Atlantic Ridge (MAR), American-Antarctic Ridge (AAR), Gakkel Ridge (GAK), Lena Trough (LT) and the Southwest Indian Ridge (SWIR). Furthermore, peridotites in those studies have a variety of lithologies such as Hartzburgites, Lherzolites, Dunites with some of them containing veins of Gabbro or Pyroxenite in them (15,3% of the Opx/Sp pair samples). By having the aforementioned in mind, the results of the Thermometers are the following.

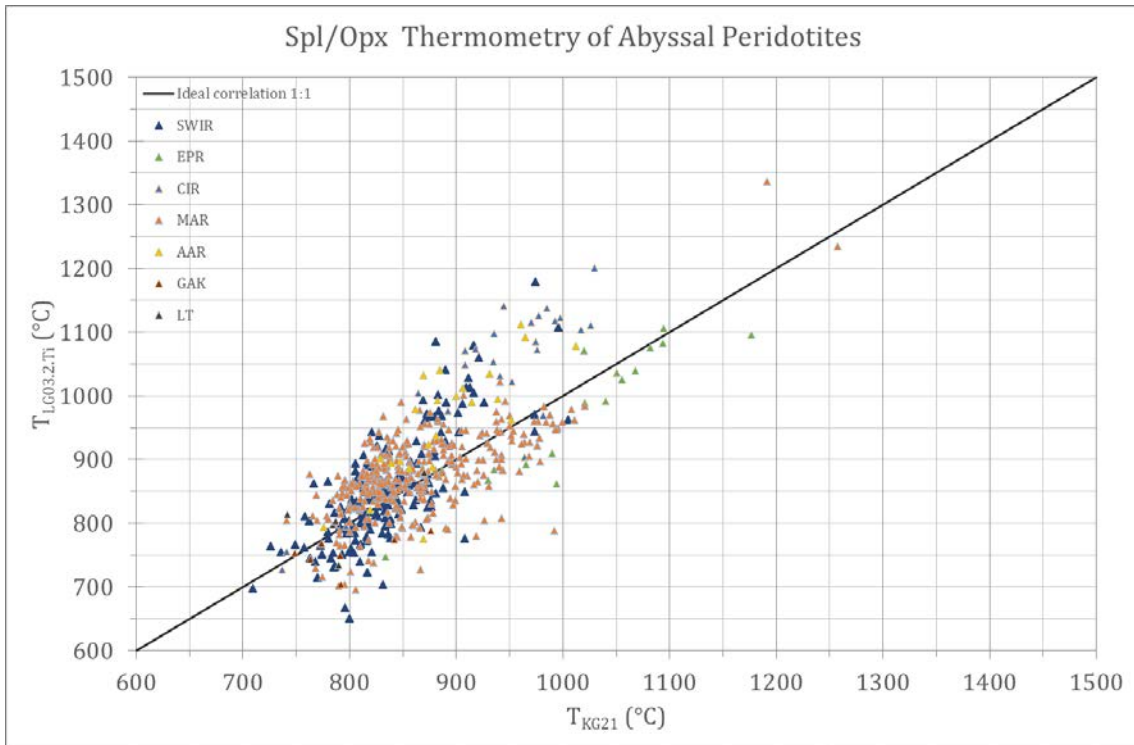


Figure 45: Diagram of $T_{LG03.2.Ti}$ vs T_{KG21} in natural samples from abyssal peridotites.

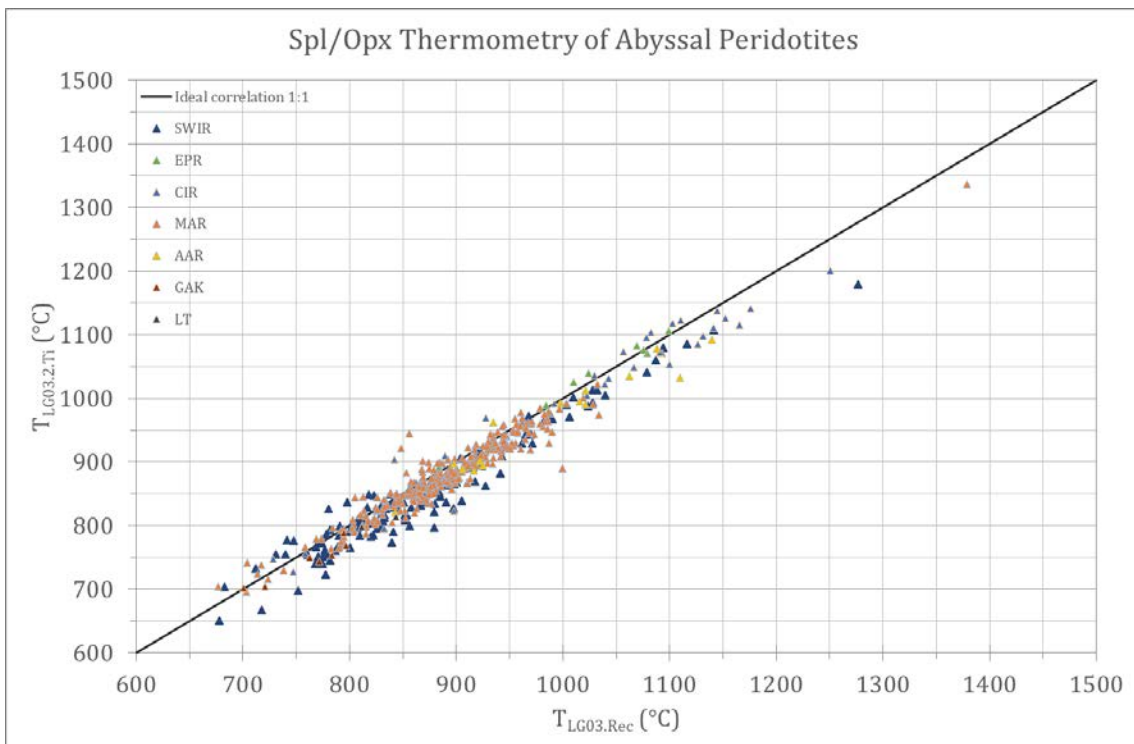


Figure 46: Diagram of $T_{LG03.2.Ti}$ vs $T_{LG03.Rec}$ in natural samples from abyssal peridotites.

In the comparison of T_{KG21} with $T_{LG03.2.Ti}$ it is shown that there is a positive correlation with a deviation within ± 200 °C. The temperatures of T_{KG21} from the abyssal peridotites vary from 709 °C to 1259 °C with an average of 865 °C and a standard deviation of 69.4 °C. On the other hand $T_{LG03.2.Ti}$ has a variation 650 °C-1336°C with an average of 886 °C and a standard deviation of 91.2 °C.

These measurements are to be expected because the diffusion of Opx/Sp with Fe^{+2}/Mg in these environments had been re-equilibrating to lower temperatures. In addition, the $T_{LG03.Rec}$ has a temperature range of 678 °C-1378 °C and an overall standard deviation of 95.8 °C, with an average of 903 °C. Also, in figure 46 it is visible that there is an almost ideal correlation between $T_{LG03.Rec}$ and $T_{LG03.2.Ti}$ and that $T_{LG03.Rec}$ is overestimating for 30°C in relation to $T_{LG03.2.Ti}$.

3.2 Continental Peridotites

Magmatic processes that can create ultramafic rocks take place in Continental zones. During the ascent of the magmas, parts of the lithospheric mantle detach and attach within the magmatic bodies creating the xenoliths. These samples are very important because they can provide us with information about the temperature of their lithospheric mantle. Locations of those samples are Eifel, Daoxian, Styrian Basin, Avacha, Lanzo, Dish Hill, Rio Grande Rift, Malaita and Central Alps. The results are the following:

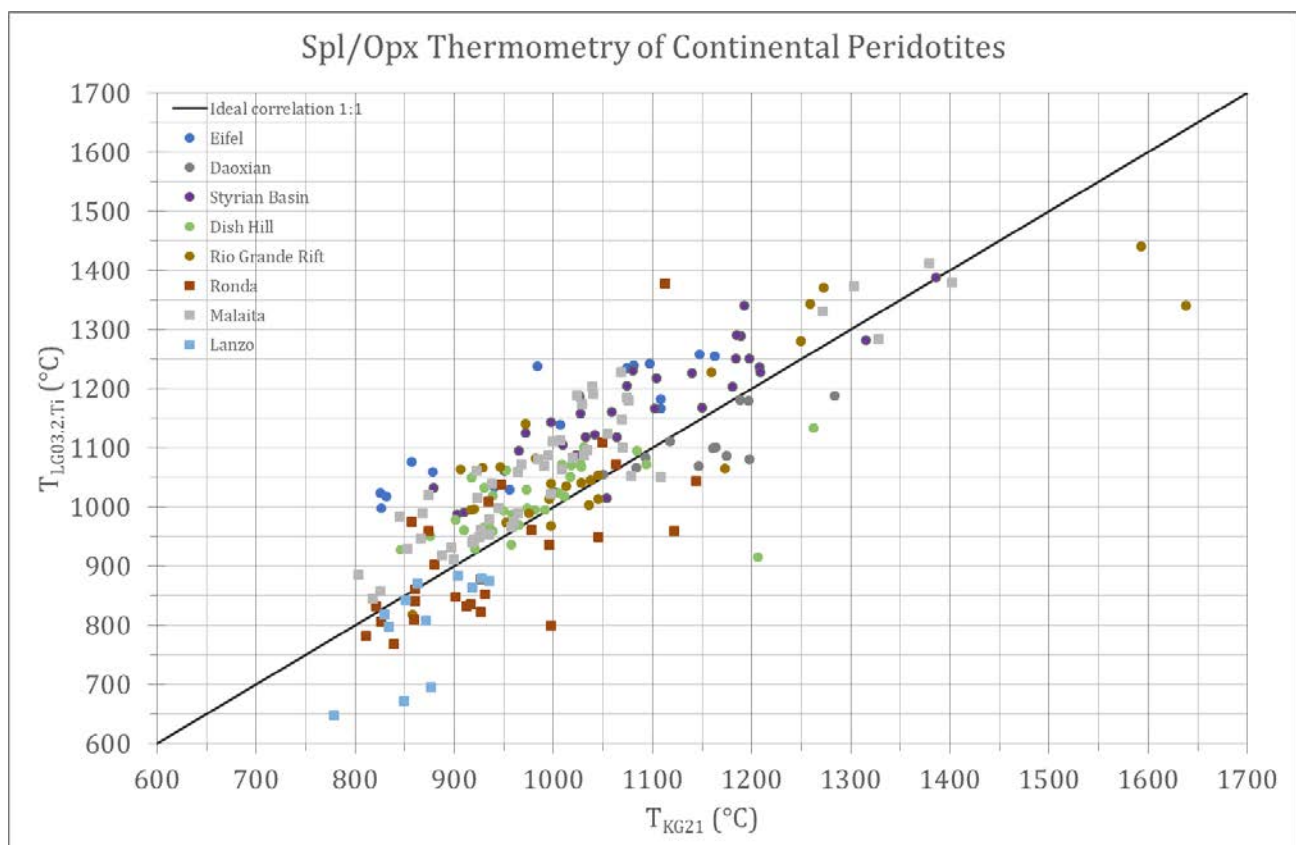


Figure 47: Diagram of $T_{LG03.2.Ti}$ vs T_{KG21} in natural samples from continental peridotites.

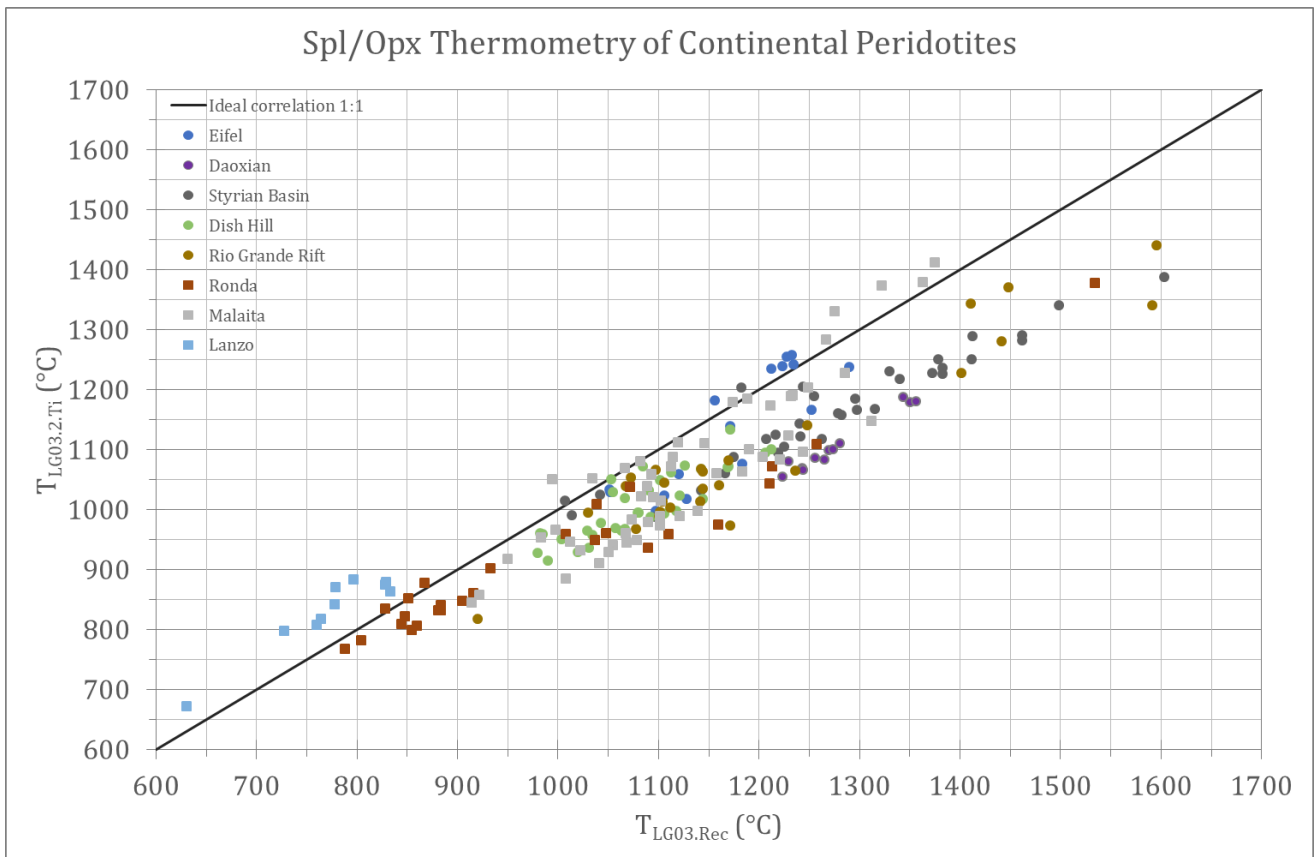


Figure 48: Diagram of $T_{LG03.2.Ti}$ vs $T_{LG03.Rec}$ in natural samples from continental peridotites.

First by the comparison $T_{LG03.2.Ti}$ with T_{KG21} it presented that there is a correlation within $\pm 150^{\circ}\text{C}$, where $T_{LG03.2.Ti}$ has higher values in samples of Eifer, Styrian basin, Dish Hill, while in Ronda, Daoxian and in some samples of Dish Hill and Rio Grande Rift the opposite occurs. Secondly, the comparison of $T_{LG03.2.Ti}$ with $T_{LG03.Rec}$ shows a robust correlation with $T_{LG03.Rec}$ capturing higher values as temperature rises. This trend is expected because $T_{LG03.2.Ti}$ has been calibrated to temperatures of 850°C - 1250°C , while the recalibrated expression has been calibrated to a range of 800 - 1600°C . As a result the recalibrated version is expected to have more trustworthy results.

Furthermore the temperature range for T_{KG21} is 779°C - 1638°C , while in $T_{LG03.2.Ti}$ is 671°C - 1440°C and in $T_{LG03.Rec}$ is 63°C - 1603°C . The temperatures range in this type of rocks because the **Fe/Mg exchange** can record temperatures from the area from which they were detached, to subsequent reactivations of the elements that occur at lower temperatures. In addition, there is a variety of Opx/Sp pairs where the analysis is in core or rims of the minerals or in derivatives of a metasomatic process or is even the result of subsequent crystallization such as neoblast. The aforementioned processes give us different results and this is the reason big temperature spans.

3.3. Ophiolites

Ophiolites are lithologic sequences that created in oceanic tectonic environments and they have been annexed through tectonic processes in incremental prisms. The way they are created varies depending on the tectonic processes that take place within the oceans as well as on the boundaries between ocean and continents. These settings are classified as subduction related and those are the forearcs, backarcs and volcanic arcs. Also there are the subduction unrelated ophiolites, that can be subdivided to continental margins, mid ocean ridges and plume type. (Dilek and Furnes 2014).

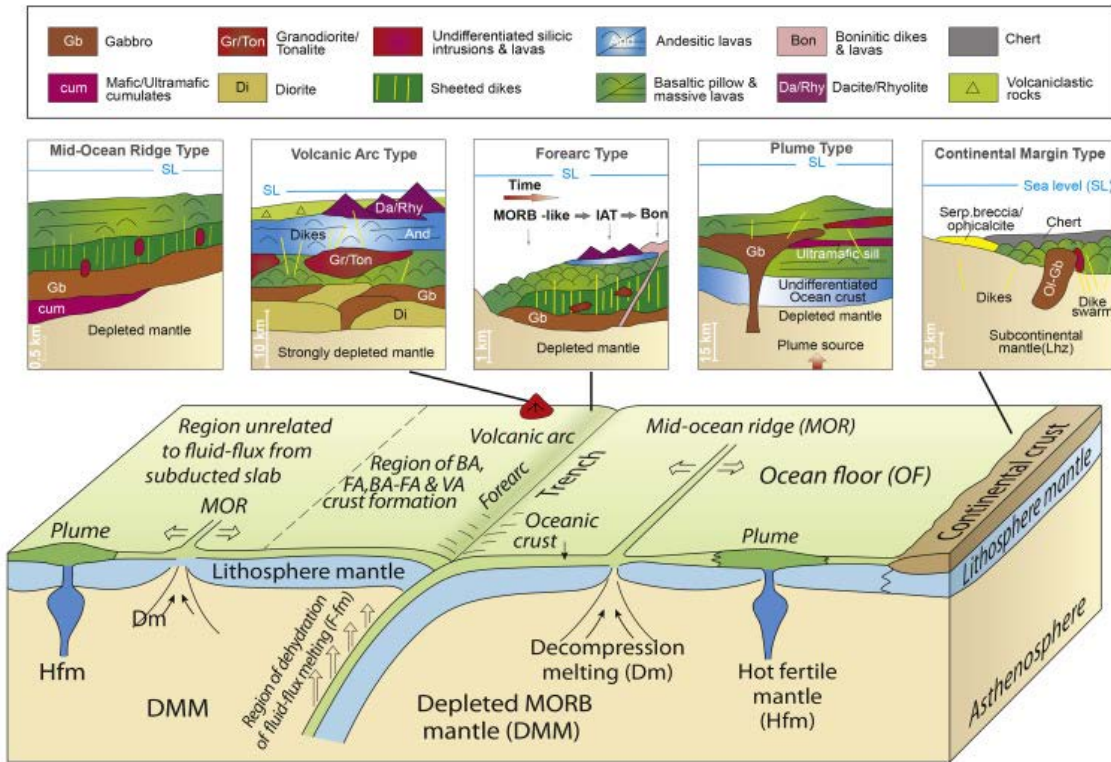


Figure 49: Schematic presentation of the variety of ophiolites and their tectonic processes (Furnes et al 2020),

For those types of tectonic settings the locations of the samples that are forearcs is Antalya, New Caledonia, Izu-Bonin-Marianna (IBM), Tonga, Dazhuqu, for continental margins are Central Alps and Avacha and for plume/hotspots are Hawaii and Samoa Islands. The results of these samples are the following:

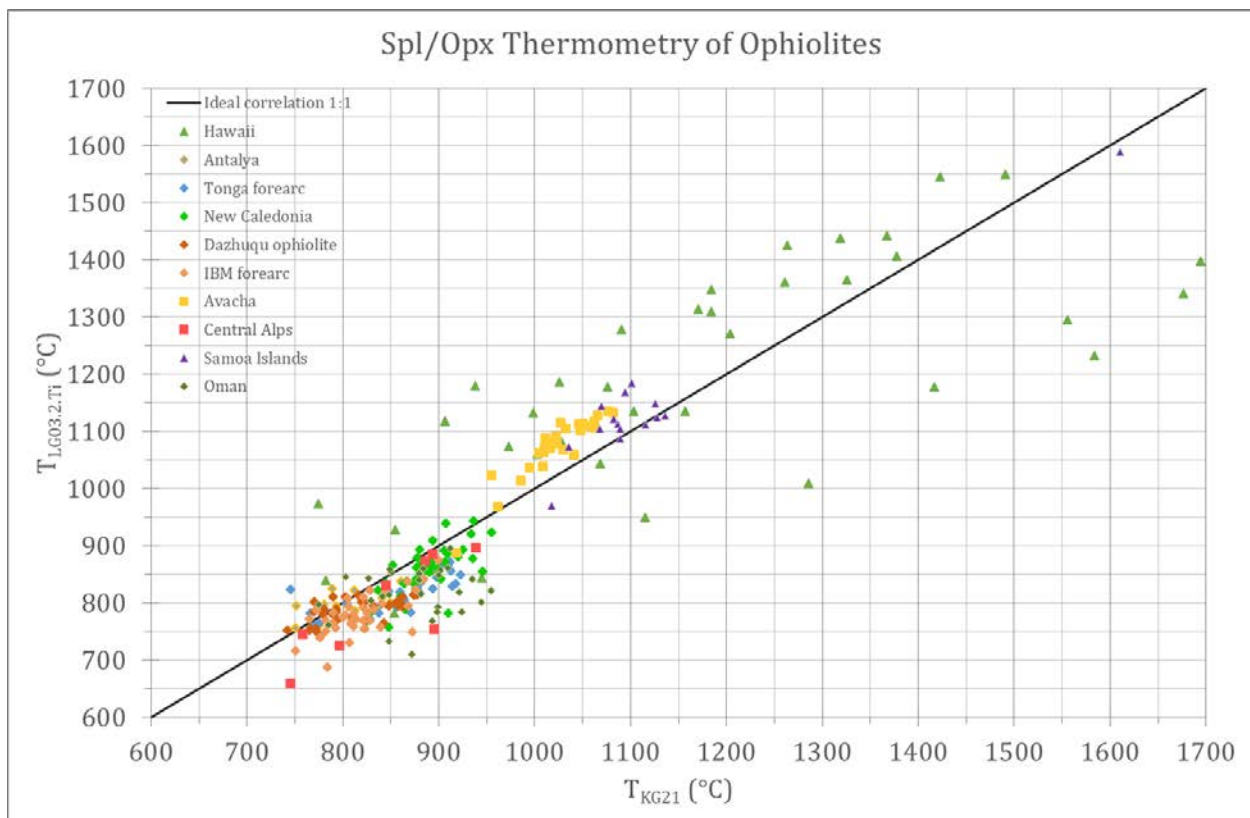


Figure 50: Plot of $T_{LG03.2.Ti}$ vs T_{KG21} in natural samples from Ophiolites.

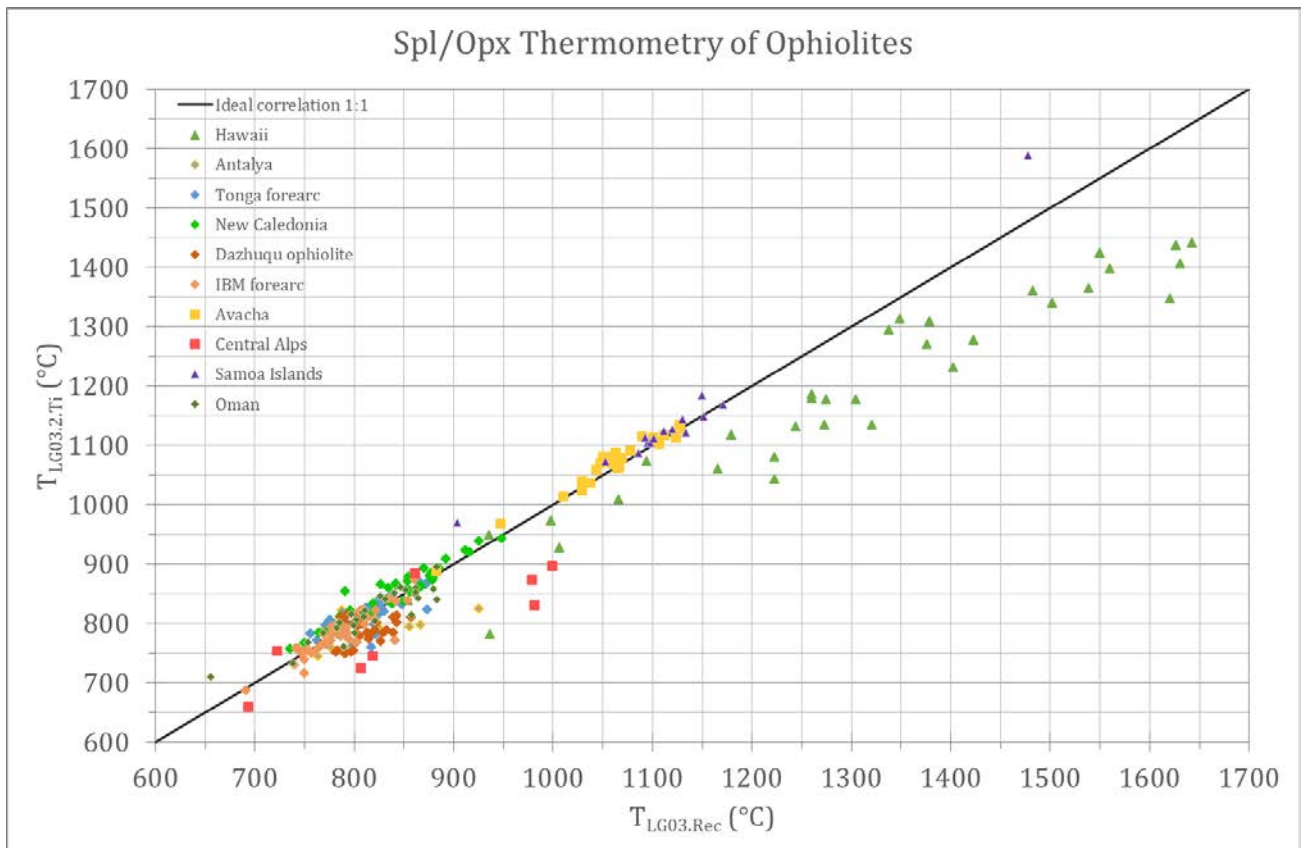


Figure 51: Plot of $T_{LG03.2.Ti}$ vs $T_{LG03.Rec}$ in natural samples from Ophiolites.

For the different ophiolitic types the results have their own temperature spans. In Forearcs T_{KG21} has a range between 742-955°C, for $T_{LG03.2.Ti}$ is 678-942°C and for $T_{LG03.Rec}$ is 655-948°C. These results showed that the new thermometers tend to overestimate in relation to $T_{LG03.2.Ti}$ by 20°C on average. In Continental Margins the Avacha results are concentrated in 860-1135°C while in Central Alps the results are within 655-995°C, with $T_{LG03.Rec}$ and T_{KG21} overestimating in Central Alps and slightly underestimating in Avacha in relation to $T_{LG03.2.Ti}$. Finally, in Plume type rocks from Hawaii and Samoa islands it is showed that there is a big range of calculated temperatures. The values vary for T_{KG21} from 774°C to 1695°C, for $T_{LG03.2.Ti}$ is 854-1589°C and for $T_{LG03.Rec}$ is 935-1642°C. In the comparison between T_{KG21} and $T_{LG03.2.Ti}$ there is an unclear discrepancy with a $\Delta T = \pm 250^\circ\text{C}$ for the samples of Hawaii, while for the Samoa islands there a better correlation. On the contrary, in the comparison of $T_{LG03.Rec}$ with $T_{LG03.2.Ti}$ there is an overestimation of 120°C on average for the samples of Hawaii, while for the samples of the Samoa islands there is a 20°C overestimation.

3.4 Discussion

The calculated temperatures for all the tectonic environments have satisfying results, as they depict values that are expected based on their origin. First, the goal for $T_{LG03.Rec}$ to be a recalibrated form, that has extended P-T conditions of applicability, has been succeeded. The thermometer has a one by one correlation with the original $T_{LG03.2.Ti}$ but in temperatures greater than 1250°C the thermometer has more accurate results, while it also has an overestimation at higher temperatures which is expected. Also, $T_{LG03.Rec}$ seems to have a greater standard deviation than $T_{LG03.2.Ti}$, but through its calibration it is more accurate rather than precise. Furthermore, for the T_{KG21} it is shown that the geothermometer has very accurate and precise results with an overestimation in ophiolites an underestimation in Continental and Abyssal Peridotites compared with the Liermann and Ganguly 2003 thermometric expressions. The different result of T_{KG21} with the T_{LG03} thermometers is because the handling of the chemical composition within the equations is different, as seen in

2.6 and 2.7. To summarize, a statistical appendix with the results of the thermometers for each locality is the following:

Locality	Reference	No.Samples	T _{K21} (°C)					T _{K32T1} (°C)					T _{K32T2} (°C)				
			Average	Minimum	Maximum	St.Dev	St.Dev	Average	Minimum	Maximum	St.Dev	St.Dev	Average	Minimum	Maximum	St.Dev	St.Dev
EPR	Warren 2016	19	998.03	804.27	1176.37	95.13	962.28	746.74	1106.04	106.18	961.56	728.55	1099.26	101.05			
CIR	Warren 2016	26	932.52	736.51	1029.46	77.68	1031.71	726.94	1200.75	120.38	1044.20	747.24	1250.51	129.18			
MAAR	Warren 2016	337	863.93	741.03	1257.21	61.42	877.02	696.30	1336.64	64.47	886.49	676.73	1584.29	77.20			
AAR	Warren 2016	23	888.89	775.90	1012.04	53.85	958.42	774.89	1112.46	91.71	979.61	783.94	1139.69	98.47			
SWIR	Birner et al., 2018b	39	826.45	749.56	908.14	33.41	819.22	666.70	913.72	54.69	831.67	683.23	941.63	60.12			
SWIR	Warren 2016	133	837.58	709.29	1005.24	51.75	861.19	650.14	1178.28	91.88	884.48	678.19	1276.70	94.87			
GAK	Warren 2016	8	796.89	748.38	875.94	42.13	747.90	701.61	788.20	31.39	764.10	700.57	796.98	35.19			
LT	Warren 2016	5	794.35	741.52	869.84	46.58	805.85	734.75	879.89	51.65	824.12	744.21	885.32	51.97			
Syrian Basin	Aradi et al., 2020	34	1083.86	879.74	1386.50	115.38	1166.62	987.58	1387.31	98.30	1277.98	1007.64	1603.43	135.83			
Rio Grande Rift	Schaffer et al., 2019	26	1073.39	857.93	1638.23	194.00	1094.53	817.32	1440.34	148.32	1201.73	920.75	1595.61	172.69			
Eifel	Witt-Eickens & O'Neill, 2005	16	993.25	826.09	1162.86	121.67	1136.42	997.07	1256.56	100.40	1171.49	1051.70	1290.13	72.68			
Daonian	Zhang et al., 2020	12	1155.07	1050.43	1284.16	62.65	1107.82	1054.38	1187.40	47.48	1278.25	1223.94	1356.96	46.88			
Lanzo	Aoki et al., 2020	16	838.73	692.87	935.62	71.47	736.95	488.42	883.16	141.31	666.24	397.34	833.73	157.82			
Dish Hill	Luffi et al., 2009	34	983.55	846.12	1262.74	83.72	1008.78	914.19	1132.82	56.64	1082.22	980.25	1212.55	62.90			
Ronda	Soustelle et al., 2009 , Obata, 1980	27	940.83	811.76	1144.19	96.33	919.95	767.61	1377.47	131.61	990.09	788.76	1534.81	175.07			
Antalya	Caran et al., 2010	14	809.21	750.55	895.92	42.80	797.31	743.89	855.87	31.21	815.04	763.72	925.72	47.03			
Tonga	Birner et al., 2018a	32	862.36	746.23	922.68	46.52	816.61	759.58	871.46	29.16	817.54	756.14	874.01	31.24			
Oman	Gaillard, 2002	28	874.50	774.71	954.69	46.09	817.03	709.85	895.86	41.78	816.78	655.88	883.31	50.25			
IBM	Parkinson & Pearce, 1998, 박준희, 2019	39	819.69	750.97	899.84	35.02	779.93	687.12	873.65	36.25	784.75	691.15	860.76	35.58			
Malaita	Ishikawa et al., 2004	53	1000.81	803.65	1402.45	133.29	1066.07	844.30	1411.74	132.27	1129.46	914.69	1375.34	109.24			
New Caledonia	Xu et al., 2021	38	888.45	825.08	955.23	31.78	854.72	756.96	942.96	44.91	843.67	735.73	948.56	48.56			
Hawaii	Sen, 1988	38	1180.16	774.74	1694.81	244.24	1197.59	782.05	1549.31	198.69	1318.36	825.94	1800.47	252.92			
Samoa Islands	Ashley 2019	15	1123.21	1017.58	1610.68	138.72	1144.71	970.34	1589.16	132.34	1124.71	903.27	1477.11	115.57			
Avacta	Ishimaru et al., 2007 , Ionov 2010	28	1022.91	919.10	1082.00	36.99	1072.77	887.67	1133.73	52.95	1065.52	882.83	1128.33	54.51			
Central Alps	Müntener et al., 2010, Kalt et al., 1995, Kalt & Altherr, 1996, Schmädicke & Evans, 1997	14	878.54	746.18	997.61	73.31	775.45	658.51	895.00	79.21	828.25	694.25	999.64	107.57			

Table 5: Appendix with the before mentioned Natural Samples and their statistical results.

References

- Anderson, G. M. (2005). *Thermodynamics of natural systems*. Cambridge University Press. 97-105
- Aoki, T., Ozawa, K., Bodinier, J. L., Boudier, F., & Sato, Y. (2020). Thermal and decompression history of the Lanzo Massif, northern Italy: Implications for the thermal structure near the lithosphere–asthenosphere boundary. *Lithos*, 372, 105661.
- Aradi, L. E., Bali, E., Patkó, L., Hidas, K., Kovács, I. J., Zanetti, A., ... & Szabó, C. (2020). Geochemical evolution of the lithospheric mantle beneath the Styrian Basin (Western Pannonian Basin). *Lithos*, 378, 105831.
- Ashley, A. W. (2019). *Water Systematics of Samoan Peridotite Xenoliths*.
- Bertrand, P., & Mercier, J. C. C. (1985). The mutual solubility of coexisting ortho- and clinopyroxene: toward an absolute geothermometer for the natural system?. *Earth and Planetary Science Letters*, 76(1-2), 109-122.
- Birner, S. K., Cottrell, E., Warren, J. M., Kelley, K. A., & Davis, F. A. (2018). Peridotites and basalts reveal broad congruence between two independent records of mantle fO₂ despite local redox heterogeneity. *Earth and Planetary Science Letters*, 494, 172-189.
- Birner, S. K. (2018). *Variations in the Oxygen Fugacity of the Upper Mantle*. Stanford University.
- BREY, G. P., & Köhler, T. (1990). Geothermobarometry in four-phase lherzolites II. New thermobarometers, and practical assessment of existing thermobarometers. *Journal of Petrology*, 31(6), 1353-1378.
- Caran, Ş., Çoban, H., Flower, M. F., Ottley, C. J., & Yılmaz, K. (2010). Podiform chromitites and mantle peridotites of the Antalya ophiolite, Isparta Angle (SW Turkey): implications for partial melting and melt–rock interaction in oceanic and subduction-related settings. *Lithos*, 114(3-4), 307-326.
- Dilek, Y., & Furnes, H. (2014). Ophiolites and their origins. *Elements*, 10(2), 93-100.
- Droop, G. T. R. (1987). A general equation for estimating Fe³⁺ concentrations in ferromagnesian silicates and oxides from microprobe analyses, using stoichiometric criteria. *Mineralogical Magazine*, 51(361), 431-435.
- Engi, M. (1983). Equilibria involving Al-Cr spinel: Mg-Fe exchange with olivine. Experiments, thermodynamic analysis, and consequences for geothermometry. *Amer. Jour. Sci.*, 283, 29-71.
- Ferracutti, G. R., Gargiulo, M. F., Ganuza, M. L., Bjerg, E. A., & Castro, S. M. (2015). Determination of the spinel group end-members based on electron microprobe analyses. *Mineralogy and Petrology*, 109(2), 153-160.
- Furnes, H., Dilek, Y., Zhao, G., Safonova, I., & Santosh, M. (2020). Geochemical characterization of ophiolites in the Alpine-Himalayan Orogenic Belt: Magmatically and tectonically diverse evolution of the Mesozoic Neotethyan oceanic crust. *Earth-Science Reviews*, 103258.
- Gerbert-Gaillard, L. (2002). *Caractérisation géochimique des péridotites de l'ophiolite d'Oman: processus magmatiques aux limites lithosphère/asthénosphère* (Doctoral dissertation, Université Montpellier II-Sciences et Techniques du Languedoc).

- Ionov, D. A. (2010). Petrology of mantle wedge lithosphere: new data on supra-subduction zone peridotite xenoliths from the andesitic Avacha volcano, Kamchatka. *Journal of Petrology*, 51(1-2), 327-361.
- Ishikawa, A., Maruyama, S., & Komiya, T. (2004). Layered lithospheric mantle beneath the Ontong Java Plateau: implications from xenoliths in alnöite, Malaita, Solomon Islands. *Journal of Petrology*, 45(10), 2011-2044.
- Ishimaru, S., Arai, S., Ishida, Y., Shirasaka, M., & Okrugin, V. M. (2007). Melting and multi-stage metasomatism in the mantle wedge beneath a frontal arc inferred from highly depleted peridotite xenoliths from the Avacha volcano, southern Kamchatka. *Journal of Petrology*, 48(2), 395-433.
- Kalt, A., Altherr, R., & Hanel, M. (1995). Contrasting PT conditions recorded in ultramafic high-pressure rocks from the Variscan Schwarzwald (FRG). *Contributions to Mineralogy and Petrology*, 121(1), 45-60.
- Kalt, A., & Altherr, R. (1996). Metamorphic evolution of garnet-spinel peridotites from the Variscan Schwarzwald (Germany). *Geologische Rundschau*, 85(2), 211-224.
- Liermann, H. P. (2000). Thermodynamics and kinetics of Fe²⁺-Mg exchange between orthopyroxene and spinel: Experimental calibrations and applications.
- Liermann, H. P., & Ganguly, J. (2003). Fe²⁺-Mg fractionation between orthopyroxene and spinel: experimental calibration in the system FeO-MgO-Al₂O₃-Cr₂O₃-SiO₂, and applications. *Contributions to Mineralogy and Petrology*, 145(2), 217-227.
- Luffi, P., Saleeby, J. B., Lee, C. T. A., & Ducea, M. N. (2009). Lithospheric mantle duplex beneath the central Mojave Desert revealed by xenoliths from Dish Hill, California. *Journal of Geophysical Research: Solid Earth*, 114(B3).
- Parkinson, I. J., & Pearce, J. A. (1998). Peridotites from the Izu-Bonin-Mariana forearc (ODP Leg 125): evidence for mantle melting and melt-mantle interaction in a supra-subduction zone setting. *Journal of Petrology*, 39(9), 1577-1618.
- Morimoto, N. (1988). Nomenclature of pyroxenes. *Mineralogy and Petrology*, 39(1), 55-76.
- Mukherjee, A. B., Bulatov, V., & Kotelnikov, A. (1990). New high PT experimental results on orthopyroxene-chrome spinel equilibrium and a revised orthopyroxene-spinel cosmo thermometer. In *Lunar and Planetary Science Conference Proceedings (Vol. 20, pp. 299-308)*.
- Mukhopadhyay, B., Basu, S., & Holdaway, M. J. (1993). A discussion of Margules-type formulations for multicomponent solutions with a generalized approach. *Geochimica et Cosmochimica Acta*, 57(2), 277-283
- Müntener, O., Manatschal, G., Desmurs, L., & Pettke, T. (2010). Plagioclase peridotites in ocean-continent transitions: refertilized mantle domains generated by melt stagnation in the shallow mantle lithosphere. *Journal of Petrology*, 51(1-2), 255-294.
- Obata, M. (1980). The Ronda peridotite-garnet-lherzolite, spinel-lherzolite, and plagioclase-lherzolite facies and the PT trajectories of a high-temperature mantle intrusion. *Journal of Petrology*, 21(3), 533-572.
- . (2019). Influence of partial melting and melt-mantle interaction on PGE geochemistry of the Mariana forearc peridotites (Doctoral dissertation, □□□□□ □□□).

- Robie, R. A., & Hemingway, B. S. (1995). Thermodynamic properties of minerals and related substances at 298.15 K and 1 bar (105 Pascals) pressure and at higher temperatures (Vol. 2131). US Government Printing Office.
- Schaffer, L. A., Peslier, A. H., Brandon, A. D., Bizimis, M., Gibler, R., Norman, M., & Harvey, J. (2019). Effects of melting, subduction-related metasomatism, and sub-solidus equilibration on the distribution of water contents in the mantle beneath the Rio Grande Rift. *Geochimica et Cosmochimica Acta*, 266, 351-381.
- Schmädicke, E., & Evans, B. W. (1997). Garnet-bearing ultramafic rocks from the Erzgebirge, and their relation to other settings in the Bohemian Massif. *Contributions to Mineralogy and Petrology*, 127(1), 57-74.
- Sen, G. (1988). Petrogenesis of spinel lherzolite and pyroxenite suite xenoliths from the Koolau shield, Oahu, Hawaii: implications for petrology of the post-eruptive lithosphere beneath Oahu. *Contributions to Mineralogy and Petrology*, 100(1), 61-91.
- Soustelle, V., Tommasi, A., Bodinier, J. L., Garrido, C. J., & Vauchez, A. (2009). Deformation and reactive melt transport in the mantle lithosphere above a large-scale partial melting domain: the Ronda Peridotite Massif, Southern Spain. *Journal of Petrology*, 50(7), 1235-1266.
- Stevens, R. E. (1944). Composition of some chromites of the western hemisphere. *American Mineralogist: Journal of Earth and Planetary Materials*, 29(1-2), 1-34.
- Taylor, W. R. (1998). An experimental test of some geothermometer and geobarometer formulations for upper mantle peridotites with application to the thermobarometry of fertile lherzolite and garnet websterite. *Neues Jahrbuch für Mineralogie-Abhandlungen*, 381-408.
- Warren, J. M. (2016). Global variations in abyssal peridotite compositions. *Lithos*, 248, 193-219.
- Witt-Eickchen, G., & O'Neill, H. S. C. (2005). The effect of temperature on the equilibrium distribution of trace elements between clinopyroxene, orthopyroxene, olivine and spinel in upper mantle peridotite. *Chemical Geology*, 221(1-2), 65-101.
- Xu, Y., Liu, C. Z., & Lin, W. (2021). Melt extraction and reaction in the forearc mantle: Constraints from trace elements and isotope geochemistry of ultra-refractory peridotites of the New Caledonia Peridotite Nappe. *Lithos*, 380, 105882.
- Zhang, H., Zheng, J., Zhou, Y., Pan, S., Xiong, Q., Lin, A., & Zhao, Y. (2020). Mesozoic lithospheric modification and replacement beneath the Cathaysia Block: Mineral chemistry and water contents of the Daoxian peridotite xenoliths. *Lithos*, 358, 105385.